

## CASSINI PLASMA SPECTROMETER INVESTIGATION

D. T. YOUNG<sup>1</sup>, J. J. BERTHELIER<sup>3</sup>, M. BLANC<sup>4</sup>, J. L. BURCH<sup>1</sup>, A. J. COATES<sup>5</sup>,  
R. GOLDSTEIN<sup>1</sup>, M. GRANDE<sup>7</sup>, T. W. HILL<sup>8</sup>, R. E. JOHNSON<sup>10</sup>, V. KELHA<sup>11</sup>,  
D. J. MCCOMAS<sup>1</sup>, E. C. SITTLER<sup>9</sup>, K. R. SVENES<sup>12</sup>, K. SZEGÖ<sup>13</sup>,  
P. TANSKANEN<sup>14</sup>, K. AHOLA<sup>16</sup>, D. ANDERSON<sup>1</sup>, S. BAKSHI<sup>9</sup>,  
R. A. BARAGIOLA<sup>10</sup>, B. L. BARRACLOUGH<sup>2</sup>, R. K. BLACK<sup>1</sup>, S. BOLTON<sup>6</sup>,  
T. BOOKER<sup>1</sup>, R. BOWMAN<sup>1</sup>, P. CASEY<sup>1</sup>, F. J. CRARY<sup>1</sup>, D. DELAPP<sup>2</sup>, G. DIRKS<sup>1</sup>,  
N. EAKER<sup>1</sup>, H. FUNSTEN<sup>2</sup>, J. D. FURMAN<sup>1</sup>, J. T. GOSLING<sup>2</sup>, H. HANNULA<sup>11</sup>,  
C. HOLMLUND<sup>11</sup>, H. HUOMO<sup>15</sup>, J. M. ILLIANO<sup>3</sup>, P. JENSEN<sup>1</sup>, M. A. JOHNSON<sup>9</sup>,  
D. R. LINDER<sup>5</sup>, T. LUNTAMA<sup>11</sup>, S. MAURICE<sup>4</sup>, K. P. MCCABE<sup>2</sup>, K. MURSULA<sup>14</sup>,  
B. T. NARHEIM<sup>12</sup>, J. E. NORDHOLT<sup>2</sup>, A. PREECE<sup>7</sup>, J. RUDZKI<sup>1</sup>, A. RUITBERG<sup>9</sup>,  
K. SMITH<sup>1</sup>, S. SZALAI<sup>13</sup>, M. F. THOMSEN<sup>2</sup>, K. VIHERRKANTO<sup>11</sup>, J. VILPPOLA<sup>14</sup>,  
T. VOLLMER<sup>9</sup>, T. E. WAHL<sup>6</sup>, M. WÜEST<sup>1</sup>, T. YLIKORPI<sup>11</sup> AND C. ZINSMEYER<sup>1</sup>

<sup>1</sup>Southwest Research Institute, San Antonio, TX, U.S.A.

<sup>2</sup>Los Alamos National Laboratory, Los Alamos, NM, U.S.A.

<sup>3</sup>Centre d'étude des Environnements Terrestre et Planétaires, CNRS, St. Maur, France

<sup>4</sup>Observatoire Midi-Pyrénées, Toulouse, France

<sup>5</sup>Mullard Space Science Laboratory, University College London, Surrey, England

<sup>6</sup>Jet Propulsion Laboratory, Pasadena, CA, U.S.A.

<sup>7</sup>Rutherford Appleton Laboratory, Oxfordshire, England

<sup>8</sup>Rice University, Houston, TX, U.S.A.

<sup>9</sup>Goddard Space Flight Center, Greenbelt, MD, U.S.A.

<sup>10</sup>University of Virginia, Charlottesville, VA, U.S.A.

<sup>11</sup>VTT Information Technology, Espoo, Finland

<sup>12</sup>Norwegian Defense Research Establishment, Kjeller, Norway

<sup>13</sup>KFKI Research Institute for Particle and Nuclear Physics, Budapest, Hungary

<sup>14</sup>University of Oulu, Oulu, Finland

<sup>15</sup>Nokia Corporation, Helsinki, Finland

<sup>16</sup>TEKES Technology Development Centre, Helsinki, Finland

(Received 8 February 1998; Accepted in final form 9 January 2004)

**Abstract.** The Cassini Plasma Spectrometer (CAPS) will make comprehensive three-dimensional mass-resolved measurements of the full variety of plasma phenomena found in Saturn's magnetosphere. Our fundamental scientific goals are to understand the nature of saturnian plasmas primarily their sources of ionization, and the means by which they are accelerated, transported, and lost. In so doing the CAPS investigation will contribute to understanding Saturn's magnetosphere and its complex interactions with Titan, the icy satellites and rings, Saturn's ionosphere and aurora, and the solar wind. Our design approach meets these goals by emphasizing two complementary types of measurements: high-time resolution velocity distributions of electrons and all major ion species; and lower-time resolution, high-mass resolution spectra of all ion species. The CAPS instrument is made up of three sensors: the Electron Spectrometer (ELS), the Ion Beam Spectrometer (IBS), and the Ion Mass Spectrometer (IMS). The ELS measures the velocity distribution of electrons from 0.6 eV to 28,250 keV, a range that permits coverage of thermal electrons found at Titan and near the ring plane as well as more energetic trapped electrons and auroral particles. The IBS measures ion velocity distributions with very high angular and energy resolution from 1 eV to 49,800 keV. It is specially designed



to measure sharply defined ion beams expected in the solar wind at 9.5 AU, highly directional rammed ion fluxes encountered in Titan's ionosphere, and anticipated field-aligned auroral fluxes. The IMS is designed to measure the composition of hot, diffuse magnetospheric plasmas and low-concentration ion species 1 eV to 50,280 eV with an atomic resolution  $M/\Delta M \sim 70$  and, for certain molecules, (such as  $N_2^+$  and  $CO^+$ ), effective resolution as high as  $\sim 2500$ . The three sensors are mounted on a motor-driven actuator that rotates the entire instrument over approximately one-half of the sky every 3 min.

**Keywords:** Saturn, Titan, magnetosphere, space plasma, ion composition

## 1. Introduction

Saturn's magnetosphere comprises a unique plasma environment very different from that of the Earth or other planets. Although it shares a rapidly rotating magnetic field with the other giant planets, Saturn is distinguished by internal plasma sources such as Titan's atmosphere and ionosphere and the rings. The existence and location of Titan also permits the Cassini orbiter to execute a 4-year tour unlike that of any planetary magnetosphere to date including the Earth's. Over 40 close flybys of Titan and another dozen or so of the icy satellites present many opportunities for studies of magnetospheric interactions with planetary atmospheres and surfaces. Highly inclined passes near or through the auroral zone, and a wide sampling of both magnetic local time and latitude, constitute an unparalleled opportunity for comprehensive studies of the morphology and dynamics of the magnetosphere. Moreover, nearly all of the macroscopic phenomena mentioned here are associated with microphysical processes such as wave-particle interactions that can be studied to great advantage during the tour.

In order to be fully responsive to mission science objectives, the CAPS instrument is designed to make the most comprehensive possible suite of plasma measurements within constraints imposed by the mission and spacecraft itself. The balancing of measurement requirements, available technologies, and resource constraints has led to many tradeoffs that shaped the final execution of the CAPS design. A single plasma sensor cannot carry out the wide range of measurement objectives presented by the mission and therefore CAPS is made up of three sensors (see detailed descriptions in Sections 4 through 6). The Electron Spectrometer (ELS) measures differential electron velocity distributions making detailed studies of secondary electron fluxes that contribute to ionization and chemical processes taking place at Titan and elsewhere. At tens of keV ELS is expected to contribute to studies of trapped electrons and those associated with saturnian aurora. Throughout its energy range ELS will provide a global survey of plasma density, temperature and electron pitch angle distributions that are needed to derive a comprehensive view of plasma dynamics within the magnetosphere and, for roughly 50% of the mission, in the solar wind and magnetosheath.

At 9.5 AU the solar wind has cooled to become highly supersonic (Mach numbers  $\sim 10$  to  $>40$ ). The large amount of time that Cassini spends in the solar wind presents a rare opportunity to study both its intrinsic characteristics and its interactions with the magnetosphere of Saturn and possibly, the comet-like magnetosphere of Titan. The Ion Beam Spectrometer (IBS) is capable of the very high energy and angular resolution necessary not only for solar wind measurements, but also for observing ion ram fluxes at Titan and any auroral ion beams that might exist.

Many of the key questions of plasma origins and processes can only be answered through knowledge of plasma ion composition. Saturn's magnetosphere is known from Voyager to contain a wide variety of ion distributions that derive primarily from the icy surfaces of the satellites and rings, Titan's atmosphere, and, to a lesser extent, from Saturn's atmosphere and solar wind. Unfortunately very little is known about the composition of these plasmas and how the composition might affect magnetospheric phenomena. The Ion Mass Spectrometer (IMS), a high sensitivity, high-resolution mass spectrometer, is designed to provide comprehensive measurements in all regions of the magnetosphere. IMS relies on time-focused optics combined with carbon foil technology. It is designed to separate atomic species with high resolution, and to identify isobaric molecular species such as  $\text{CH}_4^+$ ,  $\text{NH}_2^+$ , and  $\text{O}^+$  (all with  $M/Q = 16$ , where  $M/Q$  is the mass/charge ratio) or  $\text{N}_2^+$  and  $\text{CO}^+$  ( $M/Q = 28$ ) that would otherwise require a very large conventional instrument to achieve. Because of its broad energy range IMS can be used to study the composition of Titan's ionosphere at a few eV, complementing the Ion and Neutral Mass Spectrometer (Waite *et al.*, 2004), or to study energetic trapped ions, complementing the MIMI/CHEMS investigation (Krimigis *et al.*, 2004).

We first present a discussion of investigation science objectives and measurement requirements (Section 2). We then describe the design, development, calibration, and operation of the CAPS instrument in some detail (Sections 3 through 7) and conclude with a discussion of instrument operations and modes (Section 8) and examples of performance data from the Cassini encounters with Earth and Jupiter (Section 9). A table of acronyms can be found in the Appendix.

## 2. Scientific Objectives

Cassini's broad scientific mission to study in depth the entire saturnian system, including its magnetosphere, admits of an equally broad range of scientific objectives for the CAPS investigation. These are primarily the saturnian magnetosphere and aurora, Titan's ionosphere and magnetosphere and the tenuous ionospheres of the rings and icy satellites. In the remainder of this section we discuss the CAPS scientific objectives in more detail as a way of providing motivation and background for measurement requirements and instrument design that are the focus of this paper.

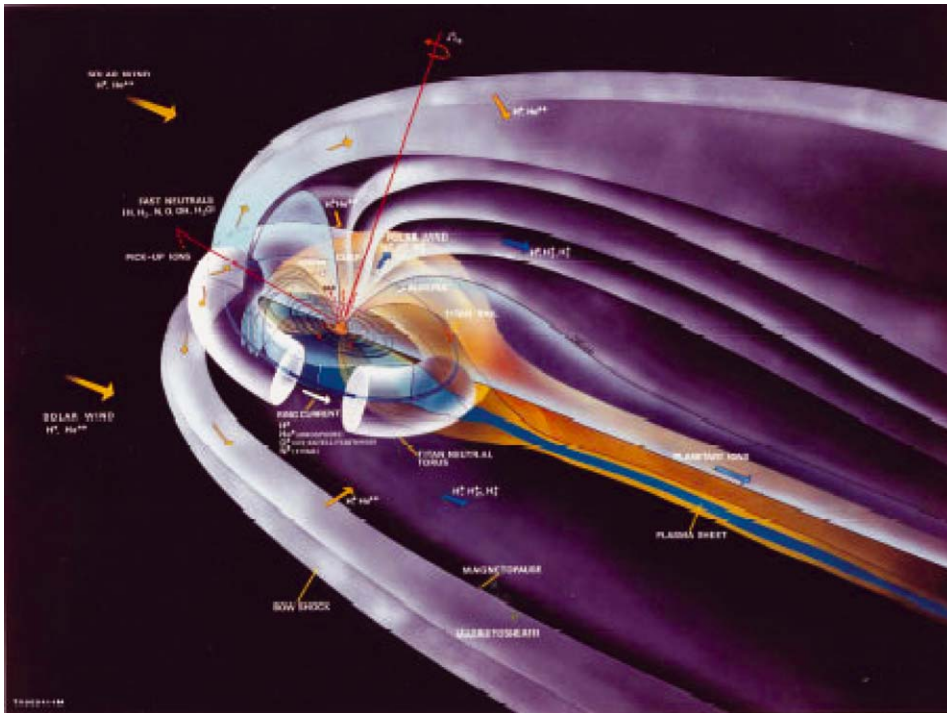


*Figure 1.* Three-dimensional rendering of the Saturnian magnetosphere showing solar wind streaming from the right, the donut-shaped torus shed by Titan, the inner region of material shed by icy satellites, and the orange-colored plasma sheet stretching out into the magnetotail. (Painting courtesy of J. Tubb, Los Alamos National Laboratory.)

## 2.1. SATURN'S MAGNETOSPHERE AND AURORA

Saturn's magnetosphere (Figure 1) envelops the extensive ring system and the collection of large icy satellites. It also encloses the orbit of Titan during average solar-wind conditions, although a strong solar-wind gust can push the magnetopause inside Titan's orbit temporarily on the day-side. The satellites and rings provide sources and sinks of plasma, thereby affecting the dynamics as well as the composition of the magnetospheric plasma. The plasma, in turn, affects the evolution of satellite surfaces and even the motion of the smallest particulates, providing a natural laboratory for *in-situ* study of dust-plasma interactions that have implications for solar-system evolution and many other astrophysical applications.

### 2.1.1. Plasma Sources and Sinks

Saturn's magnetosphere has three distinct internal sources of plasma: the upper atmosphere of Saturn (dominated by atomic hydrogen), the icy-satellite/ring system and associated neutral-gas cloud (dominated by water products), and Titan

(dominated by atomic nitrogen and perhaps atomic hydrogen). These are illustrated schematically in Figure 1. Data from Pioneer 11 and Voyagers 1 and 2 suggest that all three sources are effective, but their relative importance in various regions remains controversial (cf. Shemansky *et al.*, 1985; Richardson *et al.*, 1986; Richardson and Eviatar, 1987; Blanc *et al.*, 2004). External sources (solar wind and interstellar gas) are less evident in Voyager data but present in principle, and no less important to detect if present. Apart from its possible role as an external particle source for the magnetosphere, solar wind at 9.5 AU is expected to have high Mach numbers, providing a unique opportunity to study bow shock dynamics at very high-sonic Mach numbers. Also, the weaker interplanetary magnetic field at 9.5 AU will make shock layers thicker than at 1 AU and allow CAPS, with 2-s time resolution, to spatially resolve shocks. During the length of the tour we expect a very large number of bow shock crossings. We will look for reflected- and diffusion populations within the foreshock (Thomsen, 1985), accelerated electrons in the foreshock region (Klimas, 1985), and the leakage of magnetospheric plasma into the solar wind.

We will exploit four techniques to distinguish the source of resident plasma. One is to monitor atomic and molecular ion composition as a function of position in the magnetosphere. A wide variety of anticipated ion species must be resolved, including  $H^+$ ,  $H_2^+$ ,  $H_3^+$ ,  $He^{2+}$ ,  $O^+$ ,  $O^{2+}$ ,  $OH^+$ ,  $H_2O^+$ ,  $H_3O^+$ ,  $N^+$ , and  $N_2^+$ . It is particularly important to resolve  $M/Q$  16 ( $O^+$  from the icy satellite/ring system) from  $M/Q$  14 ( $N^+$  from Titan), which CAPS will easily do. Information on ion composition is often necessary but not always sufficient to distinguish the source of the plasma. For example,  $O^+$  and other water products can originate from any of the icy satellites or E ring particles, whereas  $H^+$  can originate from any of the several anticipated sources. A second clue to source location is the ion pitch-angle distribution (Figure 2). For example, a beam distribution centered on the particle source cone signifies an ionospheric source (Figure 2a), a pick-up ring distribution signifies a nearby equatorial source (Figures 2b and 2c), a shell or highly anisotropic “pancake” (isotropized ring) distribution signifies a more remote equatorial source (Figure 2d), and a quasi-Maxwellian distribution probably reflects a distant (e.g., solar-wind) source. (The precise shapes of the distributions will depend on the relative location of the source, the particle transit times and the rate of scattering due to wave-particle interactions.) The pick-up ring distribution may evolve into a shell, as observed near comets (Coates, 2003 and references therein), or into an anisotropic “pancake” distribution, depending on the ratio of the pickup and ion cyclotron wave velocities (Crary and Bagenal, 2000). Both regimes are expected to occur within Saturn’s magnetosphere. A third clue to source location is provided by a radial map of flux-shell plasma content, which tends to peak in source regions and to dip in loss regions. This quantity is obtained by integration of the ambipolar equilibrium equation along magnetic field lines, the accuracy of that depends on accurate measurements of the ion mass spectrum as well as the ion and electron temperatures and anisotropies. The fourth clue to source location

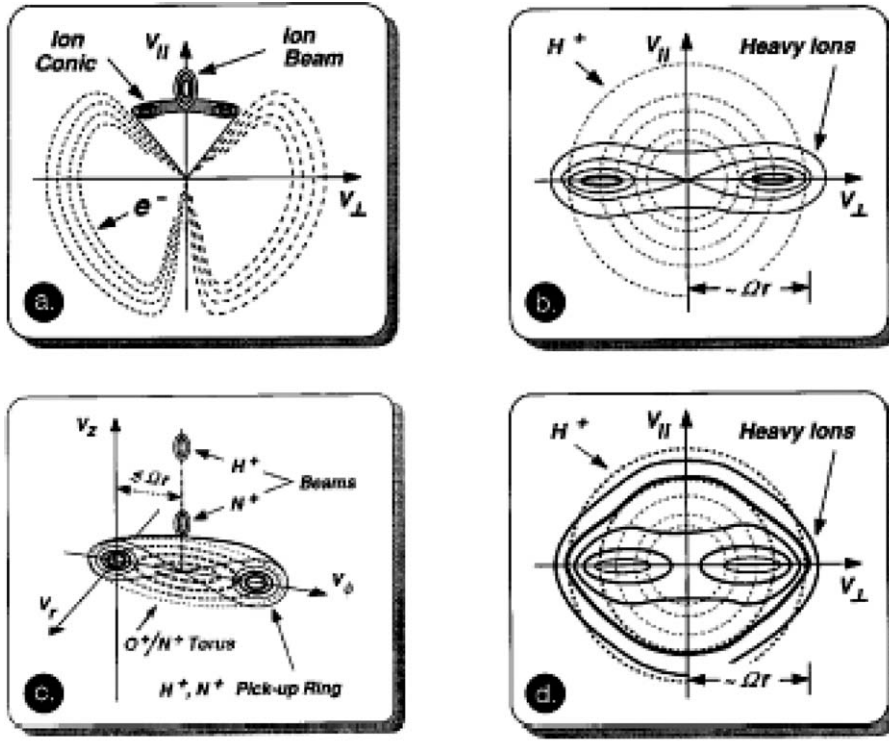


Figure 2. Representative ion velocity space distributions in the vicinity of Saturn.

is the corotation lag of magnetospheric plasma: the large-scale radial variation of the partial corotation speed provides information about the global outward mass transport rate (Hill, 1979), whereas localized departures from the general radial trend provide information on the local mass-loading rate due to ionization and charge exchange (Pontius and Hill, 1982). These last two signatures (flux-shell content variations and corotation lags) are apparent in Voyager data (Richardson, 1986; Eviatar and Richardson, 1986), and clearly contain a wealth of information that can be extracted with the greatly enhanced space/time coverage afforded by Cassini.

Plasma sinks (i.e., loss mechanisms) are also important as determinants of magnetospheric dynamics. These include absorption by solid bodies (icy satellites and E ring in particular), precipitation into Saturn's atmosphere, recombination (particularly dissociative, e.g.,  $\text{H}_2\text{O}^+ + e^- \rightarrow \text{H} + \text{OH}$ ), radial convective transport, and charge exchange (which is the primary loss mechanism). Each mechanism leaves a characteristic signature in plasma composition, energy, and/or pitch angle. These in turn can be exploited to determine their relative importance as a function of time and location in the magnetosphere.

### 2.1.2. *Plasma Transport*

The internal plasma sources described above all produce unstable particle distributions, which, among other effects, almost certainly drive radial convective ( $\mathbf{E} \times \mathbf{B}$ ) transport. The solar-wind interaction may also drive an Earth-like convection system, particularly on the night side where Saturn's ionosphere virtually disappears (Kaiser *et al.*, 1984a, b; Connerney and Waite, 1984), thereby reducing the coupling between Saturn and its magnetosphere. The spatial and temporal organization of the resulting flow is, however, completely unknown, and such information is critical to our understanding of the dynamics of Saturn's magnetosphere.

For example, does the convection consist primarily of small-scale eddy circulations that can be described in terms of a radial diffusion coefficient (e.g., Hood, 1985), or is there a persistent global-scale pattern? If a global pattern is present, is it organized with respect to saturnian longitude (indicating rotational control and an intrinsic magnetic-field asymmetry (e.g., Hill *et al.*, 1981)) or with respect to local time (indicating ionospheric or solar-wind control)? Saturn's kilometric radiation (SKR), for example, shows evidence of both rotational (Warwick *et al.*, 1981) and solar-wind (Desch and Rucker, 1983) control. Is plasma lost from the magnetosphere primarily through the formation of magnetotail plasmoids? If so, do plasmoids form as the result of the solar wind interaction as at Earth (e.g., Hones, 1979 and references therein) or as the result of planetary rotation as probably occurs at Jupiter (e.g., Vasyliunas, 1983 and references therein)? What is the origin of the high-density inclusions detected by the Voyagers in the outer dayside magnetosphere – are they vestiges of a Titan plume wrapped around Saturn (Eviatar *et al.*, 1982), or blobs of the central plasma sheet slung off by centrifugal force (Goertz, 1983), or something else? To address these and other questions we require not only accurate determination of the ion bulk flow speed, but also high spatial (hence temporal) resolution of boundaries between different flow regimes. Spatial precision is needed for accurate mapping of convection boundaries along the magnetic field to the ionosphere for comparison with auroral emission features observed by the UVIS instrument (Esposito *et al.*, 2004) and SKR emissions observed by the RPWS instrument (Gurnett *et al.*, 2004).

### 2.1.3. *Auroral Processes*

Voyager observations of SKR and UV emissions suggest strongly that parallel (magnetic-field-aligned) voltage drops enhance auroral precipitation at Saturn, as they do at Earth. Parallel voltages arise to maintain continuity of Birkeland currents along the converging magnetic field. They develop somewhere above the ionosphere where the velocity of current-carrying particles is a maximum, i.e., where the ratio of magnetic-field strength to plasma number density is greatest. This probably occurs below the minimum altitude reached by the Cassini orbiter, which would preclude direct observation of the accelerated electron beam below the voltage drop. There are, however, two distinct signatures of a parallel voltage drop that are discernible

at higher altitudes: (1) the presence of upward ion beams (Figure 2a), either strictly field-aligned beams resulting from direct parallel acceleration, or “conics” resulting from transverse acceleration followed by diamagnetic repulsion (e.g., Gorney *et al.*, 1981); and (2) the enlargement of the electron loss cone resulting from the tendency of the parallel electric field beneath the spacecraft to counteract the magnetic mirror force on the electrons (e.g., Mizera *et al.*, 1981). These two high-altitude signatures have been observed simultaneously from the DE-1 spacecraft above Earth’s aurora, and intercalibrated both with each other and with the classical low-altitude electron beam signature observed simultaneously by the DE-2 spacecraft orbiting beneath the acceleration region on the same field lines (Reiff *et al.*, 1988). Thus we have powerful analytical tools, tested in Earth orbit, for assessing the parallel voltage distribution along high-latitude field lines traversed by Cassini. It is also possible, although unlikely, that the Cassini orbiter will cross the aurora acceleration region. The location of the acceleration region depends on the electron density at high latitudes, which is poorly constrained by existing data. If sufficiently low densities place the acceleration region above  $3R_S$  from body center, then Cassini would pass through this region.

To apply these tools it is essential to resolve the atmospheric loss cones (or source cones) of both ions and electrons. It is also important to bear in mind that the terrestrial signatures cited above refer to an upward parallel electric field, which covers most terrestrial cases but not necessarily most saturnian cases. Significant parallel electric fields are generally upward at Earth because the flux of current-carrying electrons available from the ionosphere typically exceeds that available from the magnetosphere by a wide margin (Knight, 1973), a condition that may not apply at Saturn, particularly on the night side.

## 2.2. TITAN AND ITS INTERACTION WITH SATURN’S MAGNETOSPHERE

The interaction of Titan with Saturn’s magnetosphere provides an opportunity to study a unique regime of the parameter space relevant to the interaction of magnetized plasma with a non-magnetized body. Here, we briefly assess our current understanding of four important facets of Titan’s interaction with the magnetosphere of Saturn (see Ip, 1992, for more details) that are directly relevant to the CAPS investigation.

*Ionosphere.* Ionization of Titan’s atmosphere above 700 km results from the action of solar EUV, impact ionization caused by the incoming corotating flow ( $\sim 20\%$  of that caused by EUV, Keller *et al.*, 1994a, b; Luna *et al.*, 2003), and precipitation of magnetospheric electrons. Because the corotation direction and the direction of solar radiation differ around its orbit, any part of Titan’s ionosphere may have different contributors to ionization at any one time (Nagy and Cravens, 1998; Figure 2). The best direct evidence for the ionosphere is the Voyager 1 observations of a plasma and magnetic wake behind Titan’s trailing hemisphere

(Hartle *et al.*, 1982a,b). Quantitatively, only upper limits on the ionospheric electron density ( $\sim 2400 \pm 1100 \text{ cm}^{-3}$  at the terminators) could be derived from radio occultations (Bird *et al.*, 1997). Models of Titan's ionosphere suffer from a lack of observational constraints and from difficulties inherent in Titan's environment: complex ion chemistry coupled with the neutral  $\text{N}_2\text{-CH}_4$  atmosphere, and intricate boundary conditions set by the interaction with Saturn's magnetic field. Elaborated models of Titan's ionosphere (e.g., Ip, 1990; Keller and Cravens, 1994; Keller *et al.*, 1994; Cravens *et al.*, 1998, Ledvina, *et al.*, 1998), which predict an electron density peak near 1200 km (the exobase is at 1500 km), show that solar photons are presumably the principal agent of ionization, and that chemistry is initiated by the formation of  $\text{N}^+$  and  $\text{N}_2^+$ . Such species can lead to many more complex molecules including  $\text{H}_2\text{CN}^+$ ,  $\text{CH}_5^+$ ,  $\text{C}_2\text{H}_5^+$ ,  $\text{C}_3\text{H}_m^+$ .

*Magnetic Field Interactions.* The magnetospheric flow past Titan is expected to be sub-magnetosonic ( $M_S$  and  $M_A \sim 0.5$ ; Ness *et al.*, 1982 a,b) over most of Titan's orbit. MHD simulations (Hansen *et al.*, 2001) suggest that the flow may be weakly super-magnetosonic when Titan is on the dusk side of the magnetosphere. Thus, the Titan/magnetosphere interaction is distinct from both the Venus-Mars/solar-wind interaction ( $M_A > 1$ ,  $M_S > 1$ ), and the Io-torus/magnetosphere interaction ( $M_A < 1$ ,  $M_S > 1$ ). No fast upstream shock is expected, except in those rare instances when Titan is in the upstream solar wind or when Titan is in the dusk side of the magnetosphere. Either mass-loading or Titan's ionospheric Pedersen conductivity can cause the magnetospheric flux tubes to slow down, drape around Titan, and form an ionospheric wake downstream (Luhmann, 1996).

The wake resembles an induced magnetotail with the northern and southern lobes comprising oppositely directed field lines (Ness *et al.*, 1982a,b). The draping of the field lines at Titan, whose magnetotail diameter is  $\sim 2R_T$ , is more extreme than at Venus (diameter  $\sim 3R_V$ ), or Mars (diameter  $\sim 5R_M$ ) (Luhmann *et al.*, 1991). Brecht *et al.* (2000) have obtained initial results of global hybrid numerical simulations of Titan's magnetic interactions that reveal the complexity of the interaction caused by ion kinetics (Ledvina *et al.*, 2000). The spatial scale of the interaction, which is determined by the heavy ion gyroradius or inertial scale length, depends significantly on mass loading of the flow. Recent models indicate that Titan's ionosphere supports currents that exclude the magnetospheric field from altitudes below about 1000 km (Lindgren *et al.*, 1997).

*Escape of Charged Particles.* At the interface with magnetospheric plasma flow, charged particles are removed continuously from Titan's ionosphere, and some neutrals above the exobase are ionized. Newly created particles are accelerated to the local plasma corotation rate, implying exchange of momentum and energy between Saturn's magnetosphere and Titan's atmosphere. The draping of the magnetic field lines around Titan is associated with this momentum transfer. In a three-dimensional multi-species model, Nagy *et al.* (2001) have found that tailward escape of heavy ions creates a flux  $\sim 6.5 \times 10^{24}$  ions/s. Kopp and Ip (2001) and others have argued that mass loading is asymmetric at Titan because the ion gyroradius is of the order

of Titan's radius. Because MHD models neglect gyroradius effects, this asymmetry emphasizes the need for a kinetic model. There is no evidence of electron acceleration at Titan. Instead, a bite-out of electrons with energies  $>800$  eV was observed (Bridge *et al.*, 1981), which is suggestive of magnetospheric electron absorption by Titan (Hartle *et al.*, 1982). Because corotation still prevails at  $20R_S$ , the charged particles escaping Titan tend to form a torus around Saturn. However, frequent motions of the magnetopause, as well as effects of convection, displace particles radially from their original position. This may result in a multitude of dense, cool plasma "blobs" or "plumes" in the outer magnetosphere, which is otherwise filled by a hot, tenuous plasma. Plumes were observed in the neighborhood of Titan's orbit by Eviatar *et al.* (1982), who interpreted them as a plume wrapped around Saturn. Goertz (1983) proposed that the plumes were instead detached from Saturn's inner plasma-sheet and centrifugally transported outward.

*Escape of Neutrals.* Diffuse neutral gas dominates the particle environment of Saturn: the neutral to plasma density ratio is typically about 10 (Richardson, 1998). Neutrals may also eventually escape Titan's upper atmosphere (e.g., Shematovich *et al.*, 2003). The anticipated species are H, H<sub>2</sub> and N. The existence of a hydrogen cloud has been confirmed by Voyager measurements of Lyman-alpha emission. This cloud probably connects to the extended hydrogen corona of Saturn (Broadfoot *et al.*, 1981; Shemansky and Hall, 1992) and to hydrogen-rich icy surfaces in the inner magnetosphere. Molecular hydrogen, H<sub>2</sub>, may result from the photolysis of CH<sub>4</sub> but the existence of an H<sub>2</sub>-cloud remains speculative. Nor has a cloud of neutral nitrogen been observed. Monte Carlo model calculations show that neutrals escape by non-thermal processes initiated by UV photons, and precipitating electrons and ions (e.g., Ip, 1992; Keller and Cravens, 1994; Keller *et al.*, 1994; Shematovich *et al.*, 2003), processes often lumped together as atmospheric sputtering (Johnson, 1994). This loss rate has recently been shown to be sensitive to the slowing and deflection of co-rotating ions and to the flux of locally produced pick-up ions (Brecht *et al.*, 2000; Shematovich *et al.*, 2003). Therefore, the measurement of plasma ion energies and fluxes near Titan by CAPS will be critical in modeling neutral interactions with the atmosphere.

Neutrals that escape Titan become distributed in a torus as Titan orbits Saturn. Charge-exchange between the neutral torus and magnetospheric ions, as well as electron impact dissociation, direct photoionization, and electron-impact ionization, are appreciable sources of H<sup>+</sup> and N<sup>+</sup>, as well as molecular ions, in the magnetospheric plasma. Studying Titan's interaction with Saturn's magnetosphere will enable us to set important constraints for our general understanding of Titan's upper atmosphere and ionosphere. Progress on the four key problems cited above requires high-temporal resolution to identify spatial boundaries, high-angular resolution to track plasma acceleration, and high-mass resolution to separate and identify neighboring ion species. We anticipate that CAPS performance will allow us to achieve these objectives. Many close encounters with Titan during the tour will be essential because the outer magnetosphere of Saturn is highly variable and

also because unique information will be provided by variations in the local time geometry of each fly-by.

### 2.3. ICY SATELLITES AND RING PARTICLES

Scenarios for the formation of the icy satellites all assume that volatiles other than water were part of the initial composition (Stevenson, 1982). However, until recently the only volatile clearly seen by Pioneer, Voyager and Earth-based observers is water. On the other hand, atoms and molecules are ejected from surfaces by a number of processes. Because the energies of the ejected atoms and molecules are too small to escape from Saturn, this material either recondenses or is ionized and picked up by the corotating magnetic field. Plasma in the inner magnetosphere has been shown to come from satellites and ring particles (see discussion below) therefore it should be possible to use CAPS data to determine their surface compositions (Johnson and Sittler, 1990).

A principal process for ejection of neutrals from the surfaces of the satellites and ring particles is sputtering by the plasma itself, in which case the plasma is self-sustained (Huang and Siscoe, 1987). Noll *et al.* (1997) reported an observation suggestive of O<sub>3</sub> primarily on the trailing hemispheres of Dione and Rhea, and the possible presence of O<sub>3</sub> requires that O<sub>2</sub> exist in the ice (Johnson and Jessor, 1996). The observation of O<sub>3</sub> is important for two reasons. First, it is a clear indication that magnetospheric plasma ions impact the surfaces of Dione and Rhea (Johnson and Quickenden, 1997) and, second, it confirms that these ions produce new chemical species from the surface materials (Johnson, 1990; Johnson *et al.*, 1997; Delitsky and Lane, 1997). Therefore, this observation strengthens the suggestion that the plasma in Saturn's magnetosphere is a product of sputtering of ring particle and satellite surfaces by energetic ion impact. This bombardment also complicates analysis and understanding of the surface composition because reactive nitrogen ions that diffuse inward from Titan's torus are implanted into the icy surfaces.

Earlier telescopic and spacecraft observations were also suggestive of plasma bombardment and modification of the surfaces of the icy satellites. Differences in reflectance, particularly at short wavelengths, between the leading and trailing hemispheres were suggestive of radiation damage and sputtering of ice by the plasma. Differences in weak IR water bands between the hemispheres also were suggestive of plasma erosion and modification. Finally, preliminary modeling of the composition and spatial distribution of the plasma appear to confirm its self-sustained production.

As noted above, even the primary composition of the plasma was uncertain until recently. The lack of mass resolution on the Voyager PLS and LECP instruments allowed the hypothesis that N and H from Titan could be the dominant source of plasma in the inner magnetosphere rather than H<sub>2</sub>O from the satellites and

ring particles. This issue was decisively settled by the observations of gas-phase OH co-existing with the plasma (Shemansky *et al.*, 1993). These observations combined with modeling (e.g., Ip, 1995; Jurac *et al.*, 2002) confirmed that the icy satellites and ring particles were the principal source of plasma in the inner saturnian magnetosphere. However, the recent estimates of source rates for nitrogen from Titan (Shematovich *et al.*, 2003) are such that  $N^+$  diffusing inward from Titan's torus may be a significant, possibly dominant component of the *energetic* heavy ions in the inner magnetosphere.

The amount of OH seen by Voyager was larger than that initially predicted due to plasma bombardment alone (Johnson *et al.*, 1989), suggesting that additional processes cause the loss of surface material. Recent modeling has confirmed that within  $\sim 4.5R_S$  sources other than the sputtering of satellite surfaces contribute (Jurac *et al.*, 2001, 2002), whereas at larger distances satellite sputtering dominates (Shi *et al.*, 1995a, b).

Eventually, inner magnetospheric sources of plasma begin to overlap Titan's neutral out-flow. The other possible neutral and plasma sources are sputtering of E-ring grains (Morfill *et al.*, 1993), self-erosion of E-ring grains by collisions (Horanyi *et al.*, 1992), particulate bombardment of the icy satellites (Haff *et al.*, 1983; Burns and Mathews, 1986), micro-meteorite erosion of the main rings (Ip, 1984), and plasma sweeping of the ambient gas emanating from the main rings (Ip, 1995). Jurac *et al.* (2001, 2002) have shown that there is likely to be "unseen" material orbiting in the vicinity of Mimas and Enceladus, acting as sources of the plasma and the neutral OH cloud.

In addition to determining the composition and dynamics of the plasma in the inner saturnian magnetosphere, the CAPS data, combined with modeling of ambient neutrals and plasma, will be able to definitively unravel the physical processes determining various source strengths. However, what may be more important to planetary science is the following. Because the rings and satellites are sources, and different objects will dominate the local source at different distances from Saturn, CAPS can obtain compositional information on individual objects. In addition to the spatial distribution of composition, which can be masked by diffusion, measurement of the energy and pitch-angle distributions of a particular species will distinguish freshly produced ions from those that have diffused inwards or outwards. Such measurements would be particularly advantageous on a close pass by a satellite or in regions where ring sources dominate.

Observations of the icy satellites and rings have a long history but there is very little definitive composition information on these objects. Although Cassini will carry imaging spectrometers that in principle will be able to identify species other than  $H_2O$ , the plasma bombardment itself can make such identifications difficult. First, sputtering depletes surface layers of the most volatile species, causing enhanced diffusion from depth and loss of volatiles. Moreover, bombardment also chemically alters the materials. For example,  $H_2O$  is decomposed to  $H_2$  and  $O_2$ ,  $NH_3$  can be converted into  $N_2H_4$  and  $N_2$ , and carbon bearing species into volatiles

such as CO, CO<sub>2</sub> and refractory carbon chains. These species are often difficult to observe spectroscopically.

By contrast, the sputtering process acts as a natural mass spectrometer with atomic and molecular ions produced roughly stoichiometrically (Johnson and Sittler, 1990). CAPS IMS can identify the presence of intrinsic parent species and is capable of separating important atomic and molecular ions that have nearly the same molecular weight. The target list of separable sputter products includes (in order of increasing mass-to-charge ratio): C<sup>+</sup> ( $M/Q = 12$ ); CH<sup>+</sup> ( $M/Q = 13$ ); N<sup>+</sup>, CH<sub>2</sub><sup>+</sup> ( $M/Q = 14$ ); NH<sup>+</sup>, CH<sub>3</sub><sup>+</sup> ( $M/Q = 15$ ); O<sup>+</sup>, NH<sub>2</sub><sup>+</sup>, CH<sub>4</sub><sup>+</sup> ( $M/Q = 16$ ); OH<sup>+</sup>, NH<sub>3</sub><sup>+</sup> ( $M/Q = 17$ ); H<sub>2</sub>O<sup>+</sup> ( $M/Q = 18$ ); and H<sub>3</sub>O<sup>+</sup> ( $M/Q = 19$ ). Other, heavier molecules of importance in the sputtering process that can be separated include: C<sub>2</sub><sup>+</sup>, ( $M/Q = 24$ ), C<sub>2</sub>H<sup>+</sup> ( $M/Q = 25$ ); CN<sup>+</sup>, C<sub>2</sub>H<sub>2</sub><sup>+</sup> ( $M/Q = 26$ ); and CO<sup>+</sup>, N<sub>2</sub><sup>+</sup> ( $M/Q = 28$ ). The CAPS data in conjunction with modeling can therefore provide definitive analysis of satellite and ring surfaces for the planetary community.

### 3. Design Approach

The stated goal of the Cassini mission is to achieve measurements “at least 10-times better than that of Voyager.” In order to meet this goal, Voyager observations (Sittler *et al.*, 1983) and models of the saturnian plasma environment (Richardson and Sittler, 1990; Richardson, 1995; Richardson *et al.*, 1998) were used to develop CAPS science objectives, performance guidelines, and sensor requirements. A second important goal relative to Voyager performance is that CAPS should provide complete coverage of electron and ion velocity distributions, eliminating gaps between Voyager PLS (Bridge *et al.*, 1977) and LECP (Krimigis *et al.* 1977) instruments. Those gaps were <10 eV for electrons and ions; 6 to 14 keV for electrons, 6 to 30 keV for protons, and 6 to ~70 keV for O<sup>+</sup>. A third key goal is to measure unambiguously the composition of all major atomic and molecular ions from 1 to 50,000 eV.

With reference to Figure 3 and Table I, our measurement goals call for ELS to obtain medium-resolution electron energy-angle spectra; the IBS to obtain high-resolution energy-angle spectra; and the IMS to obtain high-mass resolution and medium energy-angle resolution of ions. Figure 3 is a simplified overview of the CAPS instrument layout and particle optics. All three sensors have in common that they are based on charged particle motion in electrostatic fields. After entering the sensors through wedge-shaped fields-of-view, particle trajectories are dispersed in electric fields and then measured using electron-multiplier detectors. The ELS and IBS optics separate electrons and ions respectively by energy/charge ( $E/Q$ ) ratio and by elevation angle of arrival (out of the plane of Figure 3). The second angle, azimuth, is obtained by sweeping the sensor fields-of-view using a motor-driven actuator. From knowledge of detector counting rates as a function of energy and two angles, particle velocity distributions can be deduced. The IMS optics also

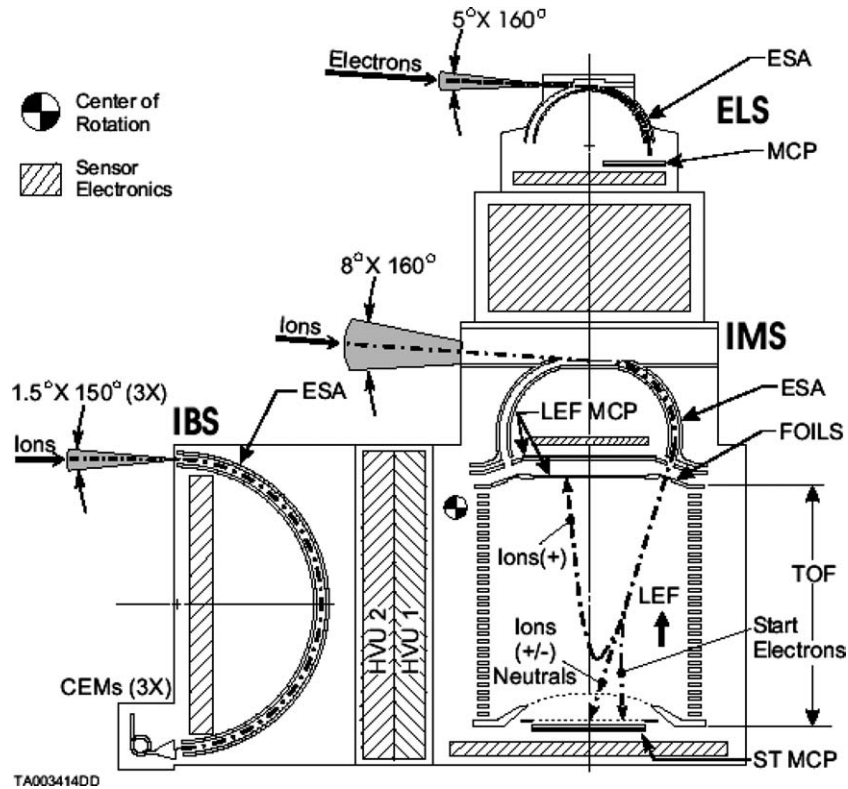


Figure 3. Optical layout, fields-of-view, and key sensor elements of CAPS shown in the  $X$ - $Y$  (azimuthal) plane of the spacecraft (see Figure 4). Cross-hatched areas Figure 3 indicate sensor electronics subsystems. Heavy dashed lines suggest the general shape of particle trajectories.

separate ions by  $E/Q$  and angle of arrival, but then in addition disperse them by time-of-flight (TOF) in a novel high-resolution mass spectrometer. IMS is capable of separating major ion species to  $\sim 1\%$  of the total flux, and minor ion species to  $\sim 0.1\%$  or better of the total flux.

An important design consideration is the location of CAPS on the spacecraft (Figure 4). Of particular concern was obtaining good separation from the main Cassini engines and thrusters (potential sources of chemical contamination), separation from the radioisotope thermoelectric generators (potential source of penetrating background radiation), and separation from any sources of electrostatic charging. With all these considerations in mind, the best location for CAPS turned out to be on the underside of the fields-and-particles pallet (Figure 4) adjacent to the MIMI/CHEMS instrument (Krimigis *et al.*, 2004) and just below the INMS (Waite *et al.*, 2004). Although meeting all of the above criteria for location, CAPS still did not have an acceptable field-of view because it was fixed to the spacecraft body and thus could only view in directions constrained by spacecraft orientation. In order to counteract this limitation, the CAPS sensors were mounted on a rotating

TABLE I  
CAPS sensor performance summary.

Parameter	IMS			
	Med. Res.	High Res.	ELS	IBS
Energy/charge response				
Range (eV/e)	1–50,280		0.6–28,750	1–49,800
Resolution $(\Delta E/E)_{\text{FWHM}}$	0.17		0.17	0.014
Angular response				
Elevation sectors (number)	8		8	3
Instantaneous FOV $(AZ \times EL)_{\text{FWHM}}$	$8.3^\circ \times 160^\circ$		$5.2^\circ \times 160^\circ$	$1.4^\circ \times 150^\circ$
Angular resolution $(AZ \times EL)_{\text{FWHM}}$	$8.3^\circ \times 20^\circ$		$5.2^\circ \times 20^\circ$	$1.4^\circ \times 1.5^\circ$
Mass/charge response				
Range (amu/e)	1 ~ 400	1 ~ 100	–	–
Resolution $(M/\Delta M)_{\text{FWHM}}$	8	60	–	–
Energy-geometric factor* $(\text{cm}^2 \text{ sr eV/eV})$	$5 \times 10^{-3}$	$5 \times 10^{-4}$	$1.4 \times 10^{-2}$	$4.7 \times 10^{-5}$
Temporal response				
Per sample (s)	$6.25 \times 10^{-2}$		$3.125 \times 10^{-2}$	$7.813 \times 10^{-3}$
Energy-elevation (s)	4.0		2.0	2.0
Energy-elevation-azimuth (s)			180	

\*Applies to total field-of-view and includes efficiency factors.

platform driven by a motor actuator capable of sweeping the CAPS instrument by  $\sim 180^\circ$  around an axis parallel to the spacecraft Z-axis (Figure 4). In this way nearly  $2\pi$  sr of sky can be swept approximately every 3 min regardless of spacecraft motion or lack thereof. Although not ideal for plasma measurements under all circumstances (e.g., when the spacecraft body blocks the direction looking into a plasma flow), careful design of observing periods permits effective performance under most conditions.

Although adding a rotating platform provides a means of turning the instrument, the spacecraft nonetheless occludes parts of the FOV as shown in Figure 5. At about  $+80^\circ$  azimuth parts of the fields and particles pallet (FPP), the neighboring LEMMS instrument, and RTG shielding obscure the CAPS FOV. Encroachments are actually

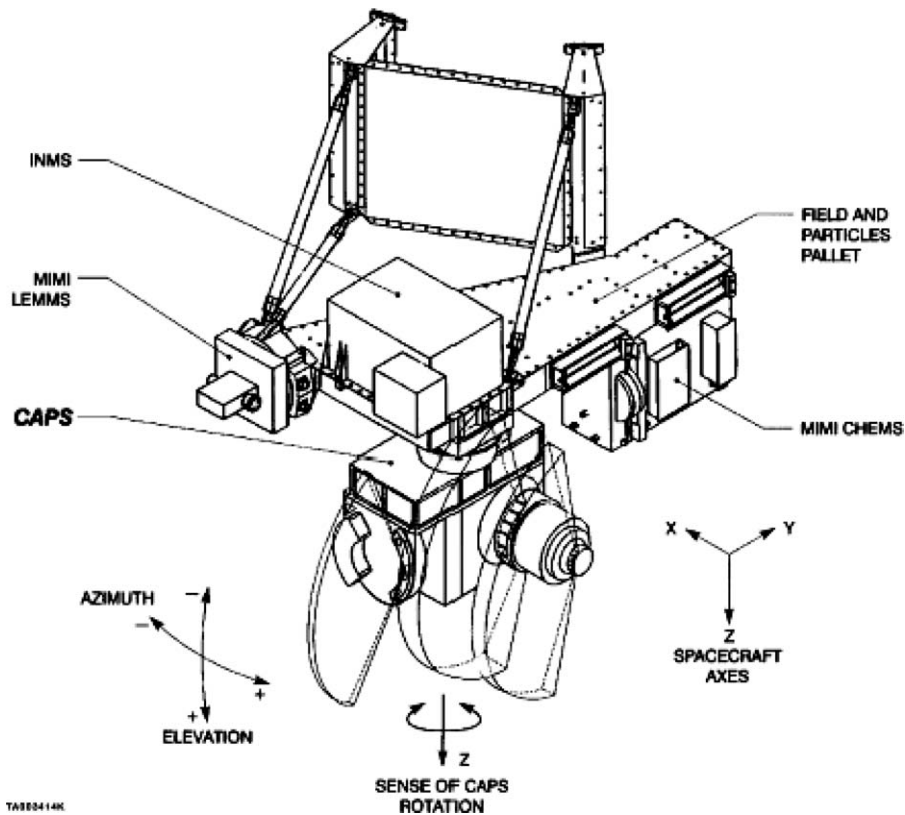


Figure 4. Location and orientation of CAPS on the Fields and Particle Pallet. Note the definitions of azimuth (in the spacecraft  $X$ - $Y$  plane) and elevation (parallel to the spacecraft  $Z$ -axis) angles. These will be used throughout the paper to describe instrument orientations and fields-of-view (FOV).

larger than shown here because of multi-layer thermal insulation blankets that stand off from all spacecraft surfaces by  $\sim 5$  cm.

#### 4. Electron Spectrometer

##### 4.1. PRINCIPLES OF OPERATION

The ELS sensor (Figure 6) is a hemispherical top-hat electrostatic analyzer (ESA) similar to that described by Carlson *et al.* (1983). Its implementation is based closely on the High-Energy Electron Analyzer (HEEA), part of the Cluster Plasma Electron and Current Experiment (PEACE) (Coates *et al.*, 1992; Johnstone *et al.*, 1997). The ELS energy range and angular field-of-view (FOV) overlap considerably with the MIMI/LEMMS solid-state electron detectors (Krimigis *et al.*, 2004), producing complete coverage on Cassini from 1 eV to  $\sim 250$  keV with no gaps.

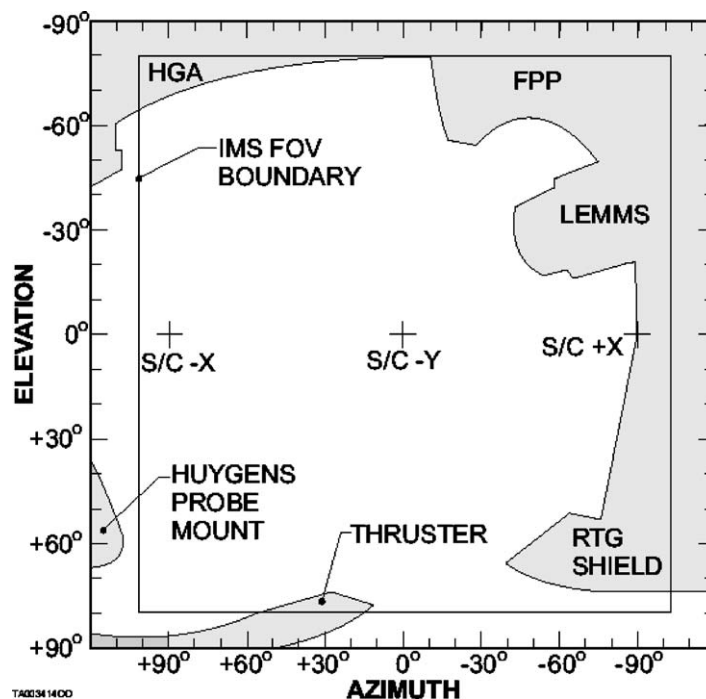


Figure 5. All-sky projection of the CAPS IMS field-of-view. Encroachment on the CAPS FOV are caused by surrounding spacecraft structures (shaded areas). Similar encroachments occur for IBS and ELS sensors.

Electrons enter the sensor via a grounded baffle (Figure 6) and then pass between concentric hemispherical electrostatic analyzer (ESA) plates before impacting on an annular micro-channel plate (MCP) detector. Angular and energy resolution of the ELS are determined by the relative spacing between the two concentric hemispheres,  $R_0/\Delta R$ . In addition, the analyzer energy acceptance is proportional to  $R_0/\Delta R$  times the voltage applied to the inner hemispherical plate. An energy spectrum is obtained by changing the voltage on the inner hemisphere in discrete, programmable steps. Electron direction of arrival in elevation is determined from the position at which it strikes the detector, recognized by the anode positioned behind the MCP (Figure 7). A number of innovative aspects from PEACE have been incorporated in the design of the ELS analyzer, including reduction of photoelectron susceptibility (Alsop *et al.*, 1998) and high-relative mechanical accuracy (Woodliffe and Johnstone, 1998) that minimizes errors in electron energy measurements.

When operating, the ELS executes consecutive energy sweeps in which the selected energy (voltage) is held for a fixed accumulation time (31.25 ms) and then stepped down to the next level. One quarter of the accumulation interval is dead time that permits readout of the detector counters and settling of the sweep high voltage.

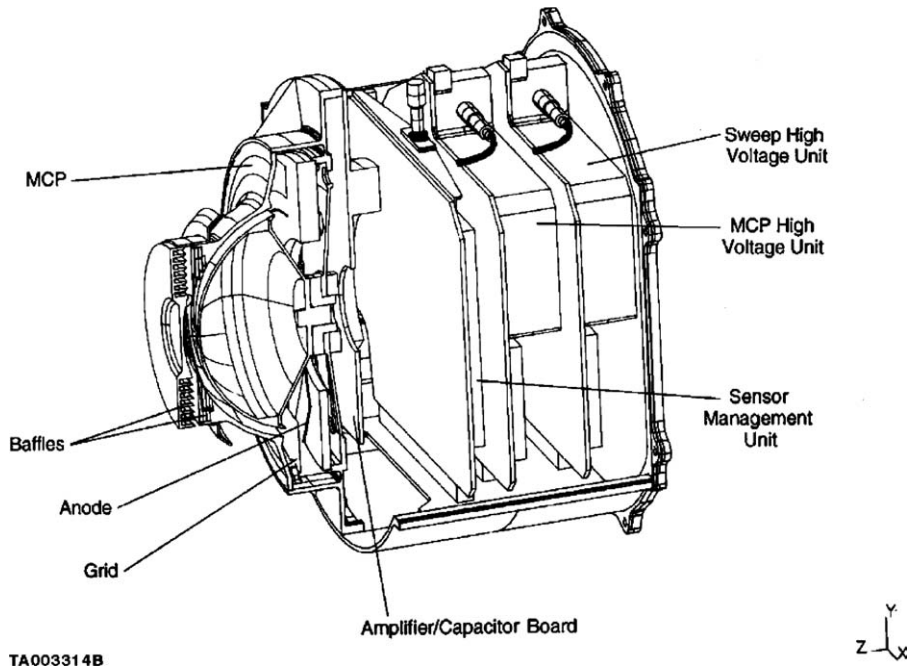


Figure 6. Cutaway drawing of the ELS sensor and electronics unit.

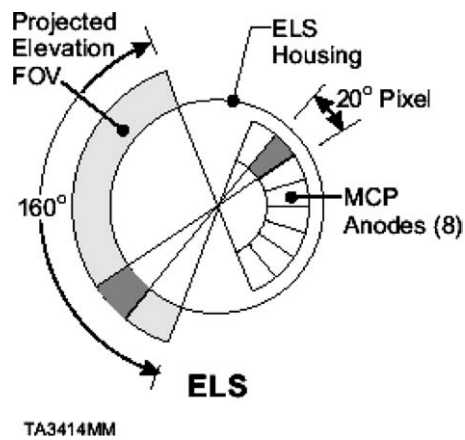


Figure 7. ELS field-of-view in the elevation plane showing its mapping to detector pixels.

In normal operation, a 64-level logarithmic energy spectrum is scanned between 0.6 and 28,000 eV in 2 s. The sequence is repeated until ELS is commanded to do otherwise. Three high-voltage step tables are stored in the ELS. Sweep Table-AI, the default mode, contains 64 values log-spaced over the energy range 0.6 eV–28.75 keV separated by 16% decrements this will likely be the workhorse mode

of ELS in the saturnian magnetosphere. Energy separation in this mode is matched to the analyzer pass-band to ensure contiguous energy coverage. Alternatively, 32 values out of the 64 available can be selected by setting the starting point of the energy sweep to any of the top 32 steps. Sweep Table B contains 32 values with 25% decrements. This mode scans over a range of 1–1000 eV and is tailored to solar wind measurements. Voltage Table C consists of 32 values with 36% decrements over an energy range of 1.8–22,000 eV. It is designed to provide faster time resolution (1 s/sweep) over most of the available energy range. A fixed-step mode is also available to facilitate ground calibration and to enable high-time resolution measurements at a fixed energy if needed.

#### 4.2. ELECTRON OPTICS

Studies by Carlson *et al.*, (1983) indicate that a bending angle of  $75^\circ$  is an optimal tradeoff between resolution and sensitivity for a top-hat ESA. Once the shape and alignment of the hemispheres was selected, secondary electron and UV rejection became major optical design considerations. In order to minimize their effects, the input collimator aperture incorporates a saw-tooth baffle structure designed to reduce particle and solar UV scattering. The central baffle section has a spherical profile that maintains the desired electric field in the ESA. A series of concentric ring-shaped baffles on the top inner surface of the outer hemisphere forms a second line of defense against stray UV and photoelectrons. The combination of these two features ensures that there is no direct line-of-sight from the aperture to the hemispherical solid surfaces.

Potential effects of sunlight in the sensor were further reduced by application of a highly absorbent, diffusely reflecting surface layer of copper oxide crystals (grown using the Ebanol-C process (Alsop *et al.*, 1998)) deposited on all internal surfaces. The film is electrically conducting, has good adhesion, and is sufficiently thin (less than  $8\ \mu\text{m}$ ) and uniform to maintain the analyzer's mechanical accuracy requirements. During operation, the inner ELS hemisphere is set to one of a programmable series of positive voltage steps (the outer hemisphere is grounded). Stepping this voltage shifts the narrow band of electron energies transmitted by the ESA. Electrons emerging after a field-defining grid reach the MCP detector. In order to maintain a satisfactory analyzer bending-angle and also to prevent high-voltage breakdown, the MCP could not be located at the optimum focus position behind the ESA. Instead, a grid was placed at the focus directly below the analyzer exit, with the MCP positioned below this and  $90^\circ$  away from the analyzer entrance. (In any case the coarse anode pattern does not require very good focusing).

The grid between the analyzer exit and the MCP defines the  $160^\circ$ -wide elevation FOV of the sensor. The grid is made from Laser-cut phosphor bronze plated in gold. An optimum design thickness of  $125\ \mu\text{m}$  was obtained by considering electric field definition requirements versus mechanical strength. By biasing the grid at  $-8\ \text{V}$

TABLE II  
ELS key sensor data and dimensions.

Parameter	Value
ESA type	Spherical top-hat
Mean radius	4.15 cm
Plate spacing	0.30 cm
Analyzer constant	6.3
Plate bending angle	75°
Top-hat set-back angle	19.0°
Top-hat aperture radius	1.35 cm
Detector	Chevron MCP
Detector anode inner radius	3.95 cm
Detector anode outer radius	4.35 cm

(normally at 0 V) to repel electrons and by setting the plate voltage to its minimum (0.1 V), the background count-rate due to penetrating radiation can be measured. The 160° annular segment of the grid is divided into tapered windows at 2° intervals and has a calculated transparency in excess of 80%.

#### 4.3. RAY-TRACING AND MODELING RESULTS

The electron spectrometer has been extensively studied by numerical simulation. Optical design, UV susceptibility and total electron fluence during the mission were all simulated. The resulting design is similar to that of the HEEA (Johnstone *et al.*, 1997), except that an analyzer bending-angle of 75° was chosen. Table II gives key sensor data and dimensions for the ELS.

The electrostatic modeling performed for PEACE has been described elsewhere (Woodliffe, 1991). The potential distribution in a three-dimensional electrostatic model of the instrument was solved using the Laplace equation and spline interpolations between the grid points. Analyzer response was calculated in three ways using electron ray-tracing based on: (1) a regular starting grid, (2) a Monte Carlo approach, and (3) tracing of the outside edge of the response function, i.e., the extreme limiting trajectories. The latter technique was a quick way of determining instrument response and establishing the major design parameters. Then Monte Carlo particle tracing was used to study detailed analyzer response and for comparisons with calibration.

The results of electron optical modeling are summarized in Table III. The acceptance space of the analyzer can be thought of as three-dimensional in energy, elevation angle and azimuthal angle. In the simulation, electrons are started at a range of angles and energies using the second technique above. For each dimension,

TABLE III  
Comparison of simulated and measured ELS analyzer characteristics.

Parameter	Simulated value	Measured value in 125 eV calibration	Measured value in 960 eV calibration
Elevation FWHM (°)	20.0	$20.20 \pm 0.23$	$20.26 \pm 0.27$
Azimuth FWHM (°)	5.24	$6.45 \pm 0.06$	$5.68 \pm 0.04$
Azimuth midpoint (°)	–	$0.41 \pm 0.07$	$0.06 \pm 0.04$
Energy FWHM/eV	–	$3.46 \pm 0.01$	$26.18 \pm 0.08$
Energy midpoint/eV	–	$20.34 \pm 0.04$	$152.08 \pm 0.23$
$\Delta E/E$ (%) FWHM	16.75	$17.02 \pm 0.05$	$17.21 \pm 0.06$
Analyzer constant	6.35	$6.16 \pm 0.01$	$6.31 \pm 0.01$
Geometric factor (20° anode, 100% efficiency) (cm <sup>2</sup> sr eV/eV)	$1.7 \times 10^{-3}$	$8 \pm 1 \times 10^{-4}$	$8 \pm 1 \times 10^{-4}$

TABLE IV  
Simulated ELS peak count rates per 20° anode for typical Saturn magnetospheric conditions.

Location	Temperature (eV)	Density (cm <sup>-3</sup> )	Counts (s <sup>-1</sup> )
Solar wind	1	0.1	427
Magnetosheath	50	0.1	2137
Plasma sheet	100	30	854700
Magnetosphere	300	0.1	5128

the response is summed over the other two to produce the full width at half maximum in each dimension. A simulated geometric factor is also tabulated.

The susceptibility of ELS to background from solar UV was also simulated. Assuming a cosine law for reflection and a reflectivity of 0.5%, we found a rejection ratio of  $\sim 10^{-8}$ . A more sophisticated model based on the HEEA sensor was reported by Alsop *et al.* (1998), including the effect of shims introduced into ELS to reduce susceptibility to UV.

Calculations were performed to estimate the number of counts anticipated for particular plasma environments during the mission. Maxwellian distributions of specified density, temperature and bulk velocity formed the input to the ELS detector simulation program, which calculates the number of counts to be expected in each angular and energy bin. Table IV shows the count rates per 20° anode at the expected peak of some typical distributions. Note that for a Maxwellian distribution the peak count rate occurs at twice the temperature in eV.

#### 4.4. DETAILED DESIGN

##### 4.4.1. *Mechanical*

The sensor head assembly, which is generally cylindrical in cross-section, consists of an entrance collimator and baffles, ESA hemispheres, and MCP detector and anode. The sensor, mounted integrally with the ELS electronics compartment, is attached to the top of the IMS collimator assembly (Figure 6). This arrangement places the ELS aperture as far as possible from the surface of the Cassini spacecraft. Two flat side panels carry card guides for four electronics boards. Connectors on the board edges mate with a motherboard in the lower part of the compartment providing ease of access. Flexible circuit cables link the motherboard to the CAPS DPU interface connector, mounted on one of the flat side panels, and to the capacitor/amplifier board mounted behind the MCP anode. Pins on the back of the anode plug into sockets on the capacitor/amplifier board when the anode is installed.

The sensor head design incorporates very accurate relative positioning of the hemispheres (design goal 1%, equating to a total tolerance of 30  $\mu\text{m}$ ; Woodliffe *et al.*, 1998), which ensures accurate knowledge of the selected electron energy at all positions around the detector. Aluminum alloy milled to a wall thickness of 1.6 mm forms the outer shell of the instrument. An additional 3 mm of aluminum located directly above the MCP provides radiation shielding.

##### 4.4.2. *Detectors*

After leaving the ESA, electrons incident on the front face of the detector each cause an amplified cloud of charge collected by an anode at the rear of the detector (Figure 7). The detector consists of a chevron MCP pair with a gold-coated copper spacer 66- $\mu\text{m}$  thick positioned between the two plates. The purpose of the spacer is to lower the voltage required for a particular gain, hence allowing more scope for increasing MCP bias voltage as required over the mission. The effect of the spacer is also to improve gain uniformity over the whole detector. At operating voltage, the measured FWHM pulse height distribution is 130%. The resistivity of the glass in the MCP is low enough to allow the plate to respond to count-rates up to  $1 \times 10^4 \text{ mm}^{-2} \text{ s}^{-1}$  or approximately  $10^6$  electrons per anode per second, without saturation causing significant gain degradation. The MCP high voltage can be varied from 0 to +3.5 kV in steps of approximately 60 V. This allows the MCP bias to be increased throughout the mission to recover possible gain loss. The bias voltage at the input to the MCP is maintained at +150 V to ensure all electrons have sufficient energy to be detected. During calibration, the operational voltage on the MCP was approximately +2.4 kV.

Electrons leaving the rear of the MCP traverse a gap of 500  $\mu\text{m}$  before striking the anode. A voltage of +82 V applied between the anode surface and the back surface of the MCP optimizes spreading of the charge cloud leaving the MCP. The anode has eight discrete 20°-wide electrodes separated by 150  $\mu\text{m}$ . The active anode area is formed by 10  $\mu\text{m}$  thick gold on a Deranox 975 Alumina substrate.

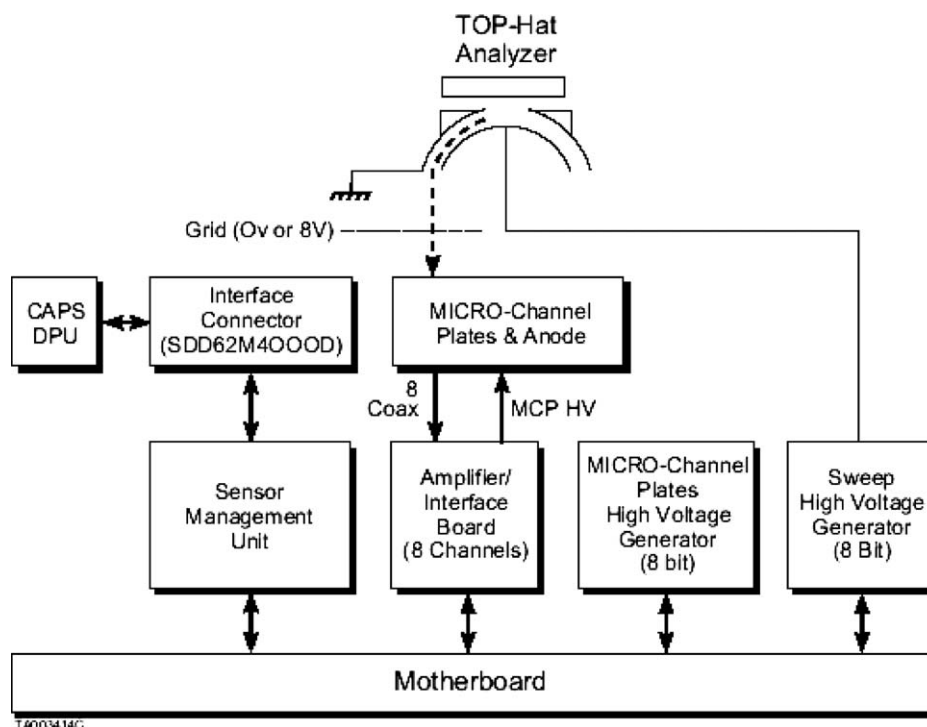


Figure 8. Schematic ELS electrical block diagram.

The area of the separator contacting the MCP is coated with  $10 \mu\text{m}$  of gold. A signal ground plane incorporated into the bottom layer of the multilayer ceramic provides electromagnetic screening of the anode from the analyzer structure.

#### 4.4.3. Sensor Electronics

A functional block diagram of ELS is shown in Figure 8. The electronics are accommodated on four circuit boards integrated to a single motherboard consisting of flexible and rigid sections. This design eliminates the need for an internal cable harness, and at the same time couples ELS to the CAPS Data Processing Unit (DPU) interface connector.

*Amplifier/Capacitor Board.* MCP pulses collected on eight anodes are passed to an equal number of Amptek<sup>®</sup> A111F charge amplifier/discriminators that convert raw signals above a predetermined threshold into 5 V, 300 ns logic pulses. Thresholds were set in hardware to  $3.4 \times 10^5$  electrons, which yields an equivalent level of 25 mV (into 2.3 pF), giving good rejection of electronic noise. A decrease in the threshold level by 2.5 mV increases spurious electronic noise counts by a factor of 10. (This relationship holds over a wide range of thresholds. MCP dark counts and penetrating radiation are the main remaining contributors to background.).

A further consideration in threshold selection was cross-talk that might couple MCP signals from one anode to the next. ELS anode cross-talk is below 3%,

which is not enough to induce a signal on its own, but could induce spurious counts when added to electronic noise. Convolving the two noise spectra (electronic and cross-talk) provided a check that showed that the chosen threshold was set correctly.

The A111F amplifiers show variation in deadtime with input pulse amplitude, especially within a factor of 2 of threshold, as well as a variation of output pulse width with input pulse amplitude, all of which were characterized during calibration. Front and rear MCP bias voltages are provided by Zener diodes, which require filtering at these low currents (around  $10 \mu\text{A}$ ). The MCP anodes are biased at high voltage (Figure 8) so signal pulses must be decoupled by high-voltage capacitors before the signal goes to the amplifiers that share the same circuit board with the HV bias/anode coupling circuitry. The HV section was carefully designed and laid out to support a maximum field of  $800 \text{ V/mm}$ .

*Sensor Management Unit (SMU).* The SMU receives and interprets sensor commands sent by the CAPS DPU and accumulates and transmits ELS data back to the DPU. It stores the sequence of high-voltage steps to be applied to the analyzer, the grid voltage setting, and the MCP voltage table. SMU circuitry supplies stimulation test pulses of variable amplitude and frequency to the amplifier/discriminator channels. Under control of the CAPS DPU, the SMU clock speed can be successively halved to lengthen the data acquisition period from 31.25 to 1000 ms/step, creating progressively longer energy sweeps. Furthermore, the sample deadtime can be varied between 25 and 12.5% of the sample period to increase counting rate capability at high rates.

*High Voltage Supplies.* The ELS contains two high-voltage supplies. A low noise supply biases the MCP at voltages up to  $+3.7 \text{ kV}$  at  $25 \mu\text{A}$  with 6-bit resolution. A second supply powers the ESA with 64 or 32 stepped voltage levels between  $+4200$  and  $+0.1 \text{ V}$ . This wide dynamic range meant that great care had to be taken at low output levels to avoid external noise affecting the pulse-width modulator that sets the voltage levels. A 12-bit digital-to-analog converter (DAC) controls the ESA output voltage using an “expanding DAC” technique to reach 16-bit resolution at low energies, thus achieving voltage accuracy of 1% or  $0.1 \text{ V}$ , whichever is greater. The supply steps at a minimum interval of 31.25 ms and settles in 8 ms. The entire HV converter section of the circuit board is shielded to protect low-voltage, low-noise circuitry from interference or possible breakdown.

#### 4.5. CALIBRATION

The ELS was calibrated in the Mullard Space Science Laboratory (MSSL) electron calibration facility developed for Cluster (Johnstone *et al.*, 1997). A photograph of ELS in the calibration system appears in Figure 9. A mercury lamp generates UV that strikes a gold layer deposited on a quartz disk. From this photoelectrons are extracted by applying a bias potential to the gold surface, creating an electron beam

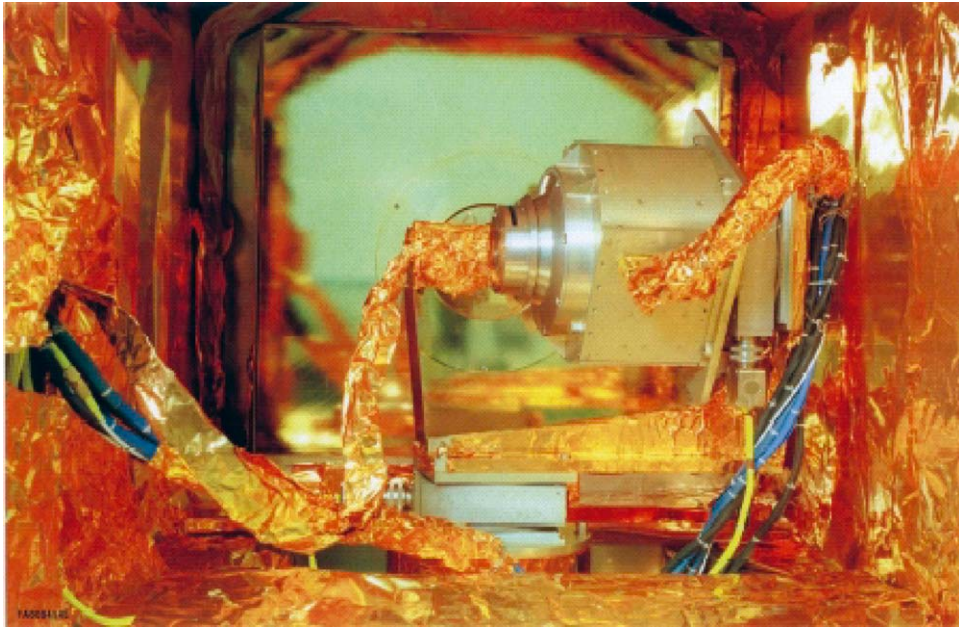


Figure 9. Photograph of the ELS flight unit in the MSSL calibration chamber. Gold-plated foil was used to prevent unwanted electrostatic charging in the calibration chamber.

15 cm in diameter with divergence less than  $1^\circ$  (at 1 keV) and good uniformity over the ELS aperture. During calibration ELS was mounted on a two-axis rotary table and turned to allow electrons from defined directions to enter (a short discussion of calibration theory can be found in Section 6.2.2). A  $\mu$ -metal shield inside the vacuum chamber shielded the calibration volume by reducing the residual magnetic field to less than 10% that of the Earth. Electron beams with energies above  $\sim 30$  eV showed minimal directional deviation.

Beam current measurements that provide absolute calibration were made with a faraday cup and picoammeter. During calibration sequences beam stability was monitored with a CEM. A tritium source provided a cross check after each sensor re-configuration to maintain consistency during calibration.

Calibration of the ELS engineering model has been described elsewhere (Linder *et al.*, 1998). Calibration of the flight model was made at ten electron energies between 2.3 and 16,260 eV. At each energy step a matrix of approximately  $500 \times 10 \times 10$  azimuthal  $\times$  elevation  $\times$  ESA voltage sweeps were taken (the actual number varied with energy step). Two basic types of data were taken: First a finely stepped elevation angular scan was made at constant energy and beam azimuth angle. Second, a full three-dimensional calibration (energy, elevation, azimuth) was obtained at defined resolutions in the three dimensions. The most detailed calibrations were made at 125 and 960 eV (Figure 10a and b). Each plot shows the ELS response as a function of elevation angle, summed over the other two dimensions. In each case

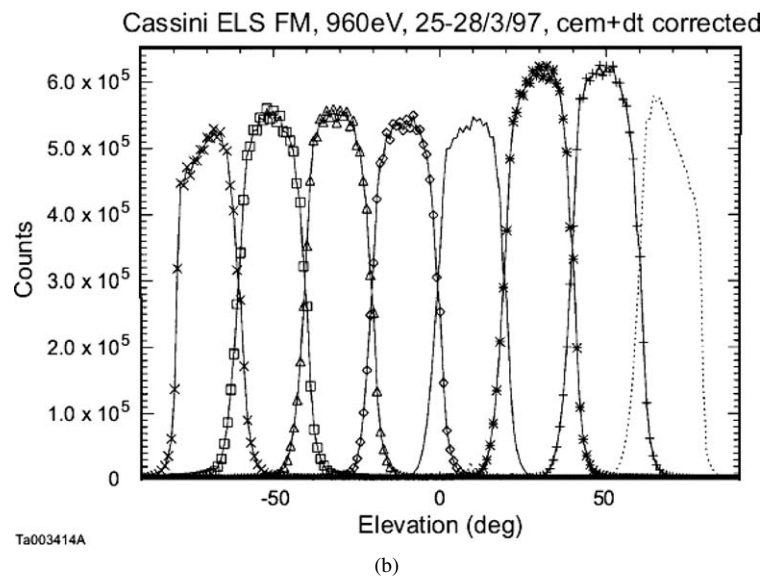
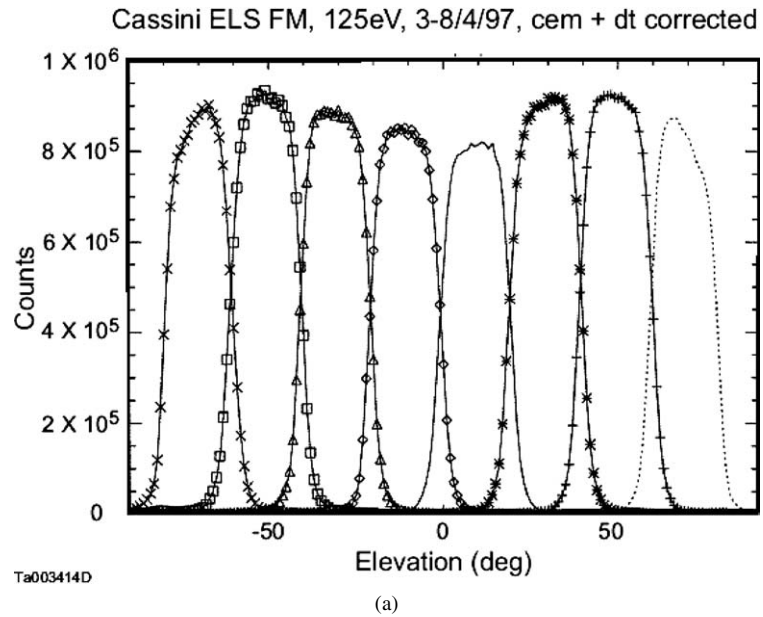


Figure 10. (a) ELS calibration data showing elevation response of the eight anodes at 125 eV. (b) ELS calibration data showing elevation response of the eight anodes at 960 eV.

some 150,000 data points, corrected for dead time and beam monitor readings, were summed to produce a plot. The eight anodes show a nearly uniform response with some loss of transmission at the two end anodes. This is to be expected because the grid holder cuts off incident trajectories at  $\pm 80^\circ$  elevation. A summary of 125 and

960 eV calibration data is included in Table III. Energy-angle scans with a 125 eV electron beam were made at the azimuthal center of each of the eight anodes. These are plotted in spectrogram format in Figure 11. Taken together, Figures 10 and 11 show that analyzer performance in three-dimensions is consistent from one anode to the next and deviates little from instrument simulations.

#### 4.6. PERFORMANCE

Calibration results in the previous section show that the mechanical construction accuracy of the analyzer (see Johnstone *et al.*, 1997), and therefore the anticipated scientific performance of the instrument, is excellent (Table V). Analyzer response widths agree with simulations and are close to those originally proposed. The geometric factor is based on a nominal MCP voltage setting.

Response of ELS to solar UV also was measured during calibration. In common with Alsop *et al.* (1998) we find energy-dependent rejection efficiency. Setting the grid potential to  $-8$  V and grounding the inner hemisphere made it possible to distinguish between photons themselves and photoelectrons reaching the MCP. The results showed an excellent rejection ratio (i.e. ratio of dark current background to background measured with UV entering the aperture) of  $\sim 10^{-10}$  at high electron energy and a worst case of  $\sim 10^{-8}$  at low energy. The intensity of Lyman  $\alpha$  at Saturn is approximately  $2.4 \times 10^9 \text{ cm}^{-2} \text{ s}^{-1}$  so the solar UV background at Saturn should be negligible. Using tritium or an electron beam as a source, end-to-end tests showed that secondary electron production inside ELS is minimal. ELS performance is summarized in Table V.

Section 9 of this paper contains examples of ELS data taken during Cassini's swingby of the Earth in August 1999 and its encounter with Jupiter in December 2000 to January 2001. Beginning with the jovian encounter, ELS (and CAPS as a whole) has been operating continuously and successfully when mission plans permit.

## 5. Ion Beam Spectrometer

The IBS is specifically designed to provide high resolution, 3-D measurements of the energy and angular distribution of any beamed ion populations encountered during the course of the mission. This instrument, based on an earlier design by Bame *et al.* (1978), has four principal measurement objectives: (1) afford context for saturnian magnetospheric studies by providing solar wind and bow shock measurements, (2) search for ion beams in the saturnian magnetosphere and study high-latitude source/loss cones in the cusp and auroral regions, (3) analyze thermal plasma distributions during transits through Titan's upper atmosphere, and (4) provide solar wind science data when the opportunity arises during the mission.

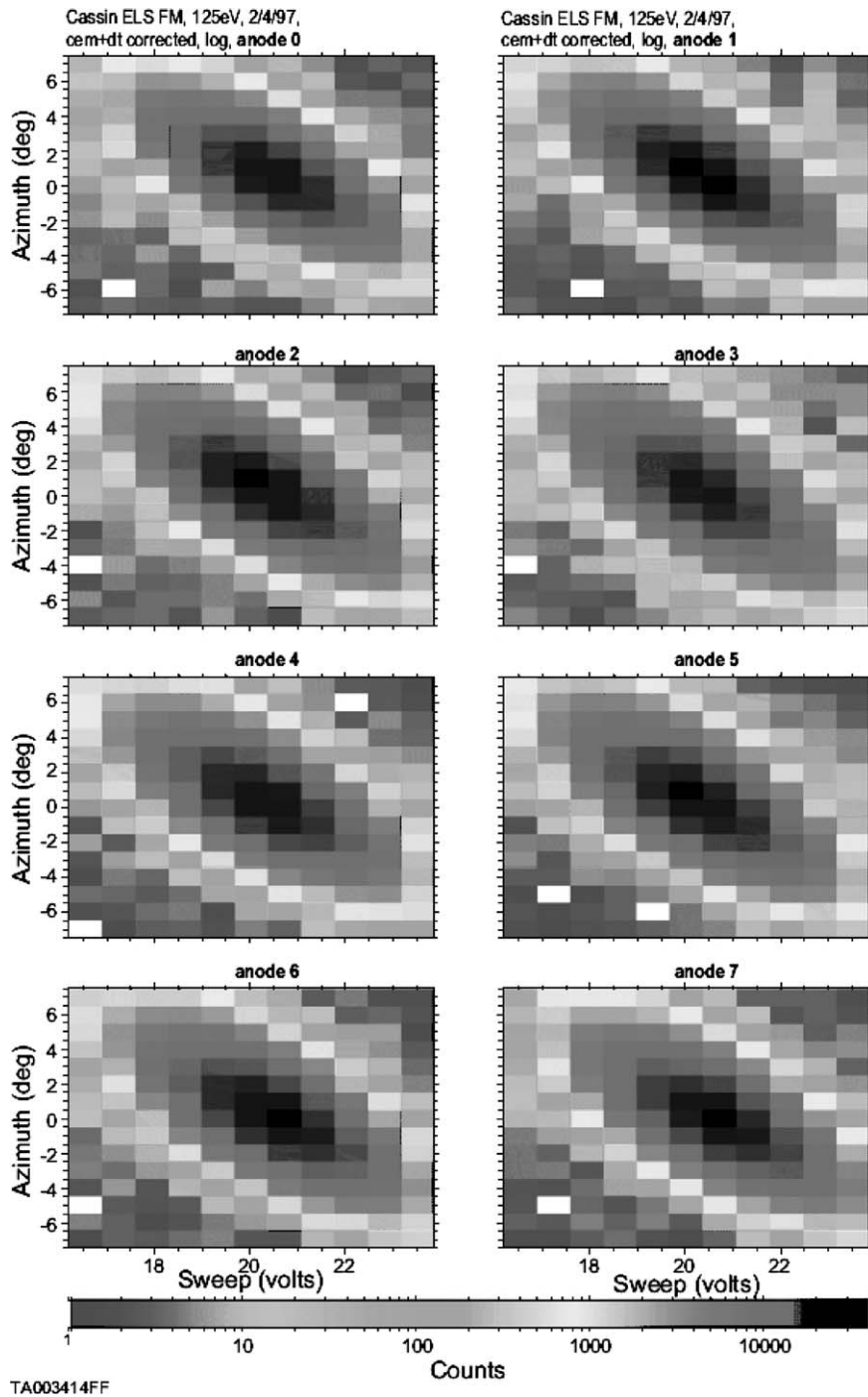


Figure 11. Spectrograms of ELS response in azimuth versus energy. Each spectrogram corresponds to an elevation passband shown in Figure 10a (125 eV beam).

TABLE V  
ELS detailed performance summary.

Parameter	Value
Energy range (eV)	0.6–28,250
Resolution $\Delta E/E$ (%)	16.75 <sup>a</sup>
Field of view (°)	5.24 <sup>a</sup> × 160
Angular resolution (°)	5.24 <sup>a</sup> × 20
Analyzer constant measured on FM at 960 eV (eV/V)	6.31
Geometric factor <sup>b</sup> (cm <sup>2</sup> sr eV/eV)	
(1) per 20° anode	8 × 10 <sup>-4</sup>
(2) per complete FOV	6.4 × 10 <sup>-3</sup>

<sup>a</sup>Value from simulation.

<sup>b</sup>Based on nominal MCP voltage setting.

### 5.1. PRINCIPLES OF OPERATION

Similar to the ELS, the IBS is based on the principles of a curved-electrode electrostatic analyzer. The primary differences, aside from its larger radius, is that the spherical IBS electrodes extend 178° from the entrance aperture to channel-electron multiplier detectors located at the exit. Positively charged ions enter the spectrometer through one of three flat, grounded apertures. They then acquire trajectories that are parts of conic sections due to the central electric force field present between the spherical electrodes (Figure 12). The inner plate has a variable (stepped) negative potential applied to it whereas the outer plate is at ground potential. Only those ions with a very small range of entrance energies and angles will transit the narrow gap between the nested hemispheres and be counted by particle detectors located at the ESA exit. Ions with too large energy or with angles of arrival more than  $\sim +1^\circ$  from the aperture normal will not be bent sufficiently by the electric field and will be lost on impact with the outer analyzer plate. Those with too little energy or with angles within less than  $\sim -1^\circ$  of the aperture normal will be pulled into the inner plate and also lost to the system. By sequentially stepping the potential on the inner plate and counting particles that transit the ESA, the energy spectrum of the ambient ion population can be readily determined.

A unique aspect of the IBS is the method used to obtain high-angular resolution 3-D velocity space measurements. On the basis of the crossed-fan FOV concept employed in an earlier solar wind ion instrument (Bame *et al.*, 1978), it is possible to obtain the required angular resolution by tilting the acceptance fans of each aperture 30° relative to the others (Figure 12). Because each of the three fans requires only a single non-imaging detector, it is possible to measure the velocity distribution of

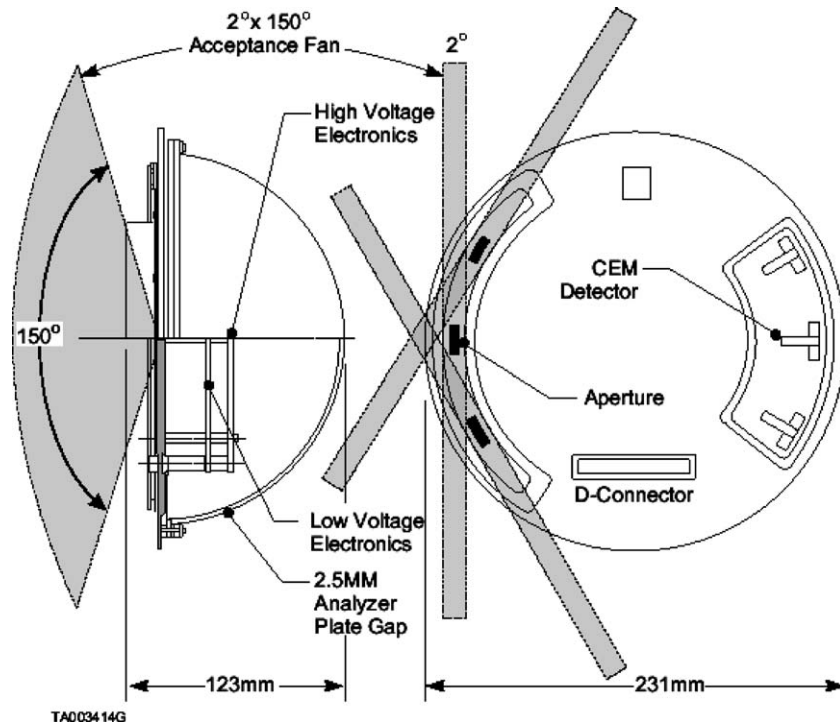


Figure 12. Elevation and plan views of the IBS sensor. Note that the three FOV fans are tilted by  $30^\circ$  and offset from one another in the vertical direction. The cutaway drawing at left shows power supplies mounted within the IBS analyzer dome.

the ambient plasma with a minimum of complexity and resources. Information on the instantaneous viewing direction of each of the fans combined with the energy analysis provided by the ESA provides a nearly complete energy-angle distribution of the ambient plasma ion population.

## 5.2. DETAILED DESCRIPTION

For a variety of reasons, the IBS was allocated minimal resources of approximately 1 kg and 1 W and optimized to near those values (Table XI). These constraints, plus a requirement to be able to search almost the entire unit sphere for ion beams and analyze them with adequate energy and spatial resolution, dictated the overall IBS design.

Key IBS sensor data and dimensions are given in Table VI. The choices were dictated by the requirement for high angular and energy resolution while simultaneously obtaining sufficient particle throughput needed to measure narrow solar wind beams expected at 9.5 AU. To minimize weight but still provide adequate radiation shielding, the inner ESA hemisphere (made from aluminum) was optimized to a

TABLE VI  
IBS key sensor data and dimensions.

Parameter	Value
ESA type	Hemispherical
Mean radius	10.00 cm
Plate spacing	0.25 cm
Analyzer constant	19.0
Plate bending angle	178°
Aperture (curved)	0.25 cm × 1.50 cm
Aperture radius of curvature	10.0 cm
Detector	CEM

thickness of 0.7 mm and that of the outer to 0.8 mm. The tolerances for manufacturing the hemispheres and aligning them relative to one another were quite stringent. Vilppola *et al.* (1993) have shown through simulations that inaccuracies of  $\sim$  few tens of  $\mu\text{m}$  are important.

Normally, the interior surfaces of the hemispheres would have been grooved and blackened to suppress UV photons that could scatter into the detectors, but grooving of the large thin plates is impractical. Originally, we avoided blackening the interior analyzer gap because the large ESA bending angle of 178° requires numerous bounces before photons could be transmitted to the detectors, which should greatly suppress unwanted background. In addition, we expect to encounter very low-energy ions (1 to a few eV) in Titan’s ionosphere. Transport of  $\sim$ 1 eV ions through the relatively long path length of the IBS ESA ( $\sim$ 315 mm) necessitates a highly uniform field between the plates. We therefore wished to avoid using the usual Ebanol-C black coating used on ELS because of the possibility of introducing surface potential “patchiness” in the analyzer gap. (For 1 eV ions the inner analyzer plate potential is only  $-50$  mV and a variation of only a few mV in surface potential along the path would be unacceptable). Therefore, the ESA hemispheres were not grooved or blackened but were instead carefully coated with pure gold, a poor reflector of UV. However, during early testing it was found that UV transmission through the ESA was much higher than that expected at high-polar angles, apparently due to “channeling” along minute machining grooves that remained in the hemispheres. As a consequence, in the end the hemispheres were blackened using the Ebanol-C process and UV rejection fell to  $\sim 10^{-10}$ . None of the anticipated problems associated with Ebanol actually occurred.

As mentioned above, the unique aspect of the IBS is its method of determining 3-D plasma velocity space distributions by means of crossed-fan geometry. There are three curved  $2.5 \times 15$  mm apertures in the IBS faceplate (Figure 12), each with a nominal acceptance fan of  $\pm 1.5^\circ$  FWHM in azimuth (set by the ESA characteristics) and  $\pm 75^\circ$  FWHM in elevation angle (set by the apertures) from the normal to the

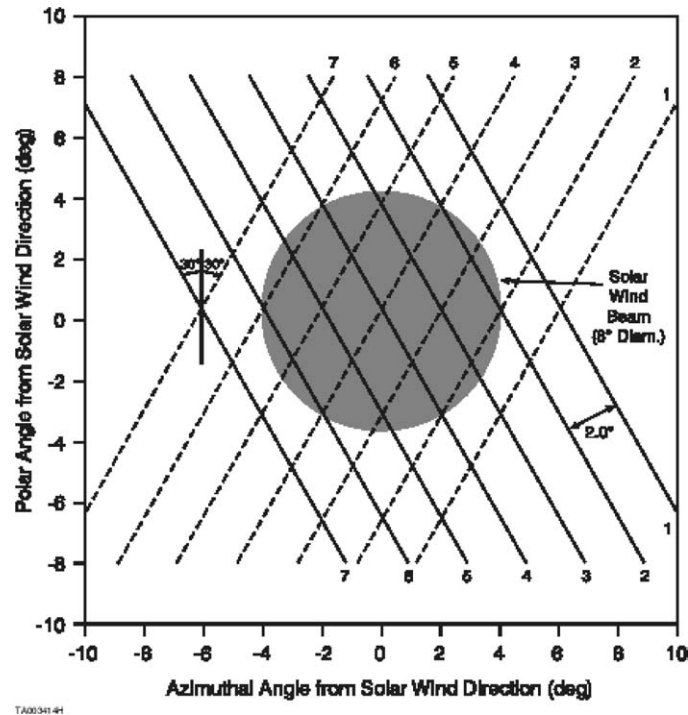


Figure 13. Velocity space coverage of the IBS crossed fan electrostatic analyzer. The solid and dashed lines represent the centers of the two slanted fans. The central aperture fan is omitted for clarity.

plane of the aperture. If we define the middle aperture as being along the  $0^\circ$  radius from the center of the instrument faceplate, the other two apertures are located at  $\pm 30^\circ$  relative to it. There are three CEM detectors located  $180^\circ$  around the faceplate from each of the apertures, i.e. in the position where ions entering the apertures from any transmitted direction come to a focus. The FOV of the middle aperture is oriented such that its long (polar) dimension is parallel to the azimuthal (Z) axis of the CAPS actuator. The FOV of the other two apertures are therefore “crossed” with inclinations of  $\pm 30^\circ$  with respect to that of the middle aperture.

Ions transmitted through each of the apertures are detected by the corresponding CEM, giving an instantaneous 1-D view of an ion distribution. A 3-D measurement of the plasma velocity distribution can be built up from each aperture by simultaneously sweeping the energy passband of the instrument and rotating the actuator (ACT) and/or the spacecraft itself. Figure 13 illustrates how spatial coverage is obtained. Data from the three individual acceptance fans are combined (Figure 14) and used to obtain a 3-D distribution measurement with angular resolution as high as  $1.4^\circ \times 1.4^\circ$  (FWHM). The maximum angular resolution falls off gradually with increasing polar (elevation) angle due to the natural broadening of the azimuthal acceptance angle as polar angle increases from the aperture normal (see Figure 17 below).

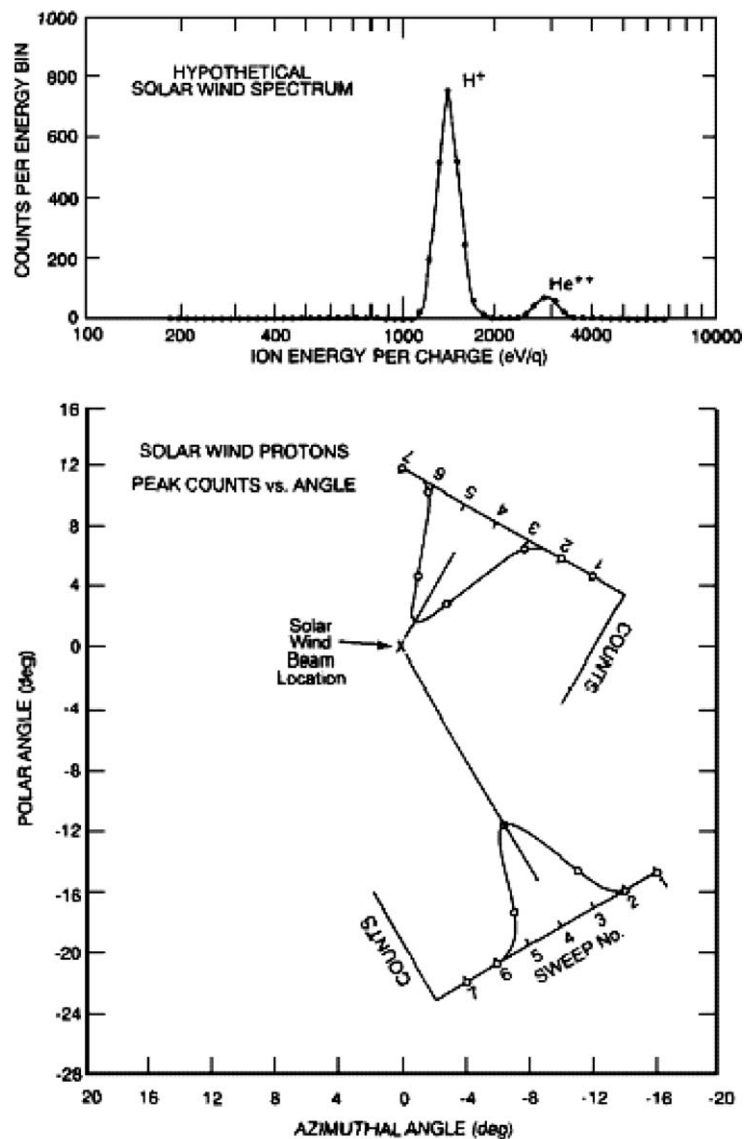
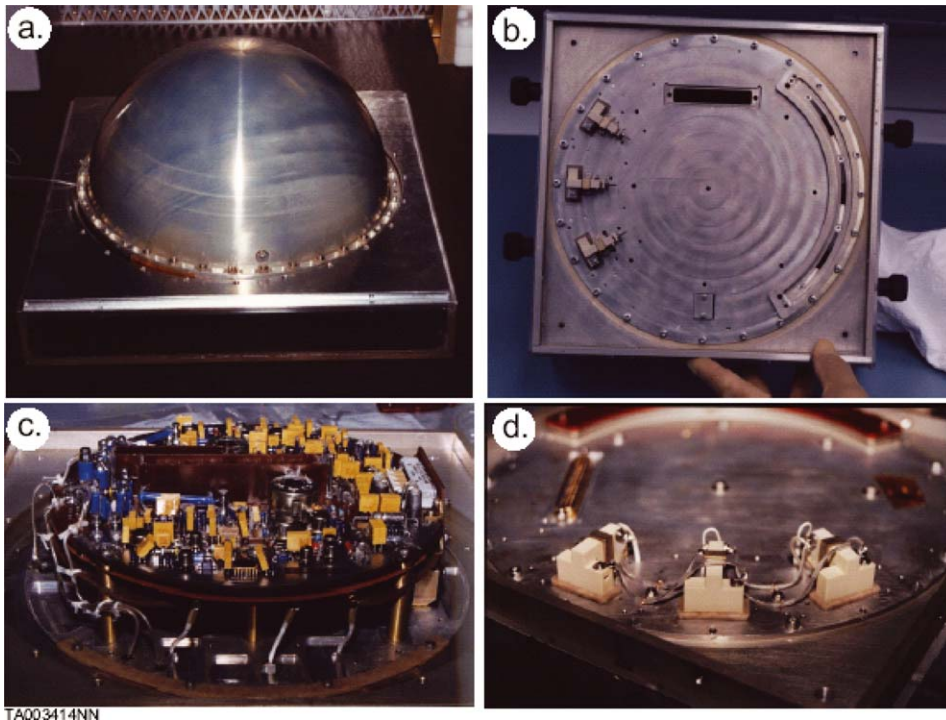


Figure 14. The upper figure shows a hypothetical input solar wind energy spectrum for a single fan. The lower figure illustrates the method for determining ion beam position in velocity space from crossed-fan measurements (after Bame *et al.*, 1978).

It can be seen that two fans would be sufficient to obtain the required measurements. However IBS incorporates three fans for a number of reasons. One is redundancy: if one of the three CEMs fails, it is still possible to obtain fully 3-D results. If two channels fail, useful 2-D data can still be obtained. Second, given an unobscured FOV, IBS can potentially obtain 3-D coverage over  $\sim 80\%$  of space.



*Figure 15.* Views of the IBS flight unit during assembly. (a) The completed unit seen from the rear showing the outer hemispherical plate. (b) View of the inside of the front plate of IBS showing the three CEM detectors on the left and aperture holes on the right. (c) Details of IBS high-voltage supplies that are mounted inside the ESA inner dome. (d) Details of the ceramic CEM detectors.

The three matched detectors used in IBS (Figures 12 and 15d) are custom-built CEMs chosen for their rugged construction out of solid ceramic, their high-gain characteristics (typical plateau  $\sim 10^8$ ), and their availability in nearly any desired form factor (the manufacturer is Dr Sjuts Optotechnik GmbH of Germany). The input funnel interior dimensions are  $5 \times 20$  mm, which is more than adequate to intercept all of the ions converging at each of the sensor's three focal points. Ninety percent transmission grids are stood off from the front of the CEM funnels and biased negatively with respect to the funnels to minimize secondary electron loss. The input assembly (grid and funnel) is biased at negative high voltage so that all transmitted ions receive post-acceleration equivalent to the CEM bias. A CEM responds to an incoming ion by emitting an electron charge pulse at its exit, which is biased at about  $-100$  V. Electrons are attracted to the anode, which is at signal ground, and are then fed to an Amptek A111F hybrid preamplifier/discriminator. The resulting output pulses are routed to counters located in the CAPS DPU where samples are compressed and inserted into the telemetry stream by the CAPS Central Processing Unit 1 (CPU1).

### 5.3. RAY-TRACING AND MODELING RESULTS

Initial modeling of the IBS was chiefly concerned with determining manufacturing tolerances required to achieve the desired energy-angle resolution and transmission efficiency of the ESA (Vilppola *et al.*, 1993). Analysis of simulation results showed that it was necessary to align the two ESA hemispheres relative to one another with an accuracy of better than  $\sim 25\mu\text{ m}$  to obtain the desired energy resolution of  $\Delta E/E = 0.015$ . Furthermore, deviations of the ESA plate surfaces could not depart from perfect sphericity by more than  $300\mu\text{ m}$  (0.3% of plate radius) if  $>90\%$  transmission efficiency was to be maintained. Guided by this analysis, fabrication, assembly and metrology techniques were developed to help ensure that individual IBS hemispheres were within specification. Unfortunately, it was not possible to directly measure the inner surfaces of the analyzer gap once the ESA was fully assembled. Thus unexpected irregularities that might be introduced during assembly potentially could go unnoticed. Laboratory calibrations were employed to determine whether specifications had been maintained and sensor response conformed to expectations.

### 5.4. ELECTRONICS

A schematic block diagram of the IBS electronics is presented in Figure 16. All of the electronics are mounted on two circular circuit boards housed in the ESA hemispherical cavity (Figure 15c). The upper board contains both the ESA and the CEM high-voltage power supplies, whereas the low-voltage amplifier/discriminators, test pulser, and digital-to-analog converters (DACs) are contained on the lower board. The electrical interface from the IBS to the CAPS DPU is a single 62-pin connector. The weight of the internal IBS electronics is 42% of the total weight of the IBS sensor, or 490 g.

The CEM HV supply, which provides a negative bias voltage to the three IBS detectors in parallel, is commanded by an 8-bit word over a range of 0 to  $-4.0\text{ kV}$ . The ESA supply biases the inner ESA hemisphere with a stepped negative potential that determines the instantaneous energy of transmitted ions. For IBS to be able to function as desired, the ESA HVPS must cover the voltage range  $-0.05$  to  $-2600\text{ V}$  in 1.284% increments with a time between steps of 7.8125 ms. In order to have sufficient resolution over the entire voltage range, the ESA supply was designed with three ranges ( $-0.05$  to  $-1.85\text{ V}$ ,  $-1.85$  to  $-69.6\text{ V}$ , and  $-69.6$  to  $-2600\text{ V}$ ) each of which is 12-bit controllable. This results in a total of 12,288 possible voltage steps although only 852 logarithmically spaced steps are required for full coverage of the voltage range with 1.284% spacing. During operation a 14-bit data word controlling the ESA stepper supply is written to a latch in the IBS electronics every 7.8125 ms (one-eighth of the IMS stepping interval of 62.5 ms). The basic operational mode consists of a 255-step voltage scan (corresponding to an

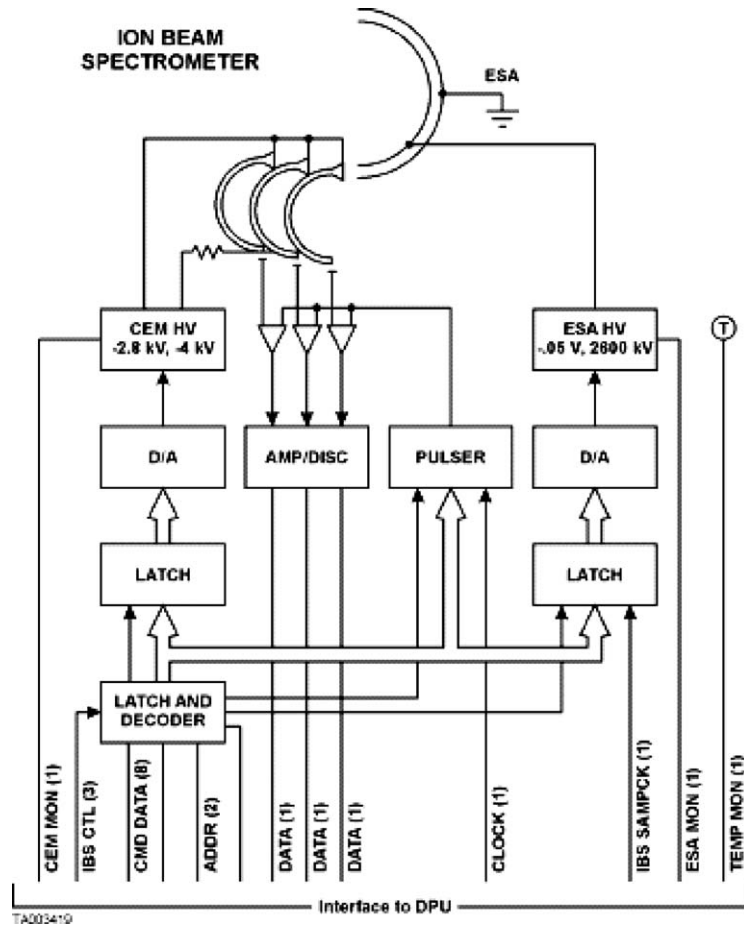


Figure 16. Schematic IBS electrical block diagram.

energy scan) lasting 2 s. In planned operations this may consist of a single, 255-step scan, two 127-step scans, or half of a 510-step, interleaved scan. Data values for generating the energy sweep are stored in CPU1 memory. Energy sweep steps are verified by returning an analog monitor voltage that is digitized and entered into the CAPS housekeeping data.

### 5.5. CALIBRATION

Initial calibration results showed that IBS responds as expected (Figure 17) except for the presence of a few small but unusual features. Of these, a double-bend in the energy-polar angle response (Figure 17c) is the most notable. To address these findings, a more accurate simulation of the sensor was developed and used

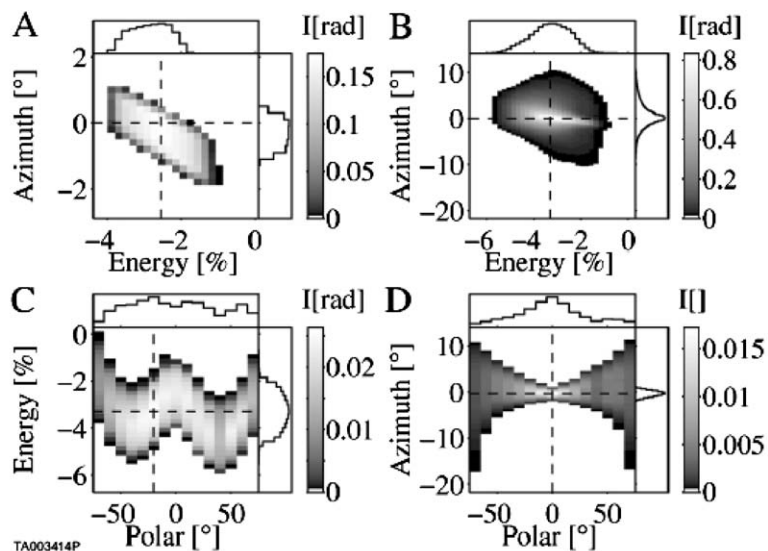


Figure 17. Spectrograms summarizing detailed calibration of the IBS.

to investigate IBS response in more detail (Vilppola *et al.*, 1996). Improvements made to the model included addition of curved apertures (Figure 15b) at the correct standoff distance from the ESA plates, introduction of fringing fields, and a realistic description of the ion beam that matched that used in calibration. These upgrades to the model did not, however, account for the bend feature of Figure 17c. A further refinement of the model allowed the introduction of slight asymmetries in ESA plate geometry (Vilppola *et al.*, 2001). The resulting simulations with asymmetric hemispheres and a slight (few tens of microns) misalignment of the two hemispheres produced good agreement with laboratory results. Although the flight sensor's ESA plates may indeed be slightly misaligned as suggested by simulations, the response of the engineering model IBS is almost identical to the flight model, which is surprising if a random misalignment occurred. Moreover, the responses of the three individual fan apertures in both IBS models are also very similar. This suggests that the unexpected calibration response is due to a small systematic error in alignment or is inherent in the overall electro-optic design and not a function of alignment accuracy. Our latest simulations suggest that a small systematic manufacturing fault might be to blame.

Calibration of IBS took place in ion beam facilities at Los Alamos and SwRI (the same facilities that are used to calibrate IMS). The work at Los Alamos concentrated on angle–angle and angle–energy responses while absolute energy and sensitivity calibrations took place at SwRI. At Los Alamos ions were produced in a radio-frequency discharge ion source and then accelerated down a 3-m flight tube into the calibration chamber where IBS was located. Both external supplies and the IBS internal power supplies were used in calibration. A nitrogen beam was typically used

which was accelerated to between 0.3 and 60 keV. Beam location and uniformity were measured but not absolute ion current. Typical operating pressures were in the low  $10^{-8}$  Torr range.

The ion current extracted from the Los Alamos source was quite stable but not easily varied over a wide dynamic range. Therefore a series of slits were employed to adjust the current delivered to the target chamber. IBS was mounted on a stand whose orientation could be adjusted in one translational axis (across the beam) and two rotational axes. Thus the incident ion beam could be made to impinge on the IBS aperture at any desired combination of elevation and azimuthal angles. All of the diagnostic, motion control and data acquisition systems were computer-controlled. During a typical calibration run, three separate 1-D scans in energy, elevation and azimuthal angle would be taken across the center of the response function. Three central 2-D cuts through the response function would then be taken, followed by a series of energy-azimuth cuts along the elevation axis at  $10^\circ$  intervals. Finally, data were corrected for deadtime losses and variation in the beam current during the calibration run. Angular data were transformed from laboratory to spacecraft coordinates. Figure 17 shows an example of the IBS energy-angle response to a 10.0 keV beam of  $H^+$  ions.

After calibration at Los Alamos, the IBS was integrated with the CAPS flight instrument and underwent checks of calibration in the ion beam at SwRI. The latter, which is similar to that at Los Alamos, is described in Section 6. Typical beam spread at SwRI was  $\Delta\theta \approx 0.2^\circ$  and  $\Delta E/E \approx 0.005$ . One difference in the two calibration systems was important: the integrated CAPS unit was positioned to calibrate mainly IMS. Thus the rotation axes of the calibration goniometer were centered on the IMS FOV. Since the plane of the IBS apertures is offset 32.0 cm from the central axis of the IMS and ELS sensors (Section 7.1), the IBS aperture plane was neither co-planar nor co-aligned with the other two sensors: Any rotation of CAPS tended to move the IBS FOV out of the ion beam. The displacement of the aperture through the small IBS maximum azimuthal angular acceptance of  $\approx \pm 2^\circ$  was less than 1 cm, well within the diameter of the calibration beam as seen from IBS. Thus only calibrations of the energy response at azimuth = elevation =  $0^\circ$  and of absolute sensitivity (see the discussion in Section 6.6 below) were possible.

## 5.6. PERFORMANCE

The detailed results of IBS absolute and elevation calibrations with an  $N^+$  beam are summarized in Table VII. There are slight but consistent trends in the analyzer constant  $K$  and in the energy and angle resolutions. Taken at face value, the trend in  $K$  suggests that the analyzer plates appear to be closer together at higher voltages, or, alternatively that the voltages produced by the IBS ESA supply are too low by 0.26% at 0.25 keV and too high by 0.47% at 25 keV. The latter would be within the allowed error range of the supplies. Trends in energy and azimuthal angular resolution are toward slightly higher resolution at higher energies. By extrapolating

TABLE VII  
IBS detailed performance summary.

Parameter	Value
Energy range (eV/e)	0.95 to 49,800
Energy resolution ( $\Delta E/E$ ) <sub>FWHM</sub>	0.014
Field-of-view ( $^{\circ}$ ) <sub>FWHM</sub>	$1.4 \times 150$
Angular resolution ( $^{\circ}$ )	$1.4 \times 1.4$
Analyzer constant (average)	19.0
Geometric factor (cm <sup>2</sup> sr eV/eV)	$4.7 \times 10^{-5}$
Effective area (cm <sup>2</sup> )	0.081
Dead time ( $\mu$ s)	0.86

data taken between 0.25 and 30.0 keV we have estimated performance for all but the lowest ion energies.

Initial absolute efficiency measurements made at SwRI found an efficiency of about 30% of the calculated value. It is possible that this disagreement arises in the beam system's ability to measure total beam current for a tightly collimated FOV such as IBS's. The beam current monitor is located 1-m upstream from the IBS aperture and 4 m from the ion source. The monitor's acceptance in angle, energy, and spatial coordinates are much larger than that of IBS, particularly in the elevation direction. This could cause the monitor to overestimate the amount of beam actually filling the IBS acceptance phase space.

IBS has performed extremely well since initial operations began during the Earth encounter in August 1999. Examples of IBS data taken at Earth and the encounter with Jupiter in December 2000 to January 2001 are presented in Section 9. IBS has been operating continuously since late 2000, with the exception of an 8-month gap in 2003, when the CAPS instrument was off while spacecraft and instrument flight software were being tested.

## 6. Ion Mass Spectrometer

The IMS is designed to carry out three primary functions in response to CAPS scientific objectives. In describing and discussing the IMS it helps to rank these functions in rough order of time resolution: (1) Obtain rapid measurements of the velocity distributions of major ion species up to 50 keV. These data will be used to determine magnetospheric boundaries, structures in the region of Titan and icy satellites, and particle acceleration regions. (2) Measure the atomic, molecular, and, where possible, isotopic composition of saturnian plasmas in order to determine chemical and physical processes leading to the creation, transport, and loss of plasma populations. (3) Carry out a thorough survey of general characteristics of the magnetosphere including its composition.

## 6.1. MEASUREMENT REQUIREMENTS AND APPROACH

### 6.1.1. Requirements

Our approach to designing the IMS was taken largely from the three requirements given above. The first centers on measurement of rapid changes in the distribution functions of the dominant ion species ( $>1\%$  of the total), for example,  $\text{H}^+$ ,  $\text{H}_3^+$ ,  $\text{He}^{++}$ ,  $\text{O}^+$ ,  $\text{OH}^+$ ,  $\text{H}_2\text{O}^+$ , or  $\text{N}_2^+$  depending on location in the magnetosphere (see discussion in Section 2). Characteristic scales are, for example, on the order of the time needed to cross plasma boundaries ( $\sim$ few seconds). It is important to realize, however, that characterization of rapid plasma changes is limited by the performance of the ACT and by spacecraft motions (nominal rotation rates of  $1^\circ/\text{s}$  and  $<0.15^\circ/\text{s}$ , respectively). Thus the highest time resolution for two-dimensional snapshots in energy-elevation is a few seconds, while for 3-D scans the resolution is  $\sim 3$  min. A comparable time base requirement ( $\sim$ minutes) is set by the combination of spacecraft relative velocity and target body radius. In order to fulfil the second requirement IMS must return energy-resolved high-resolution  $M/Q$  spectra from which minor ion species ( $<1\%$  of the total) can be identified and their relative abundances measured. This function is more nearly like that of a traditional mass spectrometer. The typical time scale for this measurement should be roughly that of the 3-D measurement (a few minutes) in order to sample the entire region of phase space available at any one time. In addition to survey products, the high-resolution  $M/Q$  versus  $E/Q$  data will serve as a ground truth check of the high time-resolution ion data.

A complete understanding of the saturnian magnetosphere requires knowledge of its average characteristics as a function of both time and position. Because of the large number of candidate plasma sources (see Section 2), ion composition can be expected to be a strong function of location. This leads to the third primary requirement placed on IMS, namely an accurate, contiguous survey of as many ion species and their energy distributions as possible. This survey will be carried out under the aegis of the Cassini magnetosphere and plasma science (MAPS) working group to which CAPS contributes. Although limited in some ways by telemetry rate considerations, we have developed a special survey mode to optimize CAPS contributions to this survey (see Section 8.1).

### 6.1.2. Approach

There is a well-known tradeoff in conventional mass spectrometry between sensitivity and mass resolution. In order to build a space flight spectrometer several issues must be addressed: (1) Magnetic mass spectrometers do not usually provide high resolution at ion energies above  $\sim 3$  keV because the size of the spectrometer grows proportionately to ion velocity. Quadrupole spectrometers (e.g., Waite *et al.*, 2004), another alternative, function well only up to energies of  $\sim 0.1$  keV. (2) Although energetic particle telescopes are able to distinguish ion mass and mass/charge, they typically are insensitive to heavy ions such

as  $O^+$  below  $\sim 50$  keV/e (e.g., Krimigis *et al.*, 2004). (3) Sensitivity is proportional to aperture acceptance (solid angle and area), so it is essential to develop a sensor having both a large FOV and a large acceptance area. Neither of these factors is conducive to good resolution in conventional mass spectrometers.

Given these considerations, our approach was to choose a novel technique based on isochronous (time-focusing) mass spectrometry based on carbon foils. Using carbon foils as a means of generating timing signals in TOF space instruments is well known (Gloeckler and Hsieh, 1976; Hamilton *et al.*, 1990; Young *et al.*, 1991). What is novel about the IMS design is its capability for isochronous performance over a FOV as large  $360^\circ$  (McComas *et al.*, 1990; McComas and Nordholt, 1990). The combination of carbon foil and isochronous methods solved several measurement problems. In the first place, all other things being equal, aperture size determines mass resolution in conventional mass spectrometry. Here, however aperture size is determined by carbon foil size, which in principle can be made as large as desired. Secondly, the foils can be arranged in an axisymmetric geometry that permits the mass spectrometer to view  $360^\circ$  if desired, thus increasing solid angle of acceptance and FOV appreciably. Finally, a third feature of the IMS TOF optics is that the combination of a high-resolution time-focusing linear electric field (LEF) with time-dispersive optics yields not only high-mass resolution but also high sensitivity because all daughter products leaving the carbon foil can be detected.

## 6.2. PRINCIPLES OF OPERATION

### 6.2.1. Overview

To achieve IMS measurement goals we have matched the properties of a toroidal ESA to those of the TOF analyzer. The combination of an ESA with carbon-foil based TOF measurements has been previously developed and flown in space by Gloeckler and colleagues (see Gloeckler and Hsieh, 1976; Gloeckler *et al.* (1995, 1998); Hamilton *et al.*, 1990), Hovestadt *et al.*, 1995, and by Young *et al.* (1991, 1998). Early development of the LEF concept by Gloeckler *et al.* (1995) resulted in a high-resolution 1-D (in energy) isochronous instrument used to measure the collimated flow of the solar wind. However, McComas *et al.* (1990) and McComas and Nordholt (1990) were the first to describe the principles and operation of a cylindrically symmetric LEF analyzer capable of making 2-D energy-angle measurements. McComas *et al.* (1998) and Nordholt *et al.* (1998) further describe the LEF application to IMS.

Ions initially enter the top-hat portion of the ESA through a grounded collimator (Figure 18). A flat circular plate truncates the inner ESA toroid at the point where it joins the top-hat section. There are two advantages to toroidal geometry: (1) Toroids have two radii of curvature that independently control ion focusing within the TOF section (in spheres the two radii are degenerate and equal, in cylinders one radius

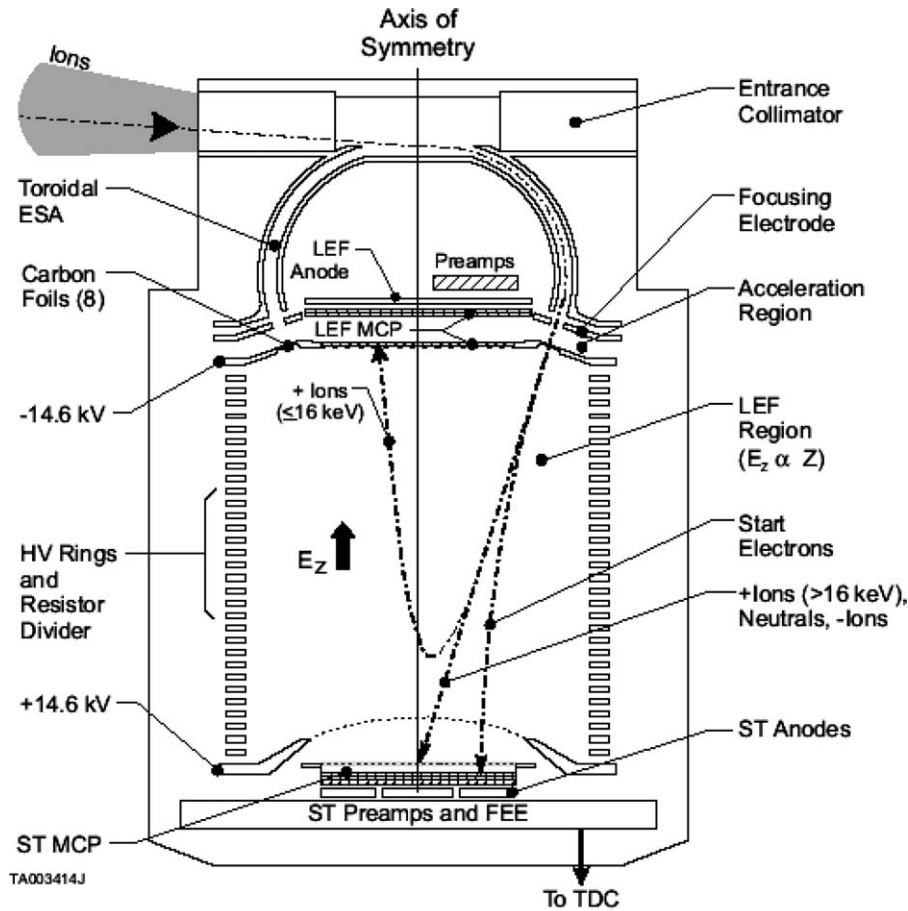


Figure 18. Schematic diagram of the IMS optics, detectors, and placement of high-speed FEE electronics.

is infinite). (2) The top-hat entrance aperture of a toroid like the one used in IMS is larger per unit of ESA plate surface area than for a comparably sized spherical top-hat, giving higher sensitivity per unit of sensor weight (Wollnik, 1971; Young *et al.*, 1988). In the elevation plane (orthogonal to that of Figure 18), ions are formed into a beam by a combination of vanes in the entrance collimator and field-correcting slits (one per  $20^\circ$  pixel) at the exit of the ESA. Figure 19 illustrates the collimated FOV and mapping to the two IMS detectors.

A voltage applied to the inner ESA electrode creates an electric field in the top-hat that deflects ions into the toroid. As with ELS and IBS, only particles within a particular range of  $E/Q$  and direction of arrival are transmitted through the ESA to the TOF analyzer. Ions that successfully exit the ESA are accelerated by  $-14.56$  kV into one of eight ultra-thin ( $1\sim 1.5$   $\mu\text{g}/\text{cm}^2$ ) carbon foils distributed

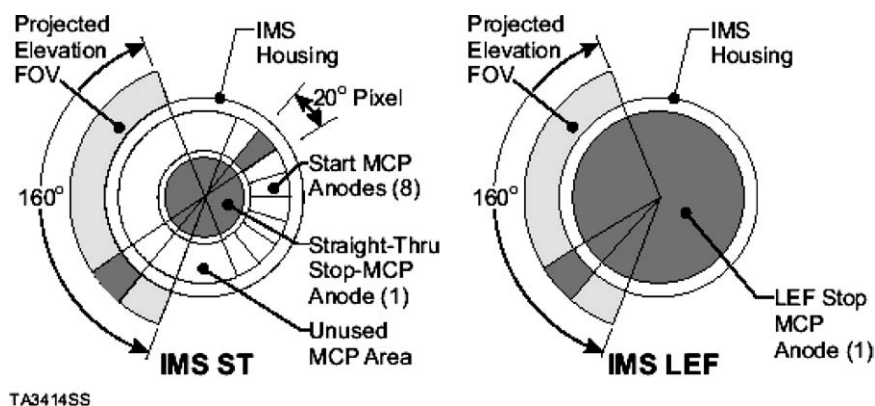


Figure 19. The IMS field of view in the elevation plane showing the mapping of angular pixels to the IMS detectors.

around the entrance to the TOF analyzer (one foil per angular “pixel”). Ions fall through the accelerating field, gaining sufficient velocity perpendicular to the foil so that they penetrate the foils even at the lowest external energies ( $\sim 1\text{eV}$ ). Higher post-acceleration voltages would naturally be desirable, but would have driven up instrument size, mass, and power in addition to risk. (The IMS supplies are capable of delivering  $-16.0\text{ kV}$  and the optics are rated at  $-15.0\text{ kV}$  but are tested much higher. However for operational reasons the IMS voltages are set at  $\pm 14.56\text{ kV}$ .)

### 6.2.2. Instrument Theory

Figure 20 shows the equipotential distribution in the LEF along with typical particle trajectories. Ions enter from below, normal to the foil surface (scattering in the foil is neglected in this simple presentation). From the figure it is clear that the shape of the LEF near the foil area pushes electrons outward toward the outer edge of the “straight-through” (non-mirroring) ST detector where “start” timing events are recorded. Negative ions have higher momentum and are pushed only slightly outwards in the upper part of the field. Neutrals of course follow a rectilinear path through the field, while positive ions below  $\sim 15\text{ keV}$  (external energy) are reflected in the field. The following first-order theory of instrument performance applies only to characteristic trajectories traveling through the central portion of the LEF.

*Ion Mass Identification.* In the simplest case of an atomic species that does not break up in a foil and that can be identified by a single TOF peak, the parent ion corresponds directly to an identifiable ion of mass/charge ( $M/Q$ ). The distinction of mass per charge is important because IMS is not able to identify mass or charge separately, only the ratio. Identification of parent molecular species (consisting of two or more atoms) is more complicated and follows a multi-step process. First, individual peaks are identified in the TOF spectrum on the basis of calibrated properties such as peak centroid and shape. Second, patterns or combinations of

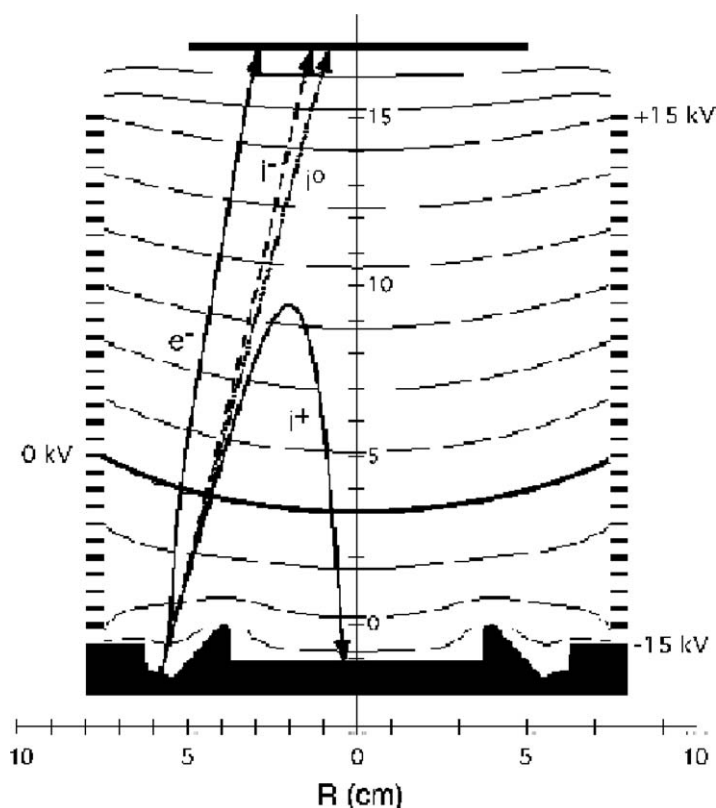


Figure 20. Characteristic trajectories in the LEF obtained by ray-tracing.

daughter peaks are recognized and the daughter peak identified (e.g., a  $C^+$  peak that might originate in any number of carbon compounds). Finally, the relative abundances of any daughter species are used to identify the parent molecule. (It may be possible with experience to go directly from the first step to the last.)

Ions with total energy  $E$  and charge  $Q$  at infinity are accelerated by a potential  $U_A$ , giving them a total energy  $E + QU_A$  or, more conveniently,  $E/Q + U_A$  since the ESA measures  $E/Q$  rather than  $E$ . The ions strike the carbon foil, exiting with energy “per charge”  $\sigma(E/Q + U_A)$  (for neutral species the total energy is used). The factor  $\sigma$  accounts for energy losses due to collisions. Although molecular species will break up in the foil, the daughter products all travel with approximately the same center of mass velocity, allowing us to write the following equation for any peak measured at time  $T$ :

$$M/Q = (\sigma/k_1^2(E/Q + U_A)T^2L^{-2}) \quad (1)$$

where  $k_1 = 22.85$ ,  $E/Q$  and  $U_A$  are measured in kV,  $M/Q$  is in amu/charge:  $L$  is the particle path length in cm, and  $T$  is in units of ns ( $10^{-9}$  s). The acceleration potential

$U_A$  has a nominal value of  $-14.56$  kV but can be varied if necessary although doing so would affect calibration.

Mass resolution  $M/\Delta M$  is determined primarily by the time resolution of the LEF optics. Because the LEF portion of the IMS is time focusing resolution can be quite high ( $\sim 60$  at  $M/Q = 20$ ) including all effects of energy and angle straggling. LEF spectra are used in the interpretation of ST spectra. There, resolution is degraded by path length variations, which are caused by the range of trajectory angles leaving the ESA, combined with angle energy straggling in the foil. Writing the uncertainties as  $\Delta T$ ,  $\Delta L$  and  $\Delta E$  the mass resolution is:

$$M/\Delta M = [(T/\Delta T)^2 + (L/\Delta L)^2 + (E/\Delta E)^2]^{1/2} \quad (2)$$

*Positively Charged Ions with  $E_0/Q_0 < \sim 15.5$  kV.* An ion leaving the carbon foil and satisfying the condition  $\sigma(E_0 + Q_0 U_A) \cos^2 \theta < 14.56$  keV, where  $\theta = 14^\circ$  is the angle between the foil normal and the central IMS axis of symmetry, will execute simple harmonic motion before striking the LEF detector (see Figure 20). The motion of ions in the LEF is analogous to simple harmonic motion, depending only on ion  $M/Q$  and independent of energy or angle of entry into the field to first order:

$$T = \pi(M/Qk_2)^{1/2} \quad (3)$$

The effective “spring constant”  $k_2$  has been determined from calibration to be  $2.327 \times 10^6$  amu/(C s<sup>2</sup>). Positively charged daughter fragments from molecular breakup have energies per charge proportional to their fraction of the parent molecule’s mass. The LEF mirror field has been purposely “detuned” slightly from strict linearity to take advantage of this fact and optimize IMS resolution for molecular fragments. The square root relation in (3) holds very well despite detuning (see below). Other departures from the ideal field such as inhomogenieties cause ions to take different paths in the field, introducing broadening into mass peaks (Equation 2).

*Positively Charged Ions with Internal Energy per Charge  $E_0/Q > \sim 15.5$  kV.* Ions in this energy range are retarded by the linear electric field, but eventually reach the “straight-through” (ST) detector located at the far end of the LEF, opposite the foils. Their TOF is given by:

$$T = (M/k_2Q)^{1/2} \sin^{-1} \{ [L(k_2/2)^{1/2}] / [E/Q]^{1/2} \} \quad (4)$$

*Negatively Charged Ions.* These see a spatially varying field as they travel through the TOF region. Hence their flight times must be determined by integrating their velocity over the path.

$$T = (M/2k_2Q)^{1/2} \ln \{ [k_2^{1/2}L + (k_2L^2 + E/Q)^{1/2}] / (E/Q)^{1/2} \} \quad (5)$$

*Neutral Particles.* Most particles leaving the foils are charge neutral. Their TOF is given simply by their path length and velocity.

$$T = k_1L[M/E]^{1/2} \quad (6)$$

*Sensitivity.* In addition to identification of ion species, the other most important quantity of physical interest is the three-dimensional velocity distribution function for a particular ion species at infinity,  $f_i(\mathbf{v})$ . The quantity that IMS measures during a sampling interval  $\Delta t$  is the counting rate  $C$ . Assuming that the part of the distribution function measured at any one time is constant and uniform within the IMS range of acceptance, then, following the work of Johnstone *et al.* (1987) and others,

$$f_i(\mathbf{v}) = \mathbf{n} C M_i^2 / 4 E^2 G_i \Delta t \quad (7)$$

where  $\mathbf{n}$  is a unit vector indicating the direction of  $\mathbf{v}$ , and  $G$  is the differential IMS “geometric” factor:

$$G_i = A \varepsilon_i \tau_i \langle \Delta \Omega \Delta E / E \rangle \quad (8)$$

where  $A$  is the entrance aperture area,  $\varepsilon_i(E, M)$  is the energy and mass dependent efficiency of carbon foils and detectors as well as the effects of and circuit deadtimes,  $\tau_i(E, M)$  is the transmission dependence of foils, grids and optics, and  $\langle \Delta \Omega \Delta E / E \rangle$  is the solid angle and energy acceptance averaged over the entrance aperture.  $G$  has units of  $\text{cm}^2 \text{sr eV/eV}$ . The efficiency factor in (8) can be thought of as converting counts/s into ions/s.

Similar equations also apply to the ELS and IBS. Although ELS will observe only electrons, IBS is capable of observing and separating several ion species in a cold, flowing plasma as will occur during low-altitude Titan flybys. In that case its mass-dependent efficiency will have to be taken into account to obtain the correct relative abundance of ion species.

### 6.3. INSTRUMENT DESCRIPTION

Unlike ELS and IBS, which contain their own power supplies and data acquisition electronics, the IMS consists of a separate sensor unit and six separate electronics modules: a fast front-end electronics (FEE) performing signal acquisition, a time-to-digital converter (TDC), a spectrum analyzer module (SAM), a dedicated central processing unit (CPU2), and two high-voltage units (HVU1 and HVU2). The FEE is located in the sensor itself (Figure 18), the TDC, SAM and CPU2 are inside the DPU, and the HVU’s are outside near the sensor (Figure 3). Table VIII summarizes key IMS optical parameters.

Ions entering the IMS collimator are subject to an electric field set by a negative voltage on the inner electrode of the ESA. The value of this voltage is given by  $V_{\text{ESA}} = K E_0$  where  $K \approx R_0 / 2 \Delta R \approx 6.25$  for IMS,  $R_0$  is the mean major radius of the ESA, and  $\Delta R$  is the electrode spacing. The ESA high voltage (HV) supply is relatively complex. It generates stepped voltages at a 62.5 ms cadence, covering 63 voltage steps plus one “flyback” step every 4 s. The broad range of energies covered by IMS ( $E_{\text{MAX}}/E_{\text{MIN}} = V_{\text{MAX}}/V_{\text{MIN}} = 5 \times 10^4$ ) requires three separate

TABLE VIII  
IMS key sensor properties.

Analyzer	Parameter	Value/type
Electrostatic analyzer	–	Toroidal top-hat
	Mean major radius	6.50 cm
	Mean minor radius	1.30 cm
	Plate spacing	0.40 cm
	Analyzer constant	6.25
	Analyzer bending angle	93.0°
	Top-hat set-back angle	11.0°
	Top-hat aperture radius	2.29 cm
Mass spectrometer	<b>LEF</b>	Isochronous time-of-flight
	Spring constant	$2.327 \times 10^6$ amu/(Cs <sup>2</sup> )
	Detector	Z-stack Galileo MCP
	MCP outer radius	4.33 cm
	MCP thickness	0.10 cm
	Channel length/diameter	40:1
	STOP anode radius	3.75 cm
	<b>ST</b>	Linear time-of-flight
	Slant path length foil to detector	18.8 cm
	Detector	Z-stack Galileo MCP
	MCP outer radius	4.33 cm
	MCP thickness	0.10 cm
	Channel length/diameter	40:1
	START anode annulus radii	2.10, 3.80 cm
	STOP anode radius	2.00 cm

digital to analog converters that together yield  $3 \times 2^{12}$  “micro” steps. Normally a logarithmic voltage scan based on 63 log-spaced “macro” steps chosen from among the micro-steps is stored in tables used to command the ESA voltage. In principle the voltage table can be set to scan the ESA in a wide range of patterns. The other HVU2 supplies service the IMS microchannel plate (MCP) detectors, whose gains can be changed independently.

After leaving the ESA, ions encounter a guard electrode set at a distance of 5 mm from the ESA exit plane. The guard electrode is biased at approximately one-half the voltage on the inner ESA toroid to help shield the smaller ESA field (as low as a few mV/m) from the TOF acceleration field ( $\sim 1$  kV/mm). From the vicinity of the guard electrode ions are accelerated by  $-14.56$  kV through  $1.1 \pm 0.1$   $\mu\text{g}/\text{cm}^2$  thick “carbon” foils and into the LEF analyzer. The linear electric field is produced by voltages of  $-14.56$  kV applied to the foil end of the LEF and  $+14.56$  kV to the opposite (ST) end (Figures 18 and 20). Independent positive and negative high-voltage converters located in the HVU1 supply these voltages. Each supply is

controlled by an 8-bit command word. A  $10^{10} \Omega$  resistor-divider network applied to 30 co-axial rings creates a series of potentials that generate the LEF. One guard ring near the center of the ring stack is grounded to create a zero potential surface (Figure 20). In addition to its vertical, linear component, radial fields arise as a natural consequence of the solution to Laplace's equation in cylindrical coordinates. These act to push positive ions outward from the central axis and focus electrons toward it. By choosing an ESA bending angle of  $14^\circ$ , the inward radial velocity associated with ion bounce motion is balanced against acceleration caused by outward radial field components, thus optimizing ion transmission.

Because the carbon foils covering the entrance to the TOF are very thin and relatively large ( $7 \text{ mm} \times 18 \text{ mm}$  at the center line), they are mounted on stretched 333 lines-per-inch, 70% transmissive nickel mesh. As ions pass through the foils they come into an equilibrium charge state that depends on the incident species, its speed, and the foil material (Funsten *et al.*, 1993a, b, 1994, 1995), but is fundamentally independent of the incident charge state. To illustrate this, the probabilities of hydrogen, helium, carbon, and oxygen ions exiting a foil as singly charged positive or negative ions are shown as a function of energy in Figure 21. Above 15 keV (the lowest energy ions seen in the TOF) the ratio of neutral to positive to negatively charged hydrogen is  $\sim 35:15:1$  changing to  $\sim 60:40:1$  at 30 keV. The same ratios for carbon, on the other hand, are  $\sim 11:2:1$  and  $\sim 9:2:1$ , respectively, which indicates a higher proportion of negative ions relative to hydrogen (typically  $\sim 5:1$ ) and corresponding lower proportions of positive ions. For oxygen the comparable ratios are  $\sim 15:1:4$  and  $\sim 7:1:2$ , respectively, indicating the preponderance of negatively charged oxygen caused by its large electron affinity. It is interesting that for all three species the fraction of ions exiting as neutrals remains at  $\sim 70\%$  regardless of energy over this range. Helium has a positive ion yield that is quantitatively similar to oxygen's but the exit charge fraction of its metastable negative ion is  $< 3 \times 10^{-4}$  (Funsten *et al.*, 2001). Other ions have different positive, negative, and neutral yields, which generally fall within the range between that of hydrogen and helium. Typically, the fraction of ions exiting the foil in charge state  $Q = +2$  is less than 2%. Molecules incident on the foil are fragmented and, depending on the same parameters as for atoms, may exit the foil in a variety of daughter products and charge-states (Funsten *et al.*, 1994).

As ions exit a foil, they eject secondary electrons with a yield of two to three per incident ion on average (Ritzau and Baragiola, 1998). Secondaries are steered by nearby electrodes as they accelerate toward the outer annulus of the ST MCP. Electron transit times are  $\sim 1 \text{ ns}$  with negligible spread in times of arrival. An electron striking the ST MCP generates a signal on one of eight annular anodes located at the exit of the MCP (anodes and foils are aligned in elevation). The MCP signal is amplified and split into two components in the FEE. One identifies the elevation position of an event, the other starts the TOF measurement. In the nominal case of a single atomic species, a daughter product strikes either the central "stop" region of the ST MCP or the LEF MCP.

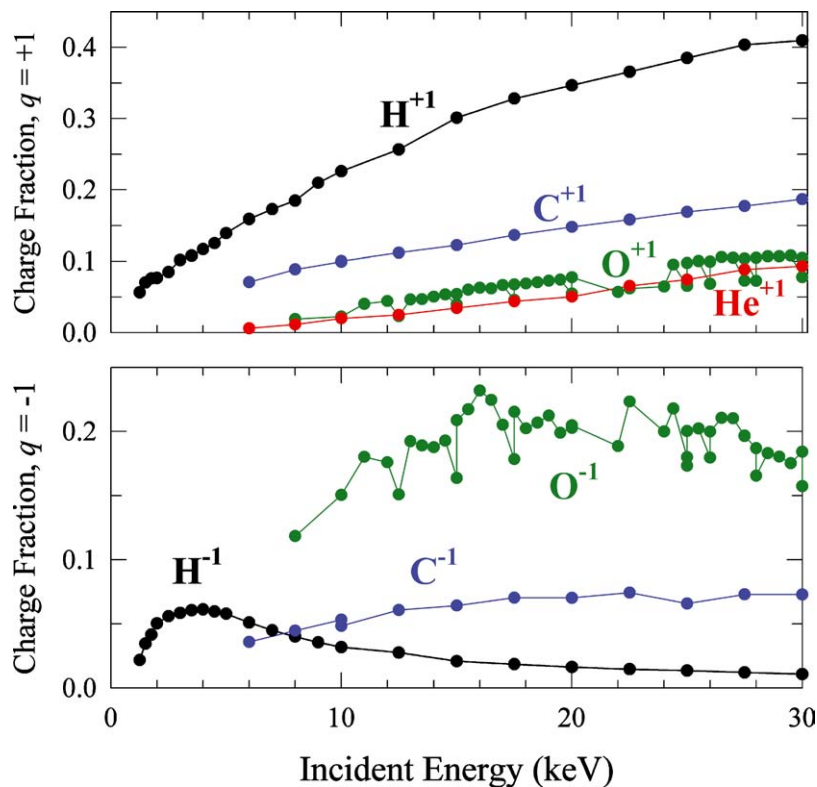


Figure 21. Equilibrium exit charge state fractions for charge states  $Q = +1$  (upper panel) and  $Q = -1$  (lower panel) for H, He, C, and O incident on a nominal  $0.5 \mu\text{g cm}^{-2}$  carbon foil as a function of incident energy. Data are taken from Funsten, *et al.* (1993a, b, 1994, and 1995).

The ST MCP consists of a so-called Z-stack of three individual plates mounted in proximity to each other. A typical operating gain is  $\sim 1$  to  $3 \times 10^6$  although this is an adjustable parameter controlled by changing the MCP bias voltage. The LEF MCP has a different configuration from the ST detector. Instead of a three plates in proximity, the MCP plate facing into the ion beam is located on the top of the TOF ring stack (Figures 18 and 23d). The remaining two plates are mounted 12 mm away from the TOF stack near ground potential. This feature conveniently decouples the LEF MCP signal from negative high voltage. Electron charge clouds from an MCP are collected on one of the anodes and then amplified in the FEE. Nearly all daughter products leaving the foils (except for those scattered out of the LEF region) have the potential to be detected. Particles striking the ring electrodes can cause secondary electrons that are detected as background.

Either a LEF or a ST stop event halts the timing measurement. In order to be counted as a valid TOF event, the TDC logic requires that start and stop events both be valid as well as coincident. In the case that “molecular” settings are chosen in

the TDC logic, a valid start and a least one stop must be coincident. The timing and outcome of all events are of course probabilistic, which must be taken into account during analysis.

In addition to detecting monatomic species, the IMS design also has fundamental advantages for measuring molecular ions. As noted earlier, nearly all polyatomic species break up during passage through foils (Funsten *et al.*, 1994). Molecular fragments exit with approximately the same center-of-mass velocity as the incident ion so their kinetic energy is proportional to their mass fraction. In order to take advantage of this fact, the part of the LEF field near the TOF foils (where low-energy daughter fragments are reflected) was “de-tuned” from the exact LEF solution by strengthening it slightly (effectively increasing the local spring constant). The effect on positively charged fragments (such as  $H^+$  from protonated molecules) is to make them return slightly faster than their counterparts entering as  $H^+$  parent ions. Trial and error determined the initial field estimate, after which Monte Carlo simulations were employed to find a solution with as few overlapping peaks as possible between atoms and molecules of interest. Details of this process are found in Nordholt *et al.* (1998).

Either the LEF or ST MCP or both may detect molecular fragments. The TDC identifies the later correlated event with high probability as a molecular event. This information, along with LEF and ST times-of-flight, are passed to the spectrum analyzer module (SAM) where a look-up table is used to identify the molecule. Triatomic and larger polyatomic molecules may produce more than two stop signals, but only two are processed. However, detailed TOF spectra can be examined on the ground to identify these ions. As an example of IMS capabilities, the TOF system can separate N, C, and O molecular fragments from  $N_2^+$  and  $CO^+$ , giving it an effective mass resolution of 1 part in  $\sim 2500$  (Figure 33 below).

TOF spectra obtained from the LEF have several properties worth noting. The first is that, because ions with  $E_0 < 15.5$  keV are time-focused regardless of energy, TOF spectra change very little with energy, making spectral deconvolution relatively easy (see Figure 34 below). The second property is that ST spectra are dispersed in TOF, which is both an advantage and disadvantage in the deconvolution process. It is an advantage because the electric field disperses, and therefore helps distinguish, negative from neutral from positive daughter products (listed in order of increasing TOF). It is a disadvantage because the lack of time-focusing means that peaks are broader (lower resolution), and there are many more chances for peak overlap.

#### 6.4. MECHANICAL DESIGN

The IMS collimator is located at the top of the unit (Figure 22). Seven equally spaced vanes divide the  $160^\circ$  FOV into eight elevation channels each  $20^\circ$  wide. The remaining vanes are closed to particles but are needed to support mechanical loads created by the ELS. All entrance collimation is coated with copper sulfide black to

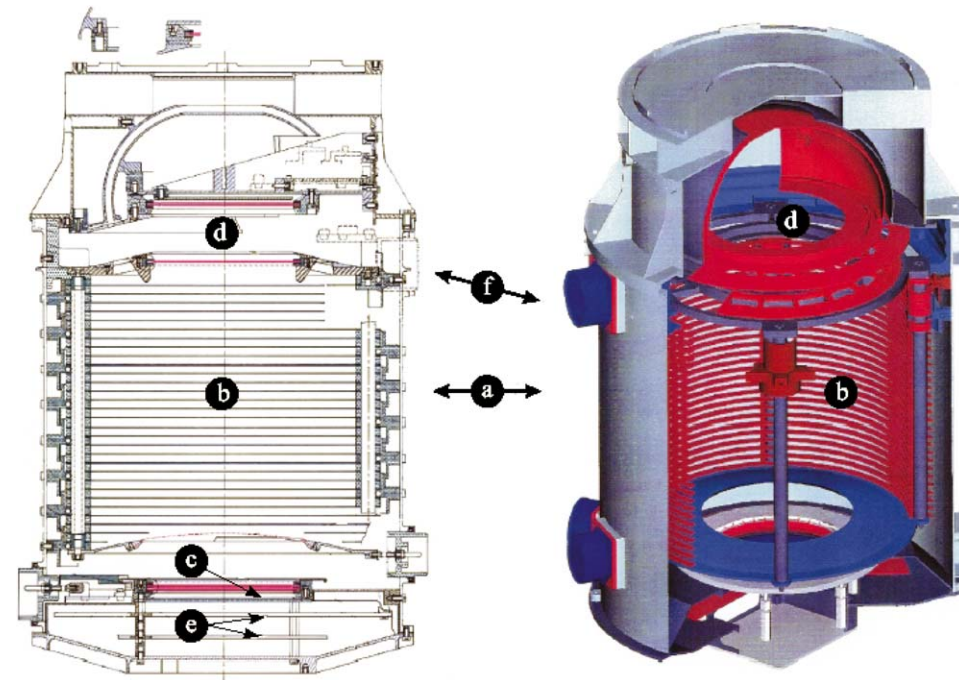
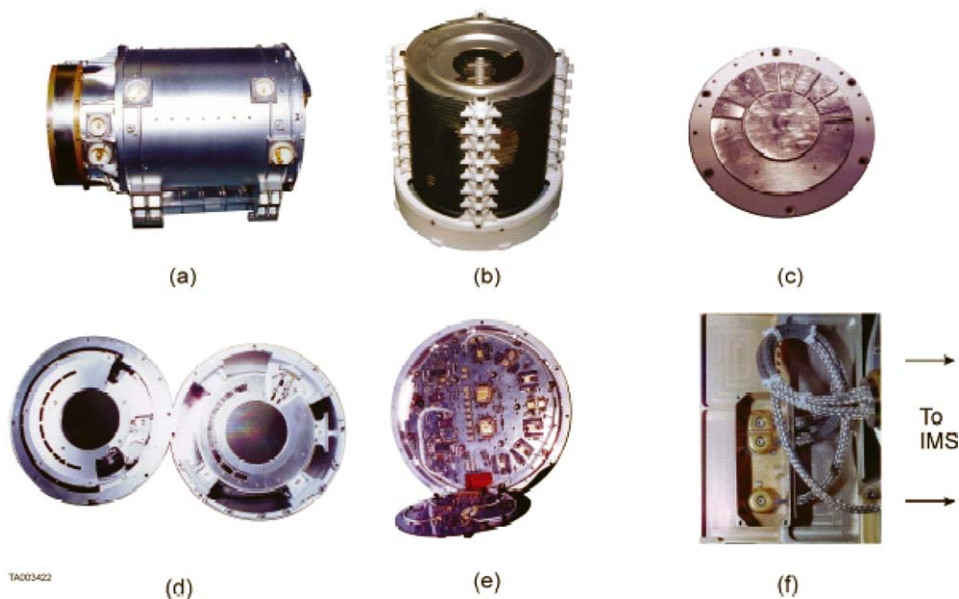


Figure 22. Elevation view of the IMS sensor shown as a detailed engineering drawing at left and as a cutaway perspective drawing at right. The letters a, b, c, etc. in the drawing refer to details visible in Figure 21.

suppress UV and particle scattering. During ground handling and through launch, the IMS aperture was covered by a thin sheet of metallized Kapton designed to help maintain chemical cleanliness and protect the many fragile sensor components (carbon foils, MCP detectors, and blackened optical surfaces) from mechanical damage. Once in space, the IMS cover was released and retracted by a mechanism similar to a roll-up window shade.

The inner dome of the toroidal analyzer is mounted concentrically with the outer by a cantilever located in the blind portion of the IMS FOV (just above (d) in Figure 22). The outer electrode is part of the IMS housing and is held at ground potential. ESA surfaces are also chemically blackened to suppress UV and particle reflections. All materials used inside the IMS are either polished aluminum or ceramic in order to maintain high levels of vacuum cleanliness and high-mechanical precision.

Figure 23b shows the LEF 30-ring assembly. Four ceramic spacers separate each ring from the next by 5.0 mm. One spacer on each ring is designed to hold one of the 30-resistor divider network used to generate the potentials for the LEF. Prior to assembly, electrical contact with the rings is made through gold-plated copper



*Figure 23.* Details of the IMS assembly keyed to Figure 20: (a) IMS housing showing aperture at left and ceramic high-voltage connectors (small white cylinders on the main body). (b) Assembled stack of 30 high-voltage rings used to generate the LEF. Four stacks of ceramic “vertebrae” that position the field rings and hold the resistor divider chain are visible. (c) ST MCP anodes showing eight individual start anodes at the top and the single ST STOP anode in the center. (d) A view looking along the central optical axis of the LEF into the opened IMS. The eight ESA field correction slits can be seen on the left in a semicircular arrangement. The corresponding foils are seen on the right. The dark areas in the center of both pieces are the upper and lower microchannel plates that make up the LEF MCP stack. (e) View of the FEE electronics. The output from the LEF MCP is sent via cabling external to the IMS housing to the FEE board. (f) View looking down on the HVU1 at terminals that connect to cables going to the  $-15$  kV (top) and  $+15$  kV electrodes on the TOF unit.

foils soldered to the ends of each resistor. Four long metal rods pass through holes in the ceramic spacers between the rings, holding the entire stack in compression. To provide the required stiffness of the ring stack, each spacer is attached to the outer IMS housing cylinder (Figures 22a and 23a). All six HV cables are terminated by ceramic feed-throughs that are protected by mechanical covers designed to allow the volumes around the terminals to outgas freely (Figure 23f). Protection from system noise required mounting the sensitive ( $\sim$ few mV signals) FEE inside the IMS housing.

The entrance to the LEF region can be seen most easily to the left in Figure 22d. The eight rectangular windows seen in this view are frames that carry the carbon foils. In the center of the assembly is the LEF MCP. Large openings between the foil assembly and the edge of the ceramic mounting ring provide ample gas conductance

during launch and afterwards. The IMS cylindrical housing is approximately 22 cm in diameter  $\times$  34 cm long.

## 6.5. ELECTRICAL DESIGN

A number of key science and resource requirements drove the electrical design of IMS.

1. Resolve TOF spectra to 0.75 ns over a range set by the fastest ions ( $H^+$  at 65 keV internal energy) and the slowest (heavy ions at 15 kV internal energies). For the ST portion of the instrument the central path length is 18.8 cm, giving a  $H^+$  flight time of 53 ns. Using 1600 ns as the upper limit on TOF we find that even with an energy loss of, say, 90% in the foils and an energy straggling tail of 300%, a limiting observable mass of  $\sim 400$  is achievable. For the LEF portion we can use Equation (3) to find the limiting observable mass to be  $\sim 200$  amu, although in practice it is doubtful that masses much above a few hundred amu will make it through the foil.
2. Compress the raw IMS data stream from  $(2048 \text{ TOF} \times 2 \text{ (LEF and or ST)} \times 8 \text{ elevation anodes} \times 16 \text{ bits})/0.0625 \text{ s} = 8.4 \text{ Mbits/s}$  to a more manageable  $\sim 10$  kbits/s. As discussed below, this problem is solved using on-board deconvolution of TOF spectra.
3. Obtain mass-resolved energy spectra continuously over 1 to 50,000 eV in 4.0 s, requiring a high voltage slew rate of 150 kV/s.
4. Generate  $\pm \sim 15$  kV high voltages for the TOF optics.
5. Keep mass, power and complexity to a minimum.

In the following section we describe the IMS electronics subsystems by tracing the order in which signals are acquired and processed, namely FEE to TDC to SAM, and then to CPU2.

### 6.5.1. Front-End Electronics

Once charge from an MCP detector is collected on an anode, it enters a series of amplifiers, discriminators, and logic that identifies the event (see Figure 24) and begins processing. In this discussion the signals are identified as “START” and “STOP.” Both event types are handled in essentially identical ways. When a START event is detected the signal is split into two parts. One is used to identify the location of the event in one of eight elevation angles or one of the two stop channels (LEF or ST). This part of the signal (termed the identification or ID signal) is processed through fast ( $0.2 \mu\text{s}$  deadtime) preamp and level-discriminators and can be used to correct for deadtime in the slower ( $2.2 \mu\text{s}$ ) circuits. The other “half” of the START signal is sent to the TDC where it triggers the timing circuitry. Similar processes apply to the STOP signals.

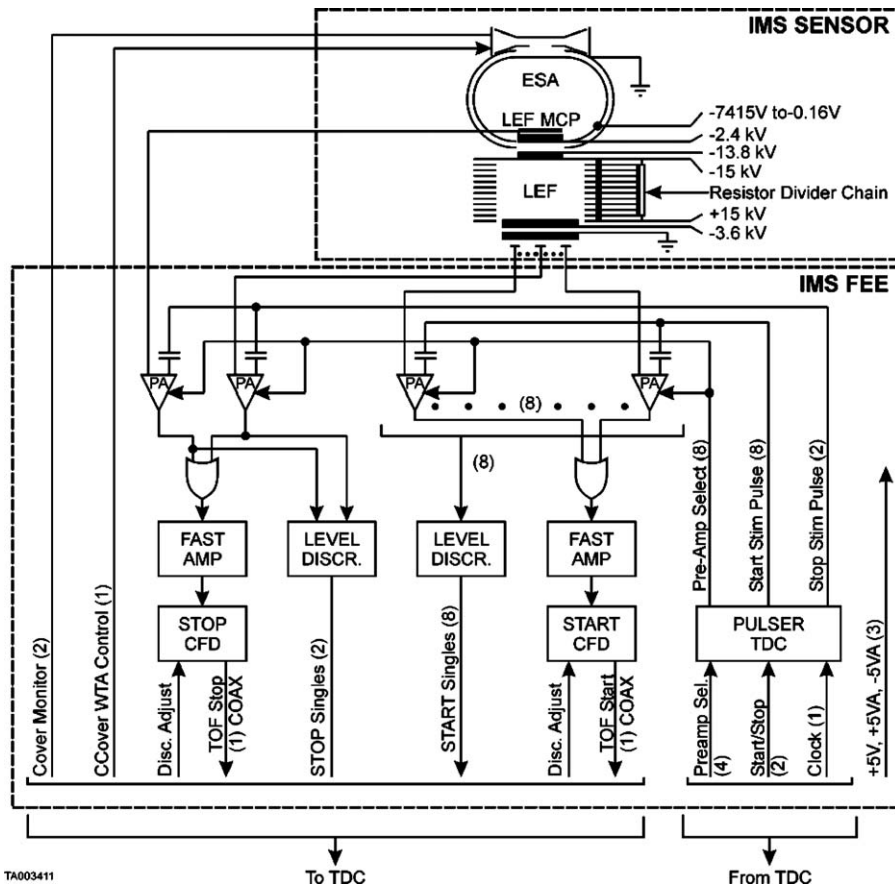


Figure 24. Schematic block diagram of the IMS front end electronics (FEE) and high-voltage connections.

### 6.5.2. Time-to-Digital Converter

Once a START pulse triggers the TDC, the state of the ID discriminators is captured giving the identity of the event origin (Figure 25). Subsequent START events are ignored for timing purposes but are counted as ID events. Once initiated, the TDC converts time directly into a digital word using a clock and vernier technique in the following manner. A valid START enables a gated 80 MHz clock that increments a counter. A subsequent STOP that occurs later than 40 ns (the pulse pair resolution of the TDC) after the START event, inhibits that counter, thus providing a coarse time measurement with a resolution of 12.5 ns. If no STOP event is recorded the counter times out at 1600 ns, corresponding to the longest time required for the heaviest, lowest energy ions to cross the TOF optics as discussed above. To obtain finer time resolution, the phase of the clock relative to the clock edge is measured at the instant the STOP is received by means of the delay line vernier (Figure 25)

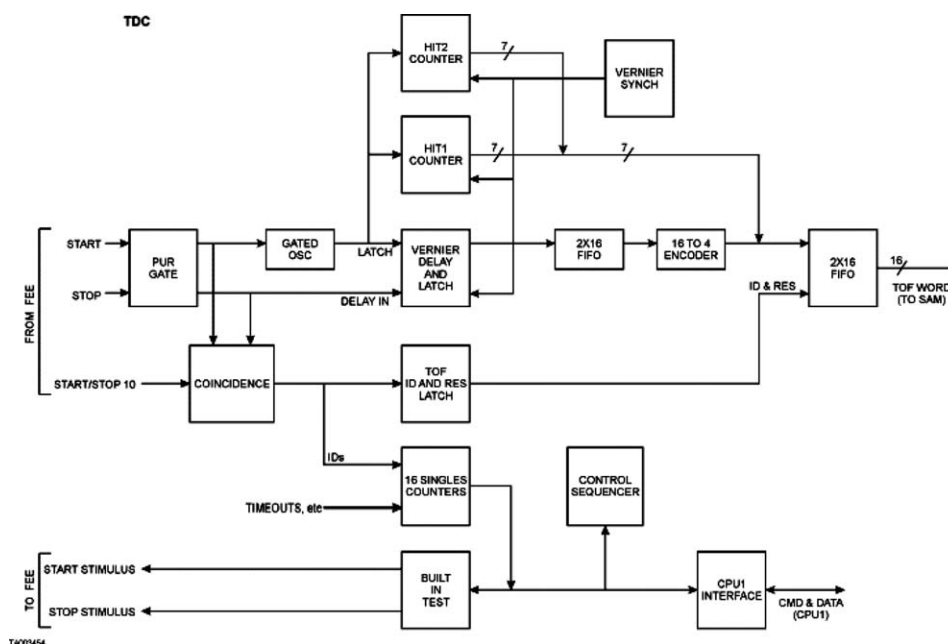


Figure 25. Schematic block diagram of the IMS time-to-digital converter (TDC).

implemented using a 12.5 ns delay line with 16 taps. As the STOP pulse propagates down the delay line, a changing pattern of 1's and 0's appears on the delay line taps. This pattern is latched at the end of every clock period. When a STOP occurs the resulting digital pattern represents the time of the STOP signal relative to the clock edge. The FEE logic then encodes it into a binary word that becomes the fine time measurement. Thus the TDC resolution is effectively  $12.5 \text{ ns}/16 = 0.781 \text{ ns}$ , corresponding to  $1600 \text{ ns}/0.781 \text{ ns} = 2048$  channels. If the TDC is instructed to identify molecular events then the gated clock is fed to two independent counters. The first STOP causes one counter to be inhibited and the vernier pattern to be read out and stored. The second STOP inhibits the second counter and causes a second vernier pattern to be read out.

There are several possible outcomes of events detected by the TDC logic in addition to the ideal outcome. For example, a "real" ion can cause a start event followed by a second ion causing a stop event. This could come about in two ways, each leading to a false result: (1) the start event could be a real start followed by a stop caused by the "wrong" ion, or (2) the start event could be caused by an ion scattered to the start electrodes (see Figure 20) followed by a stop caused by a second ion. Another example of types of false coincidences is that between real start or stop events and background in the detectors, e.g., that caused by penetrating radiation. The rate of accidental coincidence events is dependent in a complicated non-linear

way on the total event rates. False events and background must be removed from IMS data before they are usable.

After a TOF measurement is completed, the TDC encodes an 11-bit TOF value, a 3-bit elevation sector value, a resolution bit signaling ST or LEF data, and a “continuation” bit indicating a molecular event. Each 16-bit TOF word is then sent to a first-in-first-out (FIFO) buffer read out by the spectrum analyzer module (see Figure 25). The TDC is then reset in preparation for the next measurement. Among its other functions the TDC logic checks for inconsistent control states, channel ID’s, or time measurements in order to minimize systematic errors.

During a single IMS sampling period (62.5 ms) the TDC also accumulates the number of ID events corresponding to the eight start anodes, two stop anodes, two timing discriminator channels, number of times when no coincident stop TOF event was detected, total number of TOF measurements completed, and the number of events recorded in two other configurable channels. The configurable channels are used to diagnose TDC operation and to correct errors that may occur at high-counting rates. They can be set to read out the total number of the following events recorded during a 62.5 ms measurement period: (1) STARTs, (2) STOPs, (3) acquisition errors, (4) TDC fixed deadtime reached (regardless of whether or not a measurement results in a valid TOF measurement), (5) monatomic events, (6) molecular events, (7) TDC resets at the end of a measurement cycle, (8) errors caused by indeterminate channel ID values, and (9) TOF measurements less than the pulse-pair resolution time of 40 ns.

To achieve the best possible performance at high-event rates, the TDC operates as a non-paralyzable counter with a fixed deadtime of  $2.187 \mu\text{s}$  for TOF measurements. ID measurements (collected in “SINGLES” counters), on the other hand, have a  $0.2 \mu\text{s}$  deadtime making them suitable for correcting the slower timing measurement rates. Finally, the FEE/TDC system has built-in test pulsers that can stimulate any START or STOP pair with one of 24 selectable time delays at periodic event rates up to 1 MHz.

### 6.5.3. *Spectrum Analyzer Module*

The SAM processing method allows a high level of TOF data compression ( $\sim 1000:1$ ) to be achieved with little sacrifice in accuracy. The key to carrying out this process at high-event rates and within the short IMS sampling interval (62.5 ms) is a high-speed, deterministic deconvolution technique that we will refer to as the SAM algorithm. The hardware that supports this algorithm has a distributed, pipelined architecture based on four loosely coupled, reconfigurable modules (Figure 26). Once SAM processes a single data sample (i.e., data gathered in 62.5 ms) they are transferred to the CPU2 processor and the cycle repeated. Although data transfers from FEE to TDC and TDC to SAM occur at random rates, control of all other processing, data transfers and command and control functions are synchronized, taking place during the final 12.5% (7.81 ms) of the sampling interval.

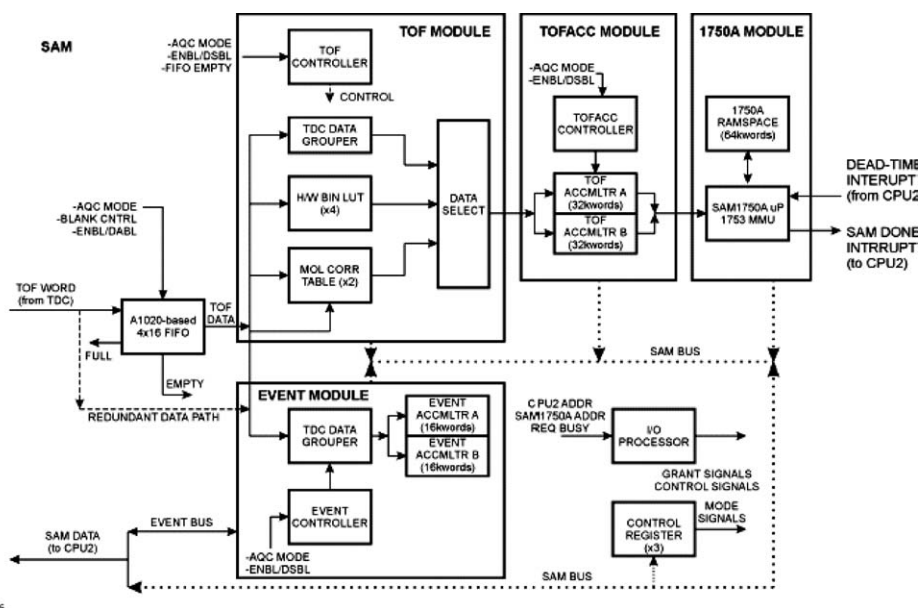


Figure 26. Schematic block diagram of the Spectrum Analyzer Module (SAM).

During this time the ESA voltage is stepped, data registers are read out and reset, and new commands are executed if required.

As a consequence of the primary measurement objectives discussed in Section 6.1.1, two different types of data and two differently timed acquisition cycles form the basis of IMS operation. The data types consist of ion data (ION) identified on-board at the highest possible rate using the SAM algorithm. The second is TOF spectra at the highest possible mass resolution but at a much lower data rate. ION energy spectra have a time resolution of 4.0 s for a maximum of 7 ion species over the full energy range. TOF data on the other hand, also cover the energy spectrum but at lower time resolution (256 s).

The operational cycles associated with data acquisition are defined as A- and B-cycles. The A-cycle lasts 32.0 s. During this time the ESA is scanned through eight, 64-step energy sweeps of 4.0 s each. The slower B-cycle is timed to correspond to eight A-cycles and to the acquisition and transmission primarily of TOF spectra (during both A- and B-cycles, data of both types are being collected). Dual memory banks allow raw data acquisition to proceed while CPU2 and SAM processors both access data from the previous 4.0 s acquisition interval. At the end of each interval, spectra that were processed during the previous interval are read from SAM by CPU2. In addition, new, selectively binned TOF spectra, are read into the SAM processor. There, during the next measurement interval, the SAM algorithm deconvolves TOF spectra, extracting selected ion  $M/Q$  values. Once analysis is

TABLE IX  
SAM operational modes.

Mode	Description
1. SNGL_DUAL_STOP	Single-stop or dual stop mode of operation
2. TOF_MODE	
Angle_Collapse_En	Accumulate TOF, collapse Polar Angle
Alt_Angle_Collapse	Accumulate TOF, collapse Alternate Polar Angles
Seq_Event_En	Enable Sequential Event Mode
3. BINNING MODE	
HW_Bin_En	Enable Hardware Binning Mode
SW_Bin_En	Enable Software Binning Mode
4. HW Bin LUT Sel	Select 1 of 4 hardware binning look-up tables
5. Mol LUT Sel	Select 1 of 2 molecular look-up tables
6. ACCUM_EV1_2.EN	Accumulate 1 event or both events from a dual stop event
7. TOF_CMPRS	Enable or disable summing: 4 adjacent TOF ST bins; 2 adjacent LEF bins
8. TOF_DISABLE	Enable or disable TOF and TOFACC Modules

complete, SAM interrupts CPU2, which then reads the  $M/Q$ -sorted data. SAM is then ready for the next acquisition and processing cycle.

SAM operates as a CPU2 slave. The analysis algorithm is coded in the Ada language and executed in the 1750A microprocessor module (Figure 26). Its address space is accessible by CPU2, and program and local data are loaded into the module by CPU2. However, SAM itself cannot read or write to CPU2 memory. The three remaining modules (TOF, TOFACC, and EVENT) are each autonomously controlled by separate gate arrays. In order to speed up TOF data processing, dedicated paths support concurrent data flow from the input FIFO to the appropriate processing modules (Figure 24). In addition, each module manages its own local processing and external access to data. The SAM operational modes are given in Table IX.

SAM acquires data from the TDC via a FIFO buffer at a maximum rate of  $5 \times 10^5$  periodic events/s. The FIFO can be configured by command to enable dual-stop operation (for molecules) and data acquisition from selected elevation ID channels. Disabling the FIFO causes data to be routed by a redundant path (Figure 26) to the EVENT and TOF modules.

The TOF module organizes incoming data from the TDC into groupings that correspond to different ion species. The way in which incoming data are grouped depends on parameters in the SAM ION group table, which contains a targeted list of species and their binning parameters (see Table IX). In normal operation, a software-binning mode (option 3 in Table IX) will be used. In this mode 16 TOF bins

$\times 8$  elevation sectors  $\times 2$  channels (ST and LEF) are stored during one 0.0625 s accumulation period. During the next acquisition period the SAM algorithm is executed beginning with the first new data stored in the double-buffered memory. If the hardware-binning mode is selected instead, the same quantity of data are selected but then are grouped according to one of four command-selectable look-up-tables (LUTs). In this mode, data are grouped in TOF channels according to their assigned mass peak locations and exported to CPU2 (Figure 26). In general, the software-binning mode requires more analysis time than the hardware-based approach.

Deconvolution of TOF spectra is more complicated in the dual STOP mode used for molecular ions. The reason is that a molecular event (i.e., two valid coincident stops) consists of two daughter products, both of which must be identified and then their identities correlated in order to specify the parent molecule. In this mode incoming TOF events are classified into one of four two-dimensional correlation tables depending on which of the following events occurs: (1) the ST MCP records the first stop, (2) the ST MCP records the second stop, (3) the LEF MCP records the first stop, or (4) the LEF MCP records the second stop. Each of the four tables is 2048 TOF channels deep and contains identification codes for 32 different molecular species. Once a molecular event is identified the SAM algorithm is used to identify the particular parent molecule.

After SAM algorithm processing is completed, all valid TOF events have been sorted into a two-dimensional array consisting of eight elevation sectors by seven ION (atomic or molecular) species. These 56 data products are sent to CPU1/CPU2 shared memory once per energy step. Several data compression modes are available based on summing adjacent energies or angles (Table IX), or by selecting fewer than seven ion species. Yet another mode, used primarily for engineering, stores 32,000 TDC words with each word corresponding to a concatenation of TOF (11-bits) + elevation (3-bits) + TOF resolution (1-bit) + atom/molecule (1-bit). Energy and azimuthal data for a particular set of events are tracked separately.

We would now like to provide some insight into the SAM algorithm (Sittler, 1993). The algorithm's advantages are that it reduces the inversion problem of deconvolving TOF spectra to a deterministic number of multiply and add operations, thus making processing time predictable and the algorithm efficient. Figure 27 contains two examples of TOF spectra. Summing counts within an interval centered on a given mass peak is a straightforward way of obtaining ion peaks from a LEF spectrum (top panel). The bottom panel, however, shows a simulated spectrum obtained from the ST detector in which it is apparent that TOF peaks from different parent species overlap significantly, and simple binning will not give the correct answer. The SAM algorithm responds to this need by providing accurate deconvolution of complex spectra without introducing systematic errors.

Taking advantage of the fact that TOF peak profiles for different species can be determined from calibration, we have developed a relatively simple algorithm that

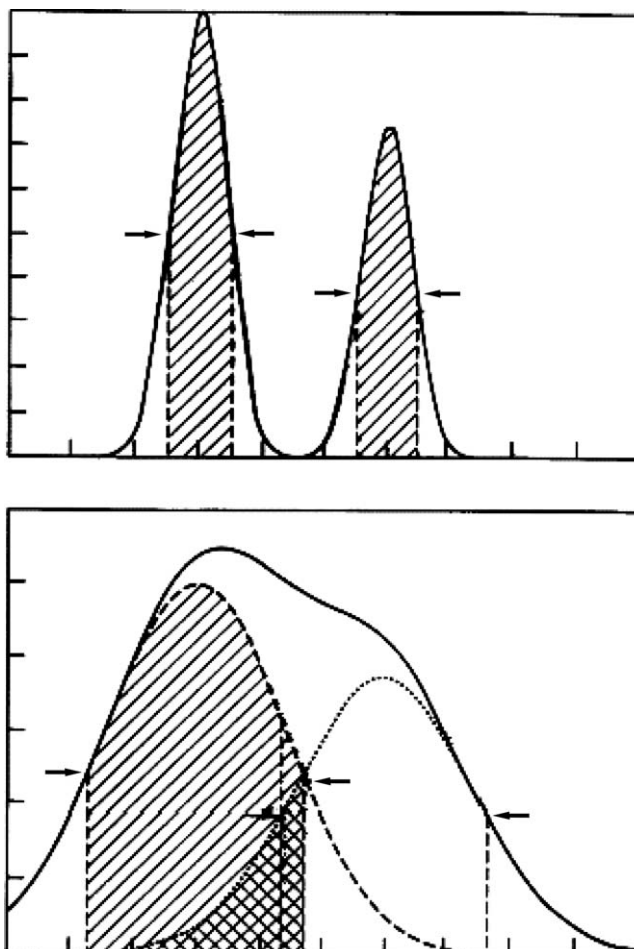


Figure 27. Schematic example of a high-resolution (LEF) TOF spectrum (upper panel) and a low-resolution (ST) TOF spectrum (lower panel).

can be expressed as a set of  $n$ -coupled linear equations with constant coefficients. This is shown in Equation 9.

$$\begin{aligned}
 N_1\alpha_1 \sum_{k=1}^m {}^1\gamma_1^k + N_2\alpha_2 \sum_{k=1}^m {}^1\gamma_2^k + \dots + N_n\alpha_n \sum_{k=1}^m {}^1\gamma_n^k &= B_1 \\
 N_1\alpha_1 \sum_{k=1}^m {}^2\gamma_1^k + N_2\alpha_2 \sum_{k=1}^m {}^2\gamma_2^k + \dots + N_n\alpha_n \sum_{k=1}^m {}^2\gamma_n^k &= B_2 \\
 N_1\alpha_1 \sum_{k=1}^m {}^n\gamma_1^k + N_2\alpha_2 \sum_{k=1}^m {}^n\gamma_2^k + \dots + N_n\alpha_n \sum_{k=1}^m {}^n\gamma_n^k &= B_3
 \end{aligned} \tag{9}$$

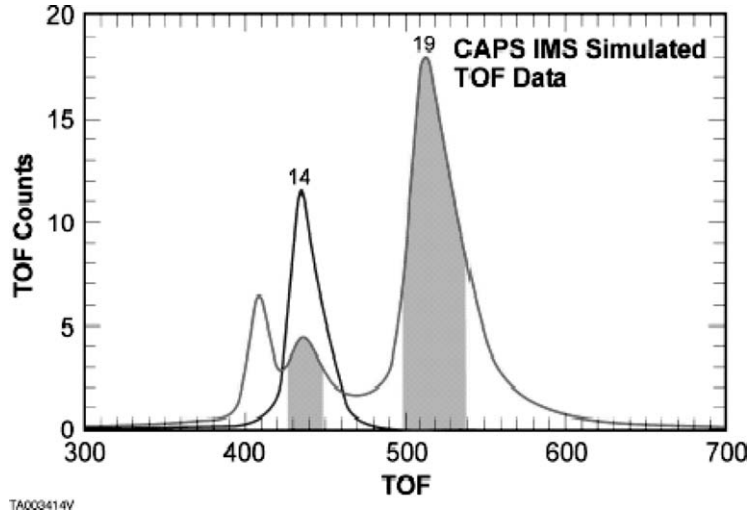


Figure 28. Simulated TOF spectrum resulting from mass 14 and the (fictitious) daughter fragments of mass 19 (in red).

Here the  $B_j$  are binned counts for the  $j$ th binning interval where  $j$  is the index indicating ion species. The  $N_j$  are the true counts corresponding to the  $j$ th ion species, the  $\alpha_j$  renormalize the  $N_j$  so that the product  $\alpha_j N_j$  is equal to the total number of TOF events due to ion species  $j$ , and  ${}^n \gamma_n^k$  gives the fraction of the total counts that the  $k$ th fragment of ion  $j$  contributes to the binning interval of ion  $i$ . Basically each row in Equation (9) consists of terms that represent contributions from each ion species and its daughter fragments to the binned counts for a particular binned interval. An application of this algorithm can be seen in Figure 28 where we show a simulated TOF spectrum containing only  $M/Q = 14$  and 19 (the mass 19 fragments are fictitious and for illustration purposes only). A binning interval is defined as the inclusive range of TOF channels between the FWHM points measured at a particular peak (roughly the blue areas in Figure 28). The binning interval for the largest peak is the shaded region on the right containing  $N_j$  counts. The total under all peaks attributable to mass 19 is  $\alpha_j N_j$ . The shaded region on the left is associated with a daughter peak of mass 19, showing the contribution of the  $k$ th fragment of ion  $j$  (i.e., of mass 19) to ion  $i$  (i.e., mass 14), i.e., the factor  ${}^n \gamma_n^k$ .

The set of equations in (9) can be written in matrix notation as follows:

$$\begin{bmatrix} a_{11} & a_{12} & a_{13} & \dots & a_{1n} \\ a_{13} & a_{22} & a_{23} & \dots & a_{2n} \\ \vdots & & & & \\ a_{n1} & a_{n2} & a_{n3} & \dots & a_{nn} \end{bmatrix} \begin{bmatrix} N_1 \\ N_2 \\ \vdots \\ N_n \end{bmatrix} = \begin{bmatrix} B_1 \\ B_2 \\ \vdots \\ B_n \end{bmatrix} \quad (10)$$

where the total coupling coefficient is given by  $a_{ij} = a_j \sum_{k=1}^m i \gamma_j^k$ . By taking the inverse of Equation (10), we obtain the following

$$\begin{bmatrix} N_1 \\ N_2 \\ \vdots \\ N_n \end{bmatrix} = \begin{bmatrix} g_{11} & g_{12} & g_{13} & \dots & g_{1n} \\ g_{21} & g_{22} & g_{23} & \dots & g_{2n} \\ \vdots & & & & \\ g_{n1} & g_{n2} & g_{n3} & \dots & g_{nn} \end{bmatrix} \begin{bmatrix} B_1 \\ B_2 \\ \vdots \\ B_n \end{bmatrix} \quad (11)$$

In Equation (11) the summed counts  $N_j$  are seen to be a weighted sum of the binned data  $B_j$  for which the  $g_{ij}$  are the weighting coefficients. (Note that  $C_j = \alpha_j N_j$  represents the total number of counts originating from ion  $j$ , which is what SAM provides to CPU2.) Because ST spectra change with ion energy (recall that ST TOF  $\sim 1/\text{velocity} \sim E^{-1/2}$ ), ST spectral binning intervals and inverse coupling coefficient matrices also change. The SAM ION group tables contain binning intervals and matrices for 16 energy steps covering the full energy range then operating. The values used for a given energy step are computed in SAM by linear interpolation at the end of the preceding energy step. Finally, SAM uses the total number of TOF events processed plus the total number of timeout events to make dead time corrections.

The major advantage of the SAM approach is that the majority of calculations needed to deconvolve ion species, such as peak fitting, can be performed on the ground using calibration data. Only the results, in the form of coefficients that make up the inverse matrix  $G$  and the binning intervals, are needed in flight. The SAM method works very well but depends on accurate calibration, inclusion of all observed species in the group tables, and subsequent analysis of contributors to calibration mass peaks.

*Algorithm Modeling.* Multiple simulations have been performed to test the SAM algorithm. Observed ion peak shapes of parent and daughter particles are modeled by combined gaussian and lorentzian fitting functions. Peaks from daughter species are normalized to unity under the total line profile (Figure 29). Then the sum of the counts in each peak is weighted such that the number of counts for a particular ion,  $j$ , are equal to  $C_j$ . The procedure is then repeated for all ions making up a particular group.

The data shown in Figure 29 represent simulated spectra from ions with masses 14 through 19. Although the six TOF spectra are simulated, it is fairly obvious that it would be impossible to interpret the summed spectrum (red spectrum labeled "14–19") without some means of deconvolving individual peaks shown below it. The process followed to generate coefficients needed by the SAM algorithm begins by defining a binning interval for each dominant ion peak (in this case the peaks labeled 14–19 in Figure 29). Once binning intervals are specified, it is straightforward to compute the inverse coupling coefficient matrix. Then a simulated spectrum can be generated and data binned and multiplied by the inverse coupling coefficient

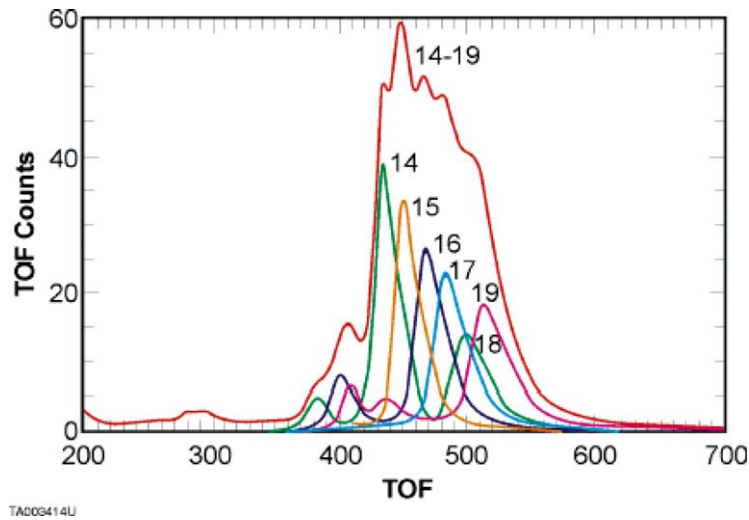


Figure 29. A simulated example of daughter product peaks ( $M/Q = 14$  through 19) and the sum of all daughter-product counting rates (outer envelope in red) based on calibration data. Note daughter fragments from several molecular species such as the water group are present (masses 16-19). Each species is normalized to 1000 counts.

matrix  $G$ . In order to estimate the accuracy of this method, poisson uncertainties are introduced randomly and the process repeated 200 times. In this particular example the water group ions (16–19 in Figure 29), are broader than mass 14 and 15 peaks because of greater overlap of the 16–19 peaks in this region ST mass resolution is relatively low ( $\sim 8$ ).

As an example of the power of the SAM technique, we have considered a case in which the relative distribution of total counts from each ion species in Figure 29 is held the same, but the total number of counts in the entire TOF spectrum is varied from 10 to 10,000 thus varying counting statistics and, one would think, the accuracy of the method. Figure 30 is a graph of the square root of the number of counts assigned to each peak divided by the measured standard deviation from the simulation. The profiles in Figure 30 are relatively flat and independent of count rate. As expected, the best precision is obtained for the most abundant species (14 and 15) with the least precision for masses 16–19. Note, however, that although the relative precision for the least abundant species is low, the average results are correct. The constant values for the errors result from the requirement that the relative abundances are held constant.

#### 6.5.4. High-Voltage System

Figure 31 is a schematic of the IMS high voltage (HV) system made up of five supplies controlled independently by CPU1 (see Table X for detailed supply characteristics). As explained earlier, the supplies are contained in two separate units: nominally  $\pm 15$  kV in HVU1 and the two MCP supplies and ESA stepping supply

TABLE X  
IMS high-voltage supply specifications.

Supply	Range (kV)	Resolution (bits)	Precision	Ripple (p-p)
HVU1/N	0 to +16.0/0 to -14.56*	8	$\pm 1\%$	0.1%
HVU1/P	0 to +16.0/0 to +14.56*	8	$\pm 1\%$	0.1%
HVU2/ST MCP	-0.5 to -3.6	8	$\pm 2\%$	0.5%
HVU2/LEF MCP	-0.5 to -2.4	8	$\pm 2\%$	0.5%
HVU2/ESA	-0.00015 to -7.415	3 ranges $\times$ 12	$\pm 0.5\%$ or 1 LSB	0.25%

\*First range is maximum capability. Second range is normal operating range.

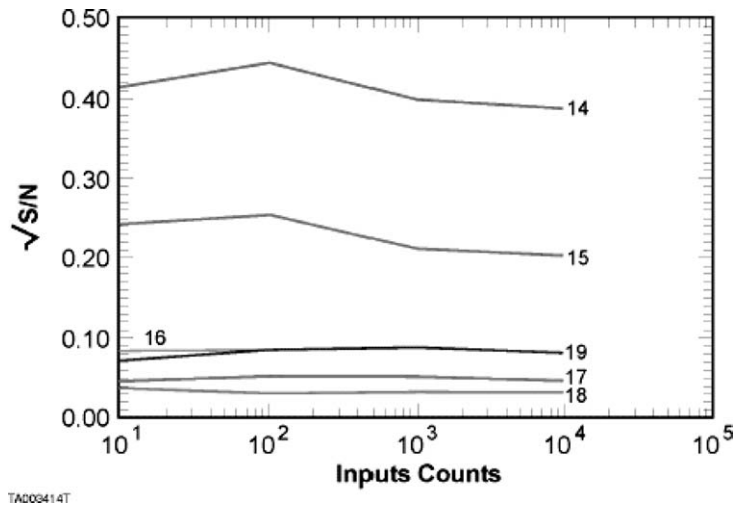


Figure 30. The ratio of the square root of the signal to measured standard deviation of estimates produced by the SAM algorithm as a function of the number of counts in the simulation. Data are from 200 runs of the algorithm using the data in Figure 29.

in HVU2. All supplies feature current-limiting and breakdown protection, as well as analog monitoring (digitized in the data stream). HVU1 is powered by filtered +30 V from spacecraft primary power whereas the HVU2 supplies use +15 V generated by CAPS. Stringent hardware, software and operational precautions were instituted to prevent HV from being applied at inappropriate times. Once in flight, separate commands have to be sent to enable and arm a supply. In addition, high-voltage commands (to any sensor) are checked by CPU1 to ensure they do not violate pre-set constraints on upper HV limits or HV step size. High-voltage cables rated at  $\geq 2.5$  times the respective supply voltages connect HVU1 and HVU2 to IMS sensor electrodes (40 kV cables are used for HVU1 connections). All HV connectors were custom designed and fabricated from low-void ceramic to prevent high-electric field concentrations that might lead to HV breakdown over the course

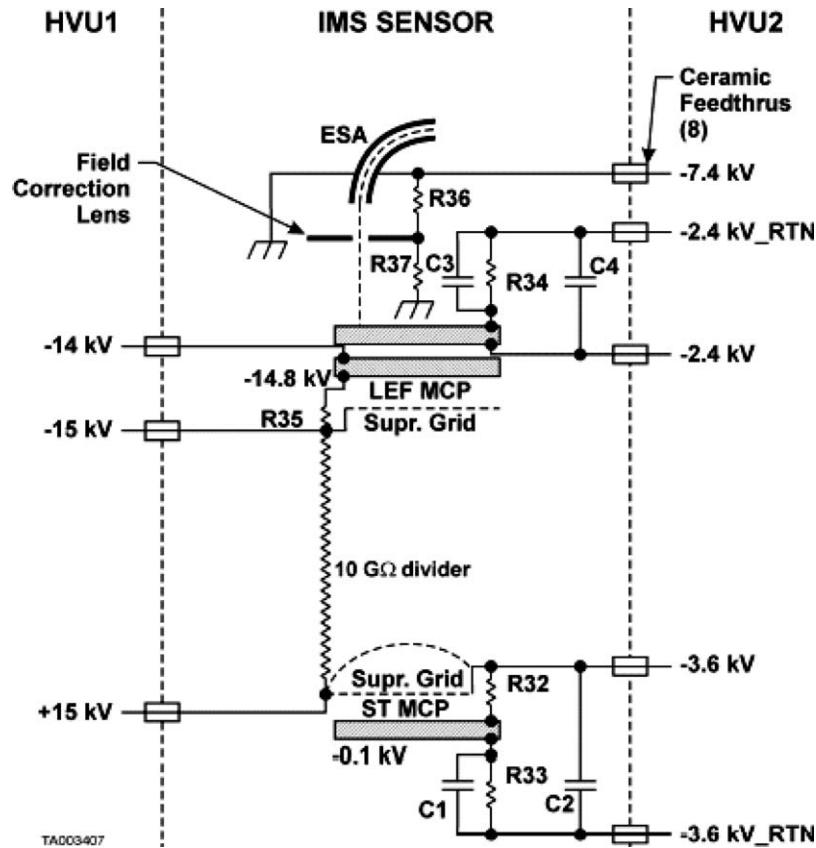


Figure 31. Schematic of the IMS high-voltage system.

of the mission. Metal covers placed over the HV terminals reduce electric stresses and provide mechanical as well as contamination protection.

*HVU1.* The HVU1 supply is composed of independent positive and negative voltage converters whose output is maintained at  $\pm 1\%$  over all line and temperature variations (Table X) with very low ripple. The primary purpose of HVU1 is to provide the negative and positive high voltages that together create the LEF by correctly biasing a string of 30-high ohmic resistors running the length of the TOF ring stack (Figures 24 and 31). HVU1 also generates regulated 1200 V referenced to  $-15$  kV that is used to bias the first plate in the LEF MCP stack. Because power for the LEF MCP regulator is derived from the  $-15$  kV supply the latter must reach a minimum of  $\approx -12$  kV in order for the LEF MCP to reach  $\sim 950$  V and operate correctly. A voltage drop of  $-100$  V is placed on a grid in front of the MCP to return secondary electrons to the MCP surface, thus maintaining high efficiency.

To make a compact but reliable unit, electric fields in the HVU1 supplies were kept below 1 kV/mm relative to the grounded housing. Transformer and high voltage assemblies were not encapsulated in order to avoid multi-material composite

structures that could introduce mechanical stresses that might in turn lead to dielectric faults and eventual breakdown. Instead, after fabrication and cleaning, the interior surfaces and components were coated with Parylene-C, a tough, low-outgassing polymer with high-dielectric strength.

*HVU2*. Both of the MCP supplies are located in the HVU2 as is the ESA supply. The MCP supplies are virtually identical in construction and operation, relying on a pulse-width modulator control circuit and a resonant converter operating at a switching frequency of 100 kHz. The capacitor networks shown in Figure 31 provide rf filtering. A resistor divider (R36 and R37 in Figure 31) biases the field-correcting aperture located at the ESA exit to approximately one-half the ESA plate potential. Another function of the MCP supplies, in addition to powering the two detectors, is supplying a suppression bias voltage to high-transmission grids to return secondary electrons to the MCP (the same function provided by HVU1 for the LEF MCP). Similar potentials at the back of the third stages of both detectors accelerate electron charge clouds toward their respective anodes.

The ESA programmable power supply presented several challenges that make it different from the MCP supplies. The primary requirements were that it step rapidly and accurately over a wide range of voltages set by the energy range of the instrument (0.16–7415 V, taking into account the finite width of the IMS passband). Thus a commandable resolution of 14 bits was required to obtain the precision given in Table X. With this resolution it is possible to cover a wide dynamic range very accurately with, in theory, any type of scan desired (linear, logarithmic, etc.). The supply is designed to step every 62.5 ms with a slew period of 12.5% or 7.81 s, requiring a voltage slew of 150 kV/s.

## 6.6. CALIBRATION

Returning to the equation for “geometric” factor, we can use Equation (8) to find a way to measure this factor in the laboratory. As discussed by Johnstone *et al.* (1987) and others, Equation (8) can be rewritten:

$$G_i = (Q/J_0)\varepsilon(E_j, M_i)\tau_i(E_j, M_i) \sum_i [\Delta\theta \sin\theta \Delta\varphi(\Delta E/2E)]_i C_i S_i \quad (12)$$

In this equation  $J_0$  is the beam current density its charge so that their ratio has units of flux. The efficiency and transmission are functions of energy and mass. The summation term is taken over a series of small volumes in energy space centered on  $(\theta, \varphi, E)_i$  weighted by the counting rate at each location. The summation extends over the entire acceptance of IMS. Finally, the weighting factor  $S_i$  accounts for variations in ion current over the time that the individual samples are taken.

Calibration was performed with a Von Ardenne plasma discharge source at SwRI and a radio frequency source at LANL (Alton, 1993). Beam intensity was fairly

stable over short time periods ( $\sim 1$  h) but could be controlled only by pressure feedback in the source itself. The beam used for calibration at SwRI was monochromatic and plane parallel to a high degree. It was verified to have an angular spread of  $0.2^\circ$ , about 2.5% of the width of IMS acceptance in angle. Beam width in energy was  $\Delta E/E = 0.005$ , about 3% of the IMS passband. Only the mass resolution of the beam separator was below expectations  $(M/\Delta M)_{\text{BEAM}} \approx 40$ .

During calibration a known ion species was selected, the energy of the beam set, and  $J_0$  measured. Because it is far simpler than varying the energy of the ion beam, the voltage on the ESA was micro-stepped at increments of  $\sim 0.3\%$  of the passband. The IMS was placed on a three-axis goniometer (two angles plus translation) and rotated about the center of the IMS FOV to obtain angular measurements at a resolution of  $\sim 1^\circ \times 2^\circ$  (AZ).

On the other hand, calibration of the IMS response to mass, energy, and  $J_0$  could be achieved relatively quickly. A wide range of energies was calibrated using  $\text{N}^+$  as a standard. Similarly, a wide range of ion species was calibrated using a few specific ESA energies as standards. At every opportunity the value of  $J_0$  was measured to quantify absolute calibration.

Correctly associating the center of TOF peaks with corresponding  $M/Q$  values for known gases established TOF calibration, the correction factor  $\sigma_i(E, M)$  for energy losses in the foil, and  $k_2$  in Equation 3.

The mass-analyzed ion beam at LANL was used initially to test IMS energy-angle response and TOF characteristics. From the latter, initial coefficients for the SAM algorithm could be calculated. During these tests we discovered cross-talk between elevation-angle channels caused by internal particle scattering. Coating the inner plate of the ESA with copper sulfide black, an anti-scattering agent, eliminated most cross-talk but some remains.

Final calibration of the IMS in flight configuration was carried out at SwRI. Only about 30% of planned activities were completed. Twenty energy steps between 0.256 and 27.56 keV, corresponding to the centers of the IMS energy passbands, were covered. The calibration species included  $\text{H}^+$ ,  $\text{He}^{2+}$ ,  $\text{He}^+$ ,  $\text{C}^+$ ,  $\text{CH}^+$ ,  $\text{N}^+$ ,  $\text{CH}_2^+$ ,  $\text{NH}^+$ ,  $\text{O}^+$ ,  $\text{CH}_4^+$ ,  $\text{NH}_2^+$ ,  $\text{OH}^+$ ,  $\text{H}_2\text{O}^+$ ,  $\text{H}_3\text{O}^+$ ,  $^{20}\text{Ne}^+$ ,  $^{22}\text{Ne}^+$ ,  $\text{N}_2^+$  and  $\text{Ar}^+$ . The primary concentration of calibration effort covering nearly all of these species at a single energy took place at 1.024, 9.74 and 27.56 keV. At all other energies calibration concentrated on  $\text{N}^+$  and  $M/Q = 16$ .

Further calibrations of IMS are being carried out in the laboratory with a prototype model refurbished to be identical to the flight model in all essential characteristics. The purpose of this effort is two-fold: First to understand features of the instrument, primarily certain TOF spectra, which were not well characterized during flight unit calibration. Second, we plan to introduce a wider variety of ion species that are more characteristic of what might be expected in the ionosphere of Titan. All calibration data from both the flight and prototype units have been placed in a common format and assembled into an archive kept with flight data.

## 6.7. PERFORMANCE

Figure 32 illustrates the characteristic energy-angle response of the IMS ESA for a 16.39 keV  $\text{Ne}^+$  beam, plotted as ion count contours in the voltage (energy) elevation angle plane. The slightly asymmetric appearance of the contours is consistent with the simulated response of the toroidal top-hat analyzer (Young *et al.*, 1988). The sawtooth nature of the contour edges is an artifact of goniometer motion. Note that this figure corresponds to Figures 11 and 17a for ELS and IBS, respectively.

A set of TOF spectra taken simultaneously with the ST and LEF anodes for  $M/Q = 16$  at 1.024 keV is shown in Figure 33 (a) and (b). The actual ion flight times in Figure 33 are obtained by multiplying the indicated channel numbers by 0.78 ns. As can be seen in the LEF spectrum in Figure 33 (a),  $\text{H}^+$ ,  $\text{O}^{2+}$ ,  $\text{C}^+$ ,  $\text{N}^+$  and  $\text{O}^+$  can be identified as the daughter products of  $\text{O}^+$ ,  $\text{CH}_4^+$  and  $\text{NH}_2^+$  all of which were present in the same beam at  $M/Q = 16.00$ . The mixture can be inferred on the basis of the history of gases leaked into the source and on the makeup of filament materials. Although the calibration beam was not mass separated, it is clear that the IMS resolve beam components. The  $\text{H}^+$  peak is proportional to the amount of  $\text{CH}_4^+$ , and  $\text{NH}_2^+$ , while the amount of  $[\text{O}^+ + \text{O}^{2+}]$ ,  $\text{N}^+$ , and  $\text{C}^+$  are proportional to the parent molecular species.

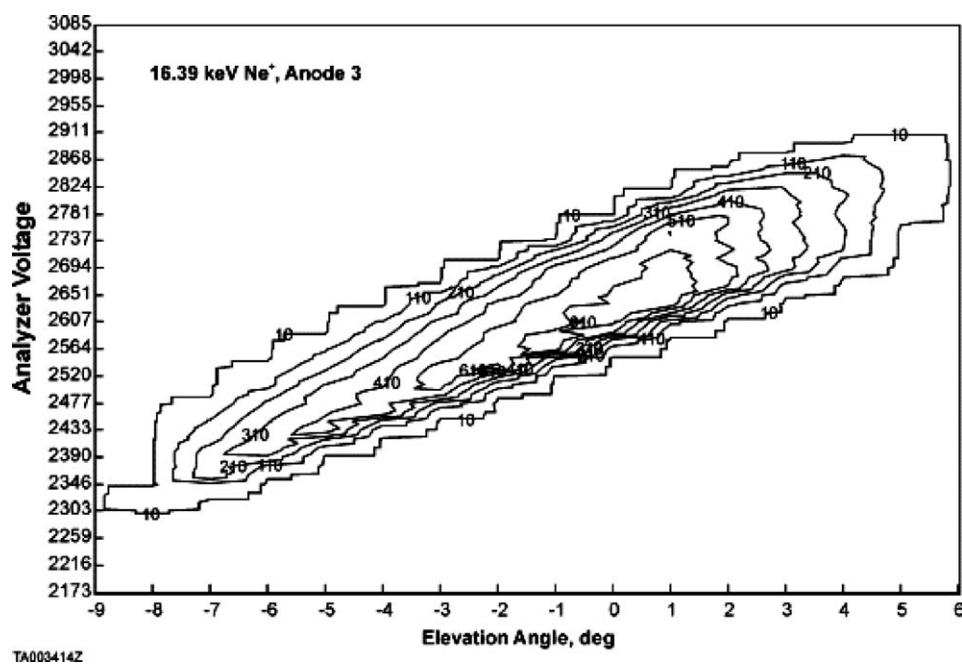


Figure 32. Ion energy (proportional to analyzer voltage) versus azimuthal entrance angle for a single elevation anode of the IMS sensor.

The corresponding ST spectrum shown in Figure 38 (b) illustrates that generally the most significant peak in the ST response is due to neutrals. Since, to first order, all neutral daughter products from an incident molecule travel with the same center-of-mass speed  $v_{\text{int}} = (2E_{\text{int}}/M)^{1/2}$  through the TOF analyzer, a single neutral peak is produced. Energy straggling and scattering in the foil tend to broaden this peak. At 1.024 keV, no positive ions appear in the ST spectrum because they are all reflected by the LEF, appearing exclusively in Figure 33(a). The two peaks labeled “E” are the result of de-focused ions that strike the LEF MCP suppression grid and grid holder. The errant ions produce secondary electrons, which are then accelerated by the LEF to the ST detector, resulting in ST peaks. Note that these two “echoes” coincide with the LEF  $\text{N}^+$  and  $\text{O}^+$  peaks. The LEF field accelerates stable negative ions leaving the foils and thus they appear at earlier times than the neutrals. This accounts for  $\text{H}^-$ ,  $\text{C}^-$ , and  $\text{O}^-$  peaks in the example. Nitrogen does not have a stable negative ion and thus does not appear in the spectrum. The noise background in these spectra is primarily due to internal scattering of particles exiting the foil and to accidental coincidences of particle events with each other (for example a START coincident with a non-related STOP event).

Data from calibration spectra have been analyzed and compared to models of IMS behavior given in Equations (3) through (6). For example, in a perfectly linear electric field the TOF should be proportional to the square root of the ion mass/charge, independent of energy. Figure 34 shows a plot of this relation for ion  $M/Q$  values of 7 and 14 ( $\text{N}^{++}$  and  $\text{N}^+$ , respectively) over a wide range of energies. Although the electric field has been purposely detuned from a perfectly linear case, the square root relation still holds quite well and can be used to identify peaks in LEF spectra. The notable exceptions are low-energy ions, which straggle badly and tend to reflect in the most non-linear portions of the field. The third curve in Figure 34 is a ghost peak caused by internal scattering (see Figure 33 (a) at TOF channel 170).

The neutral species present in ST spectra experience no electric field and hence their times-of-flight are given by effective path length divided by exit speed (Equation 6). Figure 35 (upper panel) shows a plot of measured neutral particle TOF for a wide range of incident ion  $M/Q$  and energies. The square root relation holds quite well and here again it is useful for identifying species in the TOF spectra. Energy straggling and scattering caused by the foil produce some of the scatter in this plot because of the difficulty encountered in fitting the peaks and hence identifying their centroids.

In contrast to neutral species, however, ST ions that overcome the LEF potentials experience a varying force along their paths, so modeling in this case requires integration along the trajectory (Equation 4). As an example, Figure 36 shows a comparison between the measured TOF of  $\text{C}^-$  and  $\text{O}^-$  ST ions for several energies in a simple model assuming a perfectly linear electric field. The agreement is not as good as with the LEF and neutral models, but is better than about 10%. We believe that the disparity is partly due to the non-linearity of the electric field, as well as

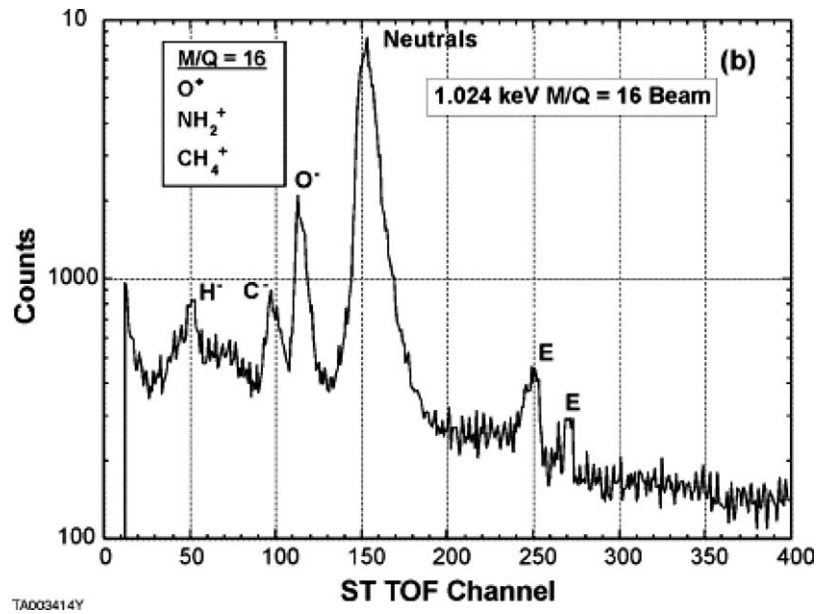
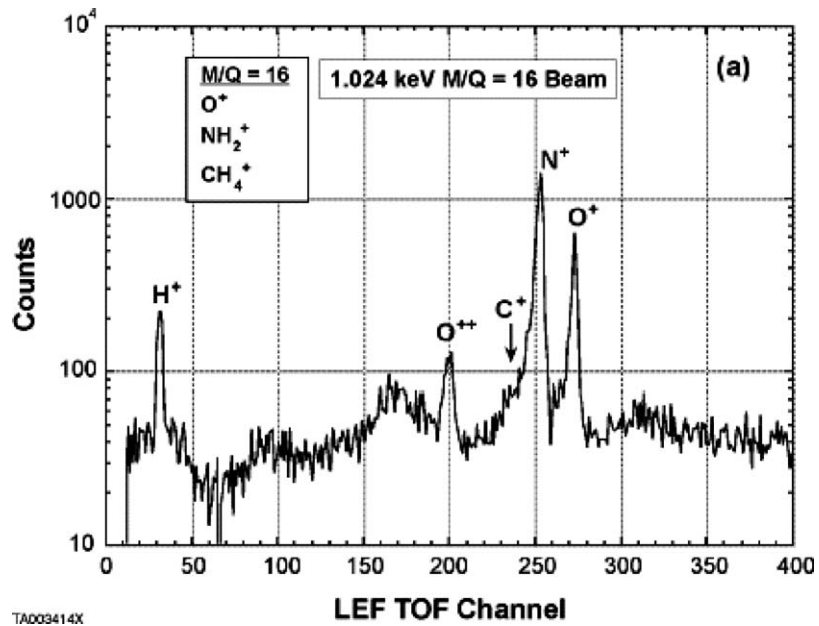
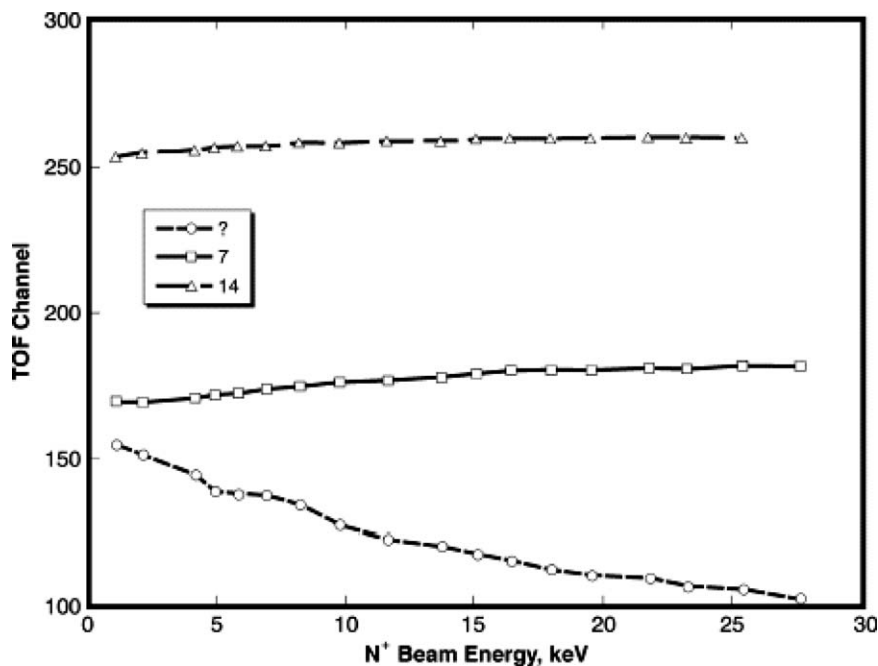


Figure 33. (a) An LEF time-of-flight spectrum for an incident 1.024 keV ion beam made up of mass/charge 16 ions including  $\text{CH}_4^+$ ,  $\text{NH}_2^+$ , and  $\text{O}^+$ . (b) The ST TOF spectrum corresponding to the LEF spectrum shown in Figure 38 (a).



TA008414Q

Figure 34. Location of the center of the  $N^+$  and  $N^{2+}$  LEF TOF peaks as a function of incident ion energy demonstrating the energy focusing capabilities of the LEF optics. The lower curve corresponds to behavior of the ghost peak evident in Figure 33 (b) at 170 TOF channels.

the mass and energy-dependent straggling and scattering caused by the foil. The foil effects are more severe for lower energies and result in a longer than predicted TOF. In addition, when a molecule breaks up in the foil the resulting components divide their energies proportionally to their masses so each has a lower energy than the original. This effect shifts the TOF of positive molecular fragments from their expected positions had they the same energy as the incident parent molecule. Thus it is possible to distinguish between an ion formed in a molecular breakup and an atomic ion of the same  $M/Q$ . Comparisons with the LEF and ST spectra (Figure 36) allows us to distinguish between molecular and atomic species, which would otherwise require a conventional mass spectrometer with much higher resolution.

## 7. Instrument System Design

This section provides a complete description of the system aspects of the CAPS instrument.

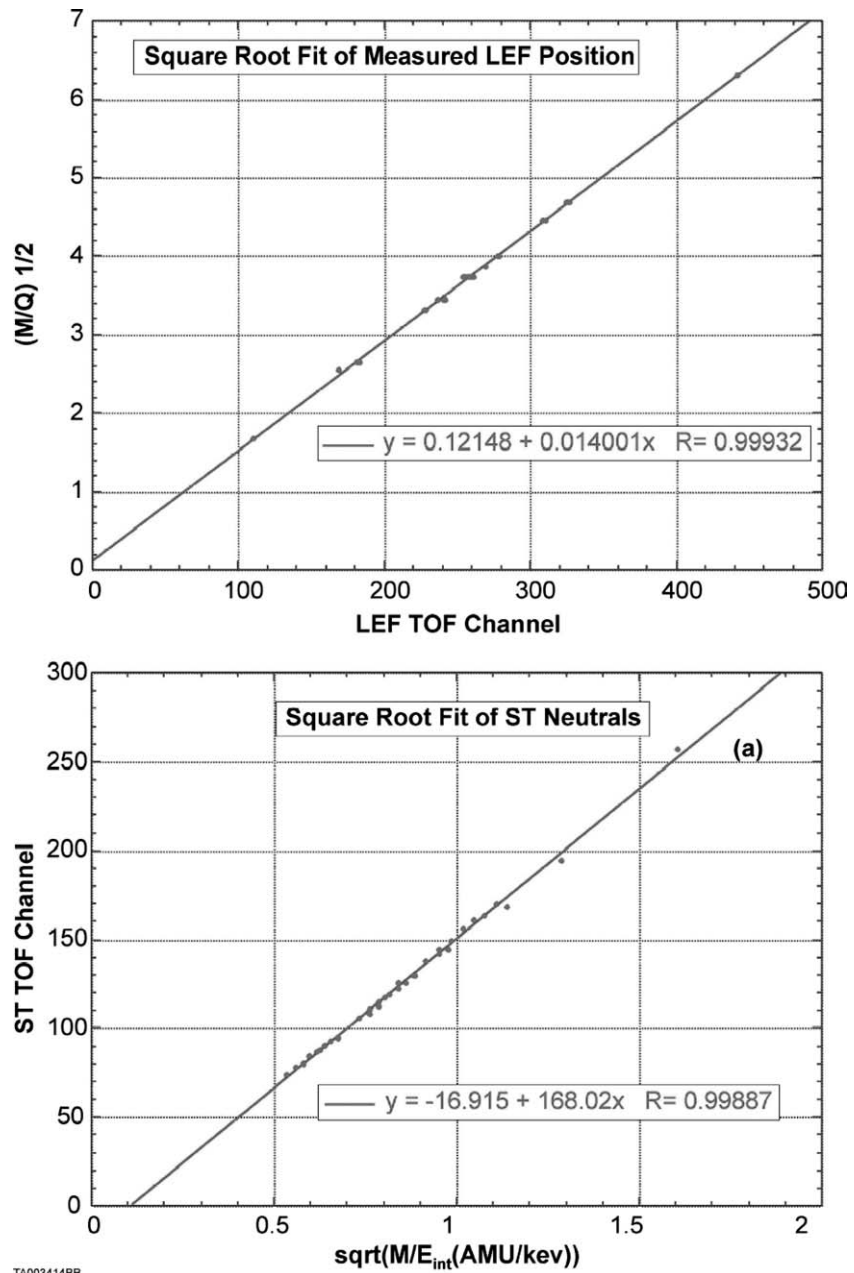


Figure 35. (a) Locations of the centers of TOF peaks as a function of ion  $M/Q$  for the ST detector. (b) Locations of the centers of TOF peaks as a function of ion  $M/Q$  for the LEF detector. Spectra were obtained at energies between 1 and 27.6 keV/e.

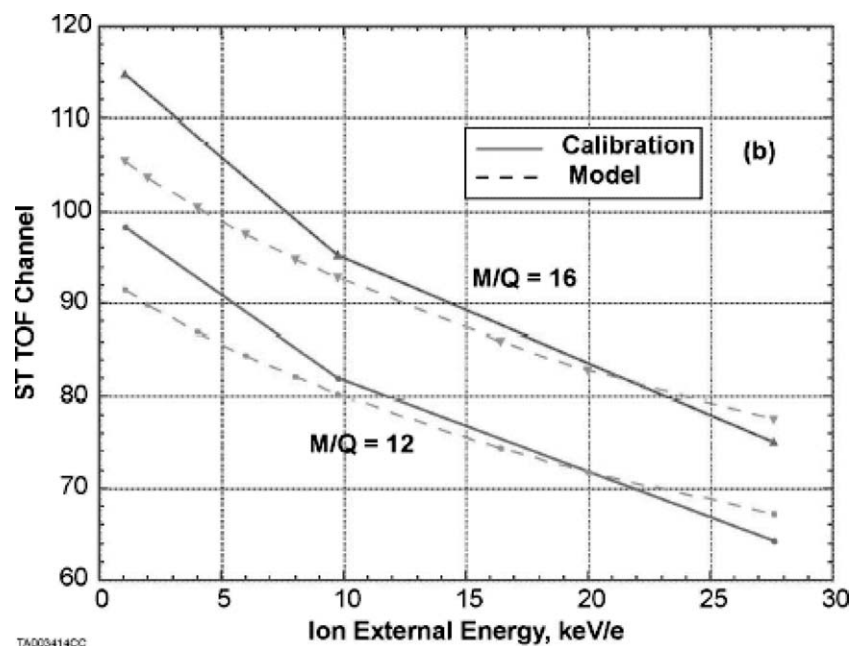


Figure 36. Comparison of the TOF peak location of negatively charged mass 12 and 16 ions as a function of ion energy external to the TOF system. The relatively simple model does not include all details of the IMS LEF fields and energy straggling.

### 7.1. MECHANICAL DESIGN

Figure 37 shows the actuator (AC). In addition to the 3 features to note in the photograph in Figure 37 are the high-voltage cables running from the IMS high-voltage units 1 and 2 to the IMS sensor (the cylindrical shape in the background) and the micrometeoroid shielding placed on the outside of the DPU. Table XI summarizes mass and power properties of the CAPS subsystems.

To have compatible electron and ion measurements, the fields-of-view of all three sensors are co-planar in elevation (Figures 4 and 38a). In addition the centers of the IMS and ELS fields-of-view are co-axial whereas that of the IBS is offset by 32.0 cm to the right in Figure 38a.

The data processing unit (DPU) houses the greater part of the CAPS electronic circuitry, and forms the central mechanical platform of the instrument. The large number and complexity of circuits needed to service three sensors, the ACT, and spacecraft interfaces determined the physical size of the DPU. To give a simple example of the electronic complexity of CAPS, consider that each of the eight DPU circuit boards is 19.0 cm  $\times$  19.0 cm square making the total board area used for electronics  $\sim 0.5$  m<sup>2</sup>. An additional  $\sim 0.3$  m<sup>2</sup> of electronics is located in the individual units for a total of 0.8 m<sup>2</sup>.

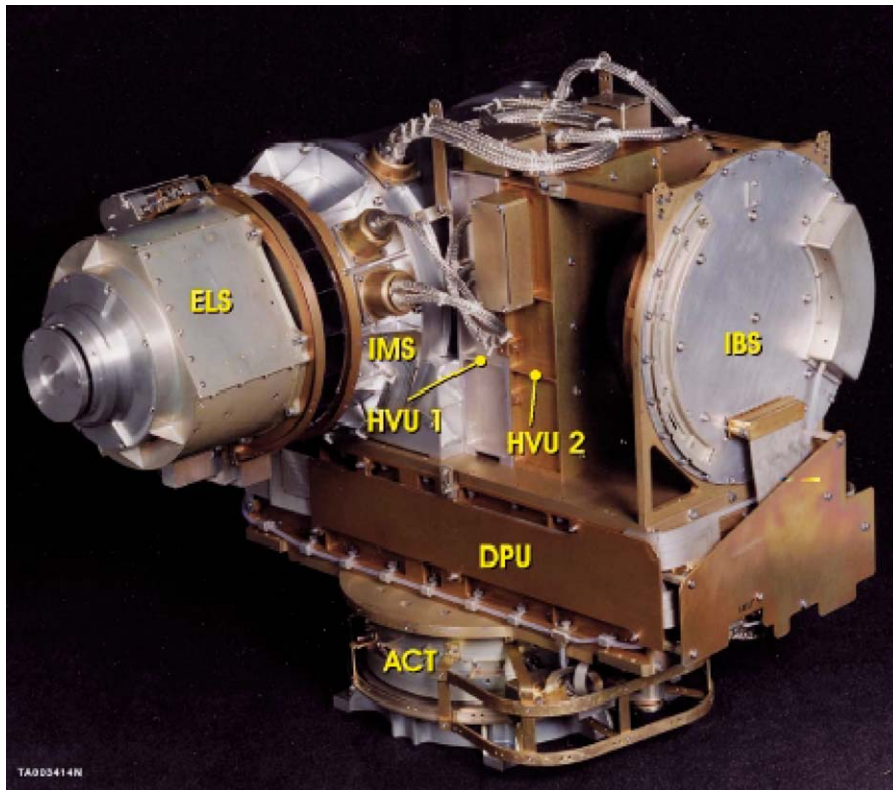


Figure 37. Photograph of the CAPS flight model prior to delivery to the Cassini spacecraft.

The presence of the ACT complicates thermal design because its bearings thermally isolate CAPS, which dissipates a maximum of 21 W, from the FPP. Therefore, the CAPS temperature is controlled independently of the spacecraft through a dedicated radiator (on the +X surface of the DPU) and electrical heaters in the instrument. The CAPS radiator is sized so that operations during the mission result in average instrument temperatures between  $-20\text{ C}$  and  $+30\text{ C}$ .

The bottom of the DPU structure is attached to a mechanical transition plate that provides attachment points connecting the DPU to the ACT assembly (Section 7.4). Six mounting feet on the base of the ACT secure CAPS to the FPP. During all test and launch activities, whenever the ACT was operated, it was done so in an upside-down configuration (see Figure 3). After final mechanical properties were measured, the transition plate was drilled such that the center of mass of the rotating portion of CAPS was positioned at the center of rotation of the ACT. This technique made it relatively easy to meet spacecraft static and dynamic balance requirements ( $<0.090\text{ kg m}$  and  $<0.060\text{ kg m}^2$ , respectively), permitting CAPS to actuate during periods when optical remote sensing (ORS) observations and

TABLE XI  
CAPS subsystem characteristics.

Subsystem	Mass (kg)	Power (W)	
		Peak	Average
IBS sensor	1.27	1.09	0.93
ELS sensor	1.40	1.90	1.50
IMS sensor	7.06	7.21	4.77
DPU	6.70	8.50	6.90
Cable and shielding	2.64	–	–
ACT	3.96	2.30	2.30
Totals	23.03 kg	21.00 W	16.40 W

spacecraft communications with Earth are taking place. Tests conducted during the cruise phase of the mission have shown that CAPS does not interfere with spacecraft pointing in any measurable way.

With six complex subsystems located externally to the DPU, 11 interconnecting cables comprising about 350 individual wires were needed outside the DPU structure. Conventional wire cables and associated connectors would have been too complicated, heavy, and bulky to be practical. In addition they would be susceptible to micrometeoroid damage and electromagnetic radiation leakage. Our approach was to design and manufacture a special set of cables made of flexible multi-layer printed circuits that were terminated by imbedded connectors. These so-called “flat” cables, which carried an outer protective shielding layer of copper, were easily bent around corners and secured to the DPU. This also made instrument integration simpler and safer than would have been possible with conventional cables. Once flat cables were implemented, a re-examination of the micrometeoroid hazard by the Cassini project indicated that cable shielding was too thin to prevent penetration by interplanetary or ring particles. Thus impact shielding was increased by introducing 1.5-mm thick aluminum “bumper” shields placed on the  $-X$ ,  $-Y$  and  $+Y$  faces of the DPU (Figure 37). As an additional precaution, the Cassini project added two layers of quartz “beta-cloth” fabric beneath the spacecraft multi-layer insulation blankets that covered CAPS. With these precautions the probability of the cables or DPU being damaged by micrometeoroid impact was estimated to be less than 4% (most of this risk occurred during successful passage through the asteroid belt).

To avoid contamination by spacecraft photoelectrons, the ELS was mounted at the far end of the IMS collimator, which, in combination with CAPS location on the FPP, placed the ELS FOV as far from nearby spacecraft surfaces as possible. However, this mounting arrangement created a cantilevered inertial load on

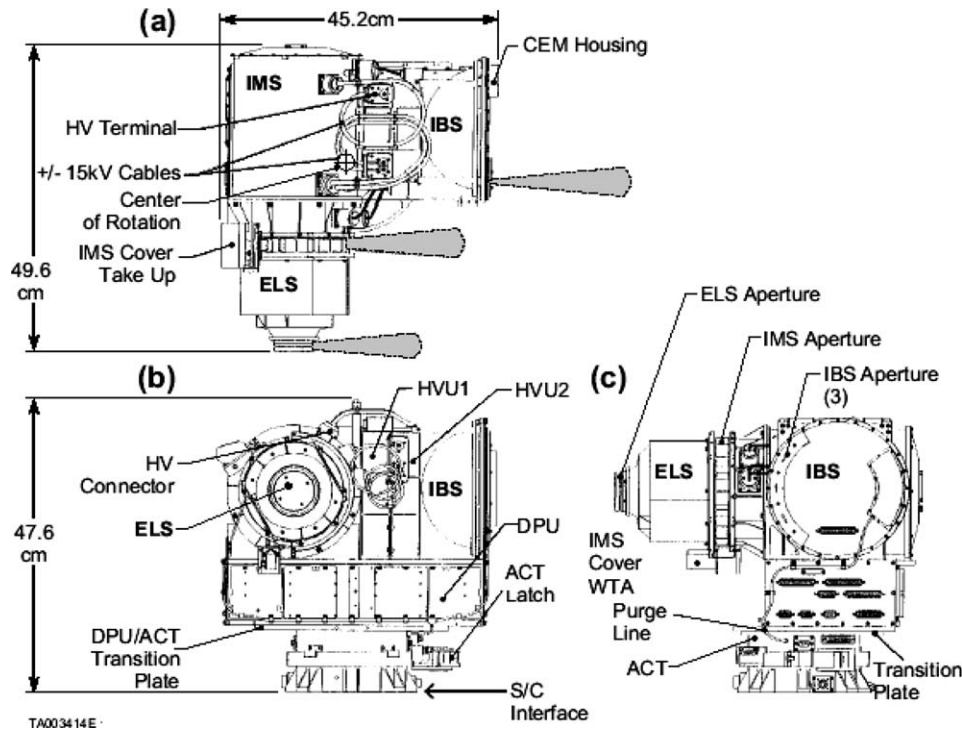


Figure 38. Orthogonal projection drawings of the CAPS flight unit showing mechanical details. Projections are in the spacecraft (a)  $X$ - $Y$ , (b)  $Y$ - $Z$ , and (c)  $X$ - $Z$  planes assuming that CAPS is in the nominal “safe” position shown in Figure 3.

the cylindrical IMS housing. Careful structural analysis was necessary to avoid mechanical resonances.

During its nominal 11-year mission, electronic components will absorb an estimated cumulative radiation dose of 100 krad behind 1.0 mm of aluminum shielding or its equivalent. Shielding calculations performed with a factor of 2 design margin showed that the walls of electronics housings required a minimum thickness of at least 1.5 mm. Although most of the electronic components in CAPS are radiation hardened to the 100 krad requirement, some are not. Care was taken to place sensitive components near the centers of individual circuit boards and then locate the boards in a way that made optimum use of the enclosures and surrounding spacecraft volumes to provide shielding. As a result, electronic components in CAPS meet the radiation design goal with margins of a factor of two or more.

Final integration of the CAPS Flight Unit on the Cassini orbiter took place at Kennedy Space Center in July 1997. At the time of integration the interface between CAPS and the spacecraft MLI blankets was problematic, especially in

areas near the junction of the moving parts of the ACT and the surface of the FPP. MLI blankets were fabricated very precisely in order to avoid snagging CAPS on the FPP. During one phase of flight operations, however, there is some evidence that CAPS did snag on the MLI. For that reason the motion of CAPS has been restricted to  $+104^\circ$  to  $-80^\circ$  in azimuth, rather than the planned  $+104^\circ$  to  $-104^\circ$  range.

*Electrostatic Cleanliness.* Differential spacecraft charging is a serious concern because all three CAPS sensors are capable of measuring particles with energies slightly below 1 eV. To ensure their performance, sensor apertures were coated with conducting black materials (copper oxide or copper sulfide deposited electrochemically), which, because of their microscopically rough surfaces, help reduce both particle and UV scattering by factors of 100 to 1,000. External aperture surfaces are bare aluminum, a sufficiently good conductor to allow adequate charge dissipation. During spacecraft integration concerns over the conductivity and uniformity of indium-tin-oxide MLI surfaces on the orbiter exterior prompted the CAPS team to request that carbon-impregnated Kapton<sup>®</sup>, similar to that used on Voyager and Galileo, be placed around the instrument. As an additional precaution, MLI blankets near the CAPS apertures were stitched on with thin stainless steel wires grounded through contact with blanket material.

*Contamination Control.* Many sensor components (detectors, carbon foils, high surface resistance insulators and chemically blackened surfaces) are sensitive to chemical contamination and particulate debris that might be introduced during ground handling, testing, or launch. The CAPS detectors are all electron multipliers that depend on the electron yield of a thin layer of reduced lead-silicate glass. Surface chemical contamination by, for example, compounds found in circuit board coatings, reduces multiplier efficiency and gain. Water and other condensable molecules are easily adsorbed on multiplier surfaces only to outgas once in vacuum, potentially leading to HV breakdown. Carbon foils in IMS interact with incoming ions to emit secondary electrons in much the same way that multipliers do. The foils are hygroscopic and easily form van der Waals bonds with polar compounds such as water (e.g., during launch). High-voltage insulators and high-ohmic resistors ( $\sim 10\text{ G}\Omega$ ) are also concerns. Thus prolonged exposure of internal sensor surfaces to water vapor and other volatiles can create large internal gas loads that need to be avoided. For this reason, and because the carbon foils are sensitive to acoustic vibration during launch, the IMS was fitted with a retractable cover released several months after launch. Operation since then has shown no signs of contamination or foil loss.

## 7.2. ELECTRICAL DESIGN

Figure 39 is a schematic overview of the major components of the CAPS electrical system and its command, control and data flow aspects. The system is made up of



TABLE XII  
Primary functions of DPU circuit boards.

Board Name	Functions
1. Spacecraft Interface	Bus Interface Unit, ACT interface, IMS cover release, ACT release, heater control
2. Low Voltage Supply	Low voltage converters, +30 V filter, housekeeping
3. IBS/ELS Interface	Master timing, IBS and ELS command and data interfaces, IBS HV control, HV safe/arm
4. IMS Interface	HV control and safe/arm, analog data, power synchronization
5. TDC	TOF data acquisition, TDC and coincidence logic, FEE control, FIFO interface with SAM
6. SAM	Pace 1750A processor, TOF, TOF accumulator, and EVENT modules, local memory for SAM LUT's
7. CPU1	Pace 1750A processor, memory management unit; 256 kwords local memory; 16 kwords PROM; ELS, IBS, HVU1, HVU2, CPU2, ACT control functions
8. CPU2	Pace 1750A processor, memory management unit, 256 kwords local memory, 256 kwords shared memory, 8 kwords boot PROM, SAM control

*CPU1 and CPU2 Microprocessors.* The CPU1 and CPU2 microprocessors are located on separate circuit boards together with associated memories. With reference to Figure 39, the CPU1 is the primary CAPS control and data processing unit. Its address and data control bus extend to the IBS/ELS interface board, the IMS high-voltage control board, and the BIU. The CPU2 is dedicated entirely to IMS data acquisition and processing as well as to control of the TDC and SAM. Both CPU1 and CPU2 can access  $10^6$  16-bit words of memory address space via individual memory management units. CPU2 contains an additional 2,56,000 words of shared memory accessible by CPU1.

*Low Voltage Power System.* The LVPS provides sensor analog and digital electronics with a variety of regulated voltages including ELS ( $\pm 8$  and  $+5$  V), IBS ( $+5$  and  $-15$  V) and HVU2 ( $+5$  and  $\pm 15$  V). Each high-voltage supply is powered through individual current-limited  $+15$  V lines controlled by separate solid-state power switches. The  $+15$  V lines are fused to prevent failure in any one circuit from damaging others.

*IBS/ELS Interface Board.* This board contains the master CAPS timing generator used for subsystem synchronization and data acquisition cycles. The timing signal is divided down to three basic periods: 7.8125 ms (the basis for IBS sampling, ACT micro-stepping, and timing interrupts to CPU1), 31.25 ms (ELS sampling interval), and 62.50 ms (IMS sampling interval). The master timing generator allows CPU1 software to synchronize CAPS operations to the scheduled repeat cycle of the

spacecraft. This is accomplished when the software sets a bit in hardware to start the master timing circuit after the appropriate real-time interrupt signal has been received from the BIU. The master clock has the capability to be divided down still further to lengthen sensor sampling periods by factors of 2 to 8.

The ELS/IBS board also contains three 16-bit counters making up the IBS data acquisition interface. An 8-bit bus controls high-voltage supplies for the IBS detector and ESA. The ELS data acquisition interface consists of a 16-bit one-way bus to the DPU that reads out eight registers in which detector counts are stored (corresponding to the eight elevation sectors). In addition an 8-channel 8-bit analog multiplexer in ELS sends housekeeping status to CPU1. A similar bus operating in the opposite direction allows CPU1 to command ELS. In addition to these functions, once power is applied to the ACT, CPU1 sends a 16-bit word every 7.8125 ms (equal to the IBS stepping cadence) to control acceleration, scan, deceleration, and stop modes.

*IMS HV Interface Board.* As mentioned earlier, CPU1 controls operation of the HV supplies located in HVU1 and HVU2. The HVU1, which produces  $\pm 14.56$  kV for the TOF, is powered directly by the spacecraft +30 V bus through a redundant, optically isolated, current-limited switch controlled by CPU1. HVU1 and HVU2 are controlled independently by 8-bit command words. The HVU2 produces ESA and two MCP detector high voltages in much the same way as the IBS and ELS high-voltage supplies. In normal operation CPU1 writes a 14-bit word to the ESA stepping supply every 62.5 ms to select 63 pre-programmed ESA voltage steps. CPU1 also controls the LEF and ST MCP detector high voltages using separate 8-bit command words.

Two 16-channel analog multiplexers process analog monitors that go into the housekeeping telemetry data. Also on this board are separate SAFE and DISABLE control lines for all nine of the CAPS high-voltage supplies. The lines are routed to a SAFE/ARM connector (removed before launch) located on the board and accessible from the outside of the instrument. Its purpose was to provide visual assurance during ground operations that CAPS sensors could not be commanded inadvertently above 3% of maximum voltage.

*Time-to-Digital-Converter (TDC) and Spectrum Analyzer Module (SAM).* These two units are dedicated to converting raw IMS detector signals into TOF spectra and processing the data to identify ion species. They were discussed separately in Sections 6.5.2 and 6.5.3.

*Grounding.* CAPS is designed with single point secondary ground. The signal ground connection to chassis is located on the DPU mother-board close to the low voltage power supply. During testing after system integration it turned out that sensitive charge amplifiers near the ELS, IMS, and IBS detectors required additional grounding. As a consequence, the grounding concept was changed to allow additional connections between these signal grounds and chassis to optimize overall noise performance. The best performance was achieved by connecting signal-grounded internal cable shields to chassis at the sensor end of the interface

cables. It should be noted that the isolation between primary and secondary power was not compromised by this arrangement.

*Fault Protection.* To prevent a failure in a subsystem from becoming catastrophic and damaging another subsystem or the entire instrument, all power lines exiting the DPU have been fused using dual redundant fuses conservatively rated for at least twice the nominal peak current. Custom-designed, current-limited solid-state switches protect power lines switched by the DPU, namely the ACT motor drive and latch, HVU1 and HVU2 converters, and supplemental heaters. Similar to the fusing philosophy, current limiting is set at twice the nominal peak current on a line.

In addition to fusing subsystem loads, other precautions were taken with the sensor high-voltage systems including SAFE/ARM controls implemented in software (in addition to hardware controls discussed above). Individual high-voltage converters must be armed and enabled by separate commands before high voltage will appear at the outputs. The more sensitive CAPS electrical circuits are protected from damage that may occur as the result of momentary ground loops associated with discharges by so-called “zap-traps.” These provide a low inductance return path from the chassis structure to the origin of the high voltage, i.e., HV ground in the individual HV generators. Zap-traps consist of two parallel fast diodes mounted in opposite directions between HV return and structure.

The health and safety of the CAPS electrical system is monitored via ~90 housekeeping channels whose contents depend on instrument mode. During maintenance mode housekeeping data reflect primarily low-voltage power supply, temperature, and ACT status. During normal science, emphasis is placed on high voltage and system-status monitoring. The CPU1 contains a 12-bit ADC (Figure 39) that samples the HV output monitors, low-voltage supplies including total current drawn on the 28 V line from the spacecraft, the ACT position encoder, and the temperature at six locations within CAPS. To provide the required thermal environment, CAPS relies on two types of heating elements located in the DPU. Supplemental heaters are controlled by commands to CPU1 (Figure 39). They provide additional heat that may be needed when the instrument is operating in a reduced power state. Supplemental and replacement heaters are controlled by the spacecraft and are intended to maintain both the CAPS thermal environment and that of the FPP when CAPS is turned off.

### 7.3. FLIGHT SOFTWARE

#### 7.3.1. *Software Description*

The primary functions of the CAPS flight software are to (1) maintain communication with the spacecraft telemetry and command systems, (2) control operation of the CAPS sensors and actuator, (3) generate data acquisition and telemetry products, and (4) carry out internal checks of system status. Figure 40 shows a detailed data flow diagram of the software control and data flow system.

The multi-processor hardware system (CPU1, CPU2, and SAM) distributes loosely coupled, fixed software tasks. The CPU1 is the “front end” of the data system and is the only processor that communicates directly with the spacecraft (Figure 40). The CPU1 collects data from all three sensors as well as housekeeping data, and formats it into “CCSDS” (Consultative Committee for Space Data Systems) standard transmission packets, which are then sent to the spacecraft command and data system (CDS) via the BIU. As can be imagined, CPU1 executes independently of CPU2 and SAM, which are slaved to the former. SAM in turn is slaved to CPU2. During operation the CPU2 extracts TOF data processed by SAM from a random access memory (RAM) shared between the two. CPU2 data are then communicated to CPU1 via another set of shared memory.

Spacecraft and instrument operational mode choices define the CAPS operating state, telemetry rate, data volume, data product type, and power allocation. As part of this scheme, the spacecraft operational mode and current physical data rate are communicated to CAPS once per second. CAPS telemetry is divided into two streams: science and housekeeping. The housekeeping stream has a nominal physical data rate of 22 bits/s dropping to 11 bits/s in maintenance mode. Science “logical” data rates can be varied by command from 16 kbps down to 0.25 kbps in factors of 2. However, the logical rates must always be smaller than or equal to one of two “physical” rates (16 and 2 kbps) set by the spacecraft CDS. Any data volume difference between physical and logical rates is filled with zero length

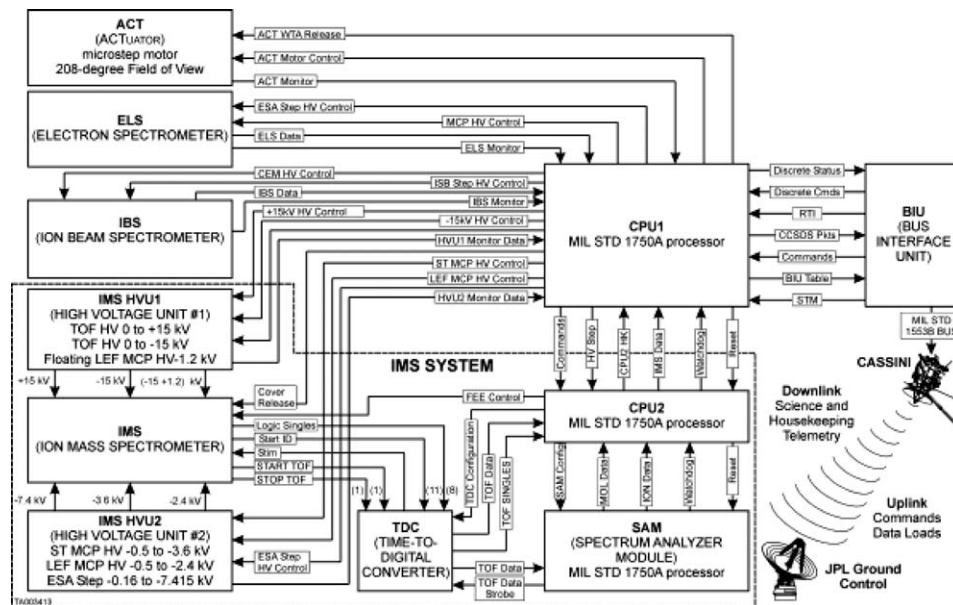


Figure 40. Detailed schematic of the CAPS data flow and command system.

packets (ZLP) so that the CDS retains the expected packet pick-up rate and is unaware of any differences in data volume. The ZLPs are recognized by the CDS and are not stored on the spacecraft solid-state recorder (SSR), thus allowing CAPS science data flow to be tailored to the allocated SSR volume without loss.

Commands or command sequences are uplinked to the spacecraft roughly every 28 days during the tour phase of the mission. Once uplinked they may be executed in real-time, stored in the spacecraft solid-state recorder (SSR), or stored in CAPS RAM memory as instrument-expanded (command) blocks (IEB's). Command sequences containing time-ordered triggers for executing IEB's are stored in the SSR from which they are sent to CAPS. Real-time commanding is also available if necessary for time critical operations.

Data acquisition, high-voltage control, and spacecraft communications with CAPS (Figure 40) all take place at times determined by the spacecraft clock broadcast once per second; or with synchronization messages and real-time interrupts (RTI) sent once every 0.125 s. The CAPS hardware sample clocks are synchronized to the RTI signal during CPU1 initialization. Internally CAPS organizes data based on A- and B-cycles introduced earlier in Section 6.5.3.

### 7.3.2. Software Operation

CAPS flight software functions are split between PROM-resident and SSR-resident software depending on instrument mode. PROM resident code includes functions needed to implement maintenance, low power, and CPU2/SAM-Ready modes. Table XIII is a list of operational modes and their characteristics. The transitions and interrelationships between these modes are shown in Figure 41. When power is first applied, or when the DPU has been commanded to reset by the spacecraft, CAPS "boots up" from code stored in PROM and begins execution of memory checks, BIU initialization and RTI synchronization. It also determines the commanded operational mode and begins execution. In the initial "ON" state, code from the SSR is read to CPU1, which then initializes its own plus CPU2 and SAM operations, bringing all three processors to a "READY" state. From this the LOW POWER, NORMAL SCIENCE, or SLEEP modes can be reached. When CAPS is commanded to the "OFF" state it ramps down any high voltages that are on and then returns to LOW POWER mode before power is turned off.

*Maintenance Mode.* During parts of Cassini cruise phase the maintenance mode was run to exercise the ACT stepper motor and bearings once every 3 months during spacecraft periodic instrument maintenance (PIM) operations. No science data were taken. Only simple housekeeping packets containing ACT angular position as well as instrument current, voltage and temperature monitors were returned at 11 bits/s. During the first and third PIM periods following launch, wax thermal actuators released the ACT latch and IMS cover mechanisms, respectively.

*Low-voltage Mode.* The initial command from the spacecraft causes CAPS to boot up from PROM into a low-voltage state. Initially the instrument ignores any accidental commands to the ACT or high-voltage units as a safety precaution. Only

TABLE XIII  
CAPS operational states.

State	Power (W)		Status		Telemetry mode		Code source	
	Average	Peak	ACT	HV	HK*	SCI*	PROM	SSR/Gnd
Maintenance	15.8	19.1	on	off	Maint.	ZLP	X	
Low voltage	12.5	12.5	off	off	Sci.	ZLP	X	X
CPU2/SAM ready	13.2	13.2	off	off	Sci.	ZLP		X
Sleep	13.2	13.2	off	on	Sci.	ZLP		X
Normal science w/o ACT	13.4	18.0	off	on	Sci.	Sci.		X
Normal science w/ ACT	16.4	21.0	on	on	Sci.	Sci.		X

\*HK: housekeeping mode; SCI: science mode; Maint. data; sci. data; ZLP: zero length packet.

housekeeping is produced at 22 bits/s. From this mode CAPS can be commanded to enter the CPU2/SAM-ready mode (Figure 41), which is simply a transition state between PROM-based and RAM-based versions of the low-voltage mode. In the CPU2/SAM-ready mode, CPU1 releases the CPU2 processor, which then waits for program load commands from CPU1. Both CPU processors and the SAM are then ready to accept program loads in assisted load format (ALF) blocks from the SSR. After all three processors are loaded, CPU1 is commanded to begin execution while CPU2 is put back into reset. At this point CAPS is again in low-voltage mode, but code is now executing from instrument memory (instead from PROM) and CAPS can be commanded to enter normal science mode.

*Normal Science Mode.* Normal science is unique because it is the only one in which high voltages can be applied, the CPU2 and SAM are operational, and a full range of ACT motion is possible. Once CPU1 releases CPU2 from reset, the latter releases SAM and then initializes SAM and TDC based on a table controlled by ground command (SAM group tables were discussed in Section 6.5.3). If, during normal operations, the SAM or TDC configuration, or the SAM group table, are changed, then CPU2 puts SAM into reset.

In addition to controlling telemetry rates and other subsystems, CPU1 also controls sensor energy scans and scan rates. The scan table contents are set by ground command as are the rates. Normally ELS and IBS scans require 2 s whereas IMS requires 4 s. During normal science mode data are acquired in the following way: A-cycle data from IBS and ELS are accumulated and stored one-half of CPU1's double-buffered memory, while the other half of memory is being read out and processed. SAM data are gathered in the same way by CPU2 before being extracted by CPU1 during the next A-cycle. At the same time that A-cycle data are

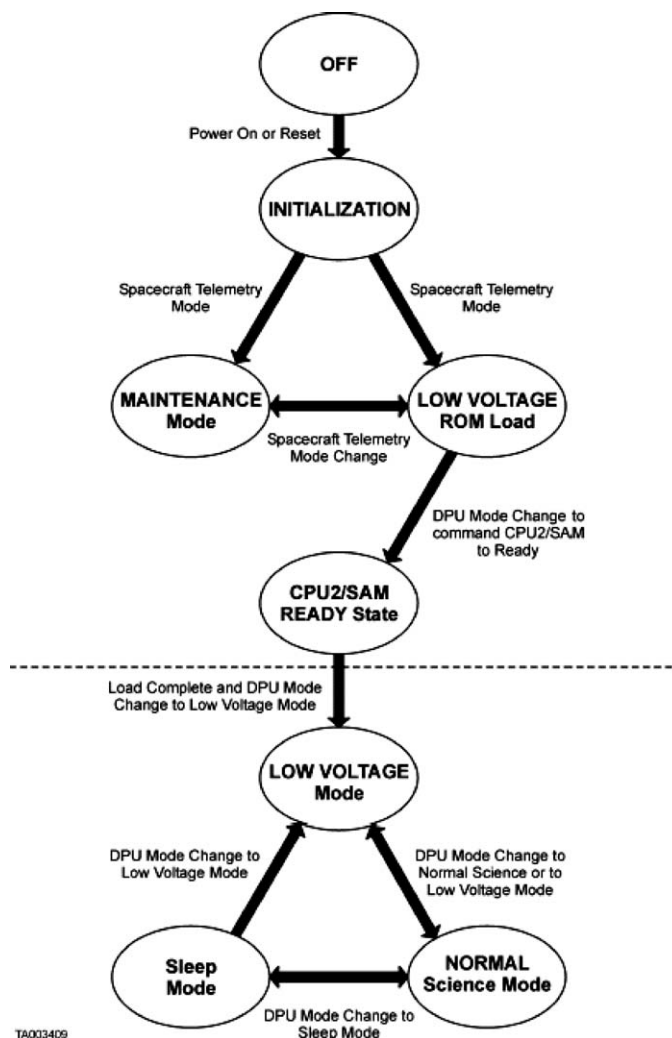


Figure 41. CAPS operational state diagram. Mode states above the dashed line are part of the CAPS initialization process; below the line are possible standard operational states.

acquired, CPU2 collects TOF data from SAM on the basis of a B-cycle (consisting of 8 A-cycles). Details of B-cycle data products were discussed in Section 6.5.3.

*Sequential Event Mode.* This mode is a diagnostic of the entire TOF system applicable only when CAPS acquires data at 16 kbits/s. In it SAM collects up to 16,000 TOF words sequentially at a fixed energy step over a period of two A-cycles. Each word corresponds to a single particle striking one of the detectors. During the next two A-cycles SAM computes ION data products corresponding to this data. The procedure is repeated for two more energy steps, acquiring 48,000 events in a single B-cycle.

*Sleep Mode.* Sleep is a reduced operations mode from which CAPS can quickly emerge (e.g., following the firing of the spacecraft's main engine during Saturn orbit insertion). In sleep mode the HVU1 voltages remain on at predetermined high, but safe, level (e.g.,  $\pm 12$  kV). All other supplies can be turned off. In addition CPU2 and SAM are held in reset and the ACT is parked and turned off. Only housekeeping data are produced.

### 7.3.3. Fault Protection

The CAPS flight software contains several features designed to detect and report faults and recover from them "gracefully." Among the most critical features, because it controls command and data transmission, is a watchdog timer that detects real-time interrupts (RTI) from the spacecraft. If one is missed, the timer generates an artificial RTI within CAPS. CPU2 also contains a watchdog circuit. If this expires, an interrupt is generated in CPU1 and an error reported in housekeeping. In the worst case, should the CPU1 watchdog expire, a reset of the CAPS system will occur automatically and a message will then be generated by the spacecraft telling the ground controllers that CAPS is in an OFF state. A second feature is on-board verification of all software and commands sent to CAPS. Commands are also checked for valid operations codes and appropriateness for the current instrument state. Detected command errors and their specific nature are reported in housekeeping. A third fault protection, mentioned earlier, is that CPU1 checks all high-voltage commands for validity before allowing execution to proceed.

## 7.4. ACTUATOR

The primary function of the CAPS actuator (ACT) is to provide articulation of the three sensors and their fields-of-view over the lifetime of the Cassini mission (nominally 500,000 cycles). To this end the ACT rotates the instrument at a nominal rate of  $1^\circ/\text{s}$  around an axis parallel to the spacecraft Z-axis (Figures 3, 4, 37 and 38). Among the many requirements placed on the ACT was a lifetime of 5,00,000 cycles without failure. Although the maximum range of actuator motion possible is  $\pm 104^\circ$  in azimuth centered on the spacecraft  $-YZ$  plane (Figure 4), the useful range is restricted to  $-80^\circ \leq \psi \leq +104^\circ$ , where at  $\psi = 0^\circ$  the FOV is aligned with the spacecraft  $-Y$  axis. Most FOV encroachments that do occur are beyond  $-80^\circ$  (Figure 5). At the  $\psi = 0^\circ$  position all three sensors are aligned with the ORS instrument FOVs. At  $\psi = +90^\circ$ , they are aligned with the FOV of the INMS and the MIMI/CHEMS instruments. In spacecraft coordinates the rotation range corresponds to clock angles of  $256^\circ$  through  $0^\circ$  to  $80^\circ$ .

The actuator uses a 90 pole, two-phase, synchronous SAGEM motor that makes use of direct mechanical coupling. The motor is driven by a sine-cosine pair of phase voltages whose values are stored in the DPU and then sent to the actuator at a rate of 128 Hz via a parallel data interface. The phase voltage waveform

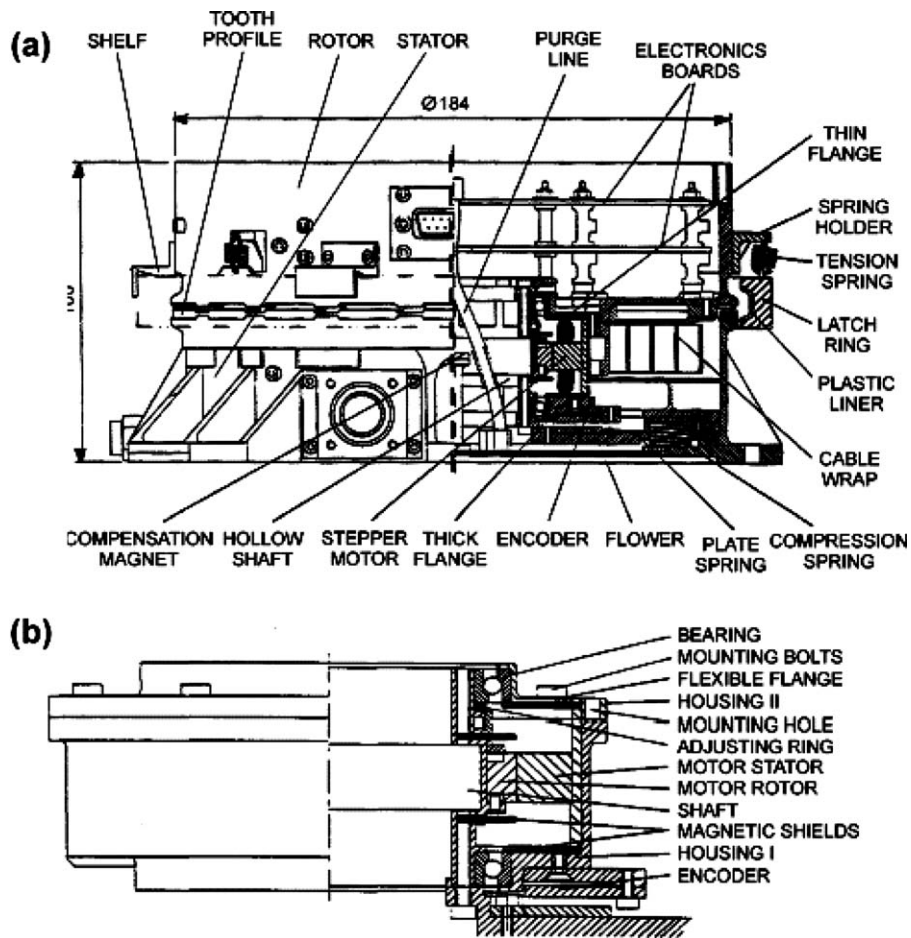
table comprises one electrical cycle ( $4^\circ$  of mechanical motion) with a resolution of 128 steps/degree. The same waveform pair is used for both directions of rotation as well as for acceleration and deceleration. Motor control electronics, DPU interface, and synchronization and timing logic are all located on a single circuit board housed inside the ACT (Figure 43). The DPU receives acceleration data that are used to determine the step size for the pointer of the phase voltage vector: If the received acceleration signal indicates that the actuator speed is decreasing due to changes in the detent torque of the motor, the nominal pointer increment of one step every 7.8125 ms is increased to two or three steps to increase motor torque and thus compensate for deceleration. Correspondingly, acceleration is compensated by not incrementing the pointer or even by taking a step “backwards” in the table.

Ideally the cumulative sum of step corrections should be zero. Due to possible offsets in the acceleration analog-to-digital converter this might not be the case. A cumulative error would cause the rate of rotation to deviate from the nominal  $1^\circ/\text{s}$ . To prevent this, a second control loop in the DPU integrates the step corrections and adds or deletes waveform pointer steps to keep the sum of corrections at zero. Because of Cassini’s stringent pointing and stability requirements, ACT motion was designed to be mechanically very smooth. Scan motion is controlled by a direct-drive stepper motor and custom designed control electronics. Active position sensing, feedback and acceleration/deceleration ramps help further smooth its motion. A resistive encoder measures angular position which is fed as an analog signal to the DPU where it is differentiated twice, producing a signal proportional to angular acceleration, which is then used to control the motion.

The endpoints of the sweep are commandable by CPU1, which generates detailed micro step values sent to the motor control unit. Once the ACT is within  $12^\circ$  of the end point of a sweep deceleration begins. After reversing direction, the motor accelerates out to  $12^\circ$  and then sweeps back the other way in windshield wiper fashion. Pointing accuracy during this motion is  $\pm 0.5^\circ$ . By using the full ACT range combined with the ELS and IMS FOV, a  $160^\circ \times 180^\circ$  swath of the sky can be scanned approximately every 3 min, independent of spacecraft orientation.

The ACT also serves as the mechanical platform for CAPS and, during spacecraft ground testing and launch, holds the instrument “upside-down” on the spacecraft pallet (Figure 3). During launch the forces on the ACT reached 28 g’s. These and other special requirements made the motor unit design very demanding. In addition to a minimum lifetime of 500,000 cycles, thermal gradients between CAPS and the spacecraft pallet pass through the bearings but must not cause significant increases in friction, or otherwise damage them. Finally, the ACT, which contains magnetic materials, had to meet a stray field requirement of 2.5 nT at 1.0 m, requiring the housing and bearing materials to be non-magnetic. One final important feature is a hollow shaft through the motor that allowed a flexible purge tube to be run from the spacecraft purge system up through the DPU to the sensors.

An important element of the ACT is bearings and bearing flanges, which are fitted together precisely to meet high concentricity requirements on their relative motion



TA003414AA

Figure 42. (a) Elevation view (left side) and cross-sectional view (right side) of the actuator. (b) Elevation and cross-sectional views of the ACT motor assembly.

(Figure 42). Because of residual magnetic field requirements there were only a limited number of materials that could be used. Aluminum alloys were avoided because of their high coefficient of thermal expansion. Moreover, common bearing steels are magnetic. We therefore chose instead AISI 316 steel as housing material and very precise non-separable angular contact ball bearings made of copper-beryllium alloy. Another important magnetic component of the ACT is the SAGEM hybrid stepper motor that provides 300 mNm of torque while requiring only 65 mA of current. Stray fields from the stepper motor were controlled by mounting  $\mu$ -metal shields on mating housing parts and adding a small compensation magnet on the

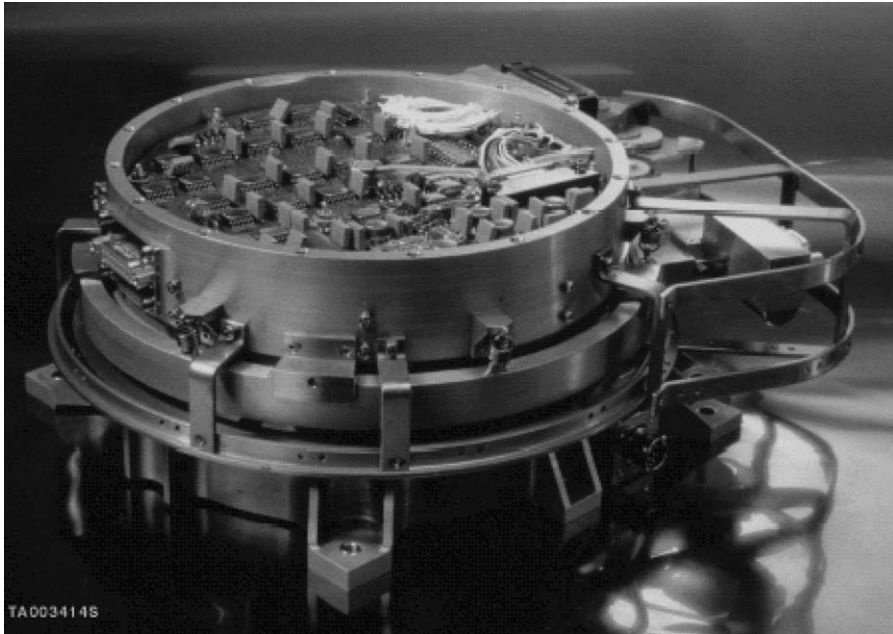


*Figure 43.* Photograph of the ACT and associated launch latch mechanism (structure on right hand side of ACT) with the DPU mounting flange removed.

bottom of the housing to cancel the motor's first-order dipole field. The residual magnetic moment of the shielded ACT was measured to be 4 nT at 1 m slightly exceeding the requirement for 2.5 nT.

Bearing lubricant and rolling surfaces easily suffer severe damage if the balls do not roll but rather skid along the ball track. Therefore it was essential to ensure sufficient bearing preload and lubrication (ion plated lead coatings). Based on life testing the bearing preload value was set at 35 N while the motor friction torque was measured to be  $\sim 5$  mNm.

The ACT bearings could not carry CAPS launch loads, which are transferred through the ACT structure to the latch clamp ring. The latching device can be characterized as a Marman or V-band clamp (Figure 42) that works by pressing the ACT rotor and stator rigidly against each other. A plastic serrated ring made of PEEK (poly-ether-ether-ketone) was placed between the clamp and the ACT parts to prevent rotation under vibration loads when the ACT was latched.

The CAPS pointing direction is measured with a resistive encoder mounted between the motor housing and a non-rotating flange. The encoder voltage is converted to a digital signal used to adjust the pointer in the motor phase-voltage table. This arrangement results in a velocity controller that damps mechanical oscillations (caused by the proximity of the main torque ripple component of the motor at 1 Hz),

to the resonance frequency of the mechanical system at 1.3 Hz. Another feature is that two limit switches, which give a signal at hard stops located at  $\pm 110^\circ$  with respect to the sweep center, can be used for position calibration.

When being latched the rotor moves 2 mm downwards (see right cutaway view of Figure 42a) and the motor assembly moves with it. Compression springs keep the upper bearing preloaded to take up vibration loads on the shaft and flange during launch. The lower bearing carries no external loads. When unlatched, the rotor, shaft and flange all move back to their upper position and the flange rests against the ACT stator structure. In this way the latch compression springs do not load the bearings or motor assembly in the released state.

## 8. Planned Observations, Instrument Modes and Operations

### 8.1. PLANNED OBSERVATIONS

The Cassini orbital tour offers the opportunity to study essentially all regions of Saturn's magnetosphere and the interactions between the magnetosphere and Titan, icy satellites and ring particles. However, spacecraft orientation and limited data volume will prevent CAPS from obtaining the highest quality data at all times. In this section, we describe the main limitations placed on CAPS measurements and our plans to maximize scientific returns despite these limits.

One method of increasing the scientific return is through the use of magnetospheric and other models that can be updated as our knowledge base increases. Despite the fact that Saturn's magnetosphere is known only through three spacecraft encounters supplemented by Earth-based observations, enough information exists to create simple models that serve as an initial guide for planning observations. For now, a limited number of science models are available. A number of workers have addressed the problem of modeling the shape and plasma populations found in the saturnian magnetosphere. Among them are Richardson and Sittler (1990), Richardson (1992, 1995), Maurice *et al.* (1995, 1996a, b), Richardson *et al.* (1998), Slavin *et al.* (1983), and Behannon *et al.* (1983). Connerney *et al.* (1983), Davis and Smith (1990) and Maurice and Engle (1995) have constructed magnetic field configuration models. Finally, Maurice *et al.* (1996b) have constructed a usable model of the saturnian magnetosphere capable of giving the probable locations of saturnian plasma boundary features such as the magnetopause.

Reliable determinations of parameters such as ion density and flow velocity may not be possible when the peak of the velocity distribution is outside the instrument's roughly hemispheric field of view. Poor pointing of this sort will be a frequent occurrence during the mission because the spacecraft's remote sensing instruments are body-fixed, requiring spacecraft turns to observe and track various objects within the saturnian system. The orientations required for these remote sensing observations may or may not allow CAPS to observe the peak of the ion velocity

distribution. More often than not, the pointing requirements are compatible, but only with an appropriate choice of the spacecraft's secondary axis (e.g., the rotation angle about the boresight of the remote sensing instruments). Spacecraft orientation is further restricted by the need to keep the Sun from illuminating the infrared instruments' radiators. Available data volume will also limit CAPS measurements. The spacecraft will, on average, return 1.75 Gbits of data per day throughout the tour. If CAPS operated at its full, 16 kbps data rate, it alone would generate 1.38 Gbits of data per day. Given that the Cassini spacecraft carries 12 instruments, CAPS clearly will have to operate on average at significantly lower rates for much of the mission.

To manage the restrictions on pointing and data volume, the Cassini MAPS (Magnetospheric And Plasma Science) instruments have adopted a strategy that mixes low-rate survey measurements with coordinated, focused observing campaigns. The survey provides a continuous, although limited, dataset covering the entire mission, whereas the campaigns provide full quality data in regions of interest. The MAPS instruments have planned various campaigns to study solar wind control of Saturn's aurora, magnetospheric boundaries, the magnetotail, Titan, the Titan torus, the inner magnetosphere, icy satellite and E ring interactions with the magnetosphere, and low-altitude crossings of auroral field lines. Table XIV shows the amount of time and the locations the spacecraft will be in various parts of the magnetosphere, as well as the anticipated times that will be part of MAPS campaigns. Figure 44 shows the arcs of the spacecraft trajectory corresponding to campaign periods. For orbits 0 through 22 (orbits with an apoapsis on the dawn side of the planet) the table and figures represent campaigns in the mission's integrated science operations plan. The science operations plan for later orbits is still under development at the time of this writing.

In survey mode, the CAPS instrument will alternate between 500 bps and 4 kbps data rates. Normally, there will be a repeating,  $\sim 30$ -min pattern of six B-cycles at 500 bps followed by a single B-cycle at 4 kbps. This strategy is intended to provide a dataset without gaps, and which includes in the worst case at least one high-rate observation every  $0.3R_S$  along the spacecraft's trajectory. During the various MAPS campaigns, CAPS will operate at data rates between 4 kbps and 16 kbps. The exceptions are solar wind/aurora campaigns, at times when the spacecraft is very far from Saturn and most probably in the solar wind. In these cases, CAPS will act as a solar wind monitor and use a specialized 2 kbps mode, which emphasizes the IBS rather than IMS ion data.

Difficulties resulting from unfavorable spacecraft orientations can be solved in several ways. When remote sensing instruments are taking data, the quality of the pointing for CAPS can be improved by selecting the secondary axis or by identifying which of several potential targets is more favorable to CAPS (e.g., observations by the remote sensing instruments of one ring ansa rather than another will frequently make the difference between good and bad pointing for CAPS.) A drawback of "riding along" in this manner is frequent turning and re-orienting of the spacecraft

TABLE XIV  
Characteristics of the saturnian tour.

L shell crossings	Number in tour	Number in MAPS campaigns
Titan ( $L = 20.25$ ) w/ $ \text{latitude}  < 30^\circ$	124	37
Enceladus ( $L = 3.94$ ) w/ $ \text{latitude}  < 30^\circ$	69	22
G ring ( $L = 2.72$ ) w/ $ \text{latitude}  < 30^\circ$	14	8
“aurora” $L = 15$ w/ $r < 5R_S$	22	13
Time in regions of the magnetosphere	Days in tour	Days in MAPS campaigns
Solar wind $r > 40 R_S$ , $0600 < LT < 1800$	277.64	107.56
Near magnetospheric boundaries $25 > r > 40 R_S$ , $0600 < LT < 1800$	313.19	195.77
Magnetotail $r > 25 R_S$ , $LT < 0600$ or $LT > 1800$	171.95	106.45
Titan Torus $10 < r < 25 R_S$ , $ \text{latitude}  < 30^\circ$	374.34	62.53
Inner magnetosphere/Icy satellite torus $3 < r < 10 R_S$ , $ \text{latitude}  < 30^\circ$	79.64	16.06
Inner magnetospher/ring ionosphere $r < 3 R_S$ , $ \text{latitude}  < 30^\circ$	1.67	0.95
Polar/auroral regions $r < 5 R_S$ , $L > 10 R_S$	2.49	1.61

as remote sensing instruments observe different targets. This will complicate data analysis, but we do not expect it to affect data quality. When riding along with remote sensing observations is not possible, CAPS will occasionally act as the prime instrument and control spacecraft orientation. These periods will be spent either at a fixed and favorable orientation, or, around apoapsis periods, rolling the spacecraft. In addition, the spacecraft will spend an average of 9 h per day downlinking data to Earth. During these periods, the spacecraft will typically roll so that the CAPS sensors and other particle instruments can observe nearly  $4\pi$  sr of velocity space. Since these rolls have a  $\sim 30$ -min period, they are not desirable when plasma conditions are likely to change rapidly. In the inner magnetosphere, such rolling downlinks will frequently be replaced with downlinks using a fixed orientation agreed upon by the particle instruments.

## 8.2. OPERATING MODES

Depending on mission phase and spacecraft power resources, CAPS will automatically go to one of two low-power states that operate out of PROM from which it can be commanded into one of three other states that operate out of software loaded from the ground or from the SSR. These states are discussed in Section 7.3.2. In only one of these (normal science) is CAPS able to acquire scientific data. In the sleep state, detector and ESA voltages are set to zero and the  $\pm 14.56$  kV

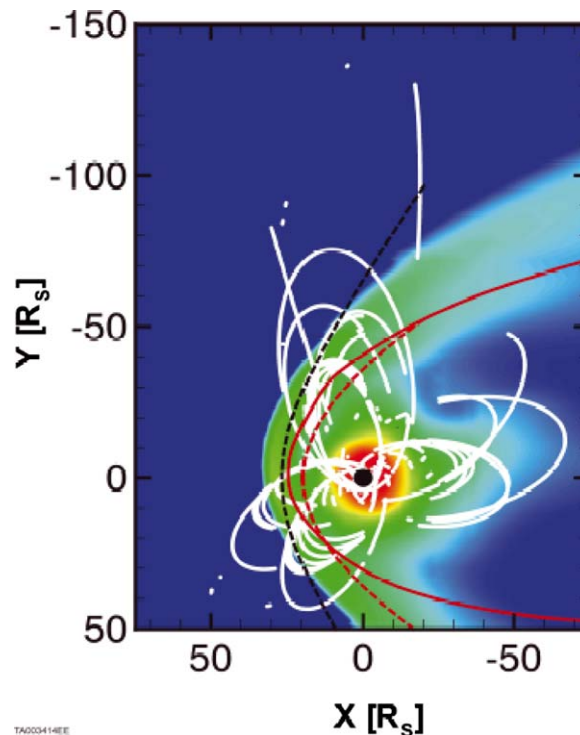


Figure 44. Cassini spacecraft trajectories corresponding to MAPS campaign periods during tour. The trajectory is overlaid on the results of a MHD simulation (Hansen, 2001) and model magnetospheric boundaries. Colors show density predicted by the MHD simulation, and the solid red line shows the magnetopause in this model. Dashed black and red lines show a Voyager-based model bow shock and magnetopause, respectively (Slaven *et al.*, 1983.)

voltages lowered to some safe value. The IBS and ELS sensors can be brought out of this state rather rapidly ( $\sim 15$  min). The IMS requires  $\sim 2$  h. None of the other CAPS states incorporate high-voltage operations, nor can they generate science data (see Table XIII for operational modes). All spacecraft operating modes currently planned for tour allow CAPS to remain on and operating. Use of the CAPS sleep mode is expected to be limited to activities associated with Saturn orbit insertion and the Huygens probe mission.

Within the normal science state CAPS is capable of performing a wide range of table-driven programs devoted to science data gathering. As part of the science planning process, observational modes are specified that control the range of velocity space covered by the sensors, the rate at which velocity space is scanned, the conditions under which IMS data will be taken, and the data products to be returned from the three sensors. Voltage tables that control each sensor's ESA, as well as the range of ACT angles to be scanned, can be independently programmed thus controlling the ranges of velocity space covered by CAPS.

The three ELS voltage tables mentioned earlier are fixed. Those of IBS and IMS consist of 512 and 64 entries respectively that can be filled with step values corresponding to a desired voltage scan. As explained earlier, the step values for IBS and IMS may be chosen from among 12,288 micro-steps corresponding to digital to analog converter resolution. Thus it is possible to create tables corresponding to logarithmic, linear, or any other placement of steps within the allowed voltage range of the ESA high-voltage supplies. The time resolution and therefore the stepping interval for each sensor is different (Table I) and tied to the IMS sampling rate of 62.50 ms.

The default energy table for ELS, which controls the sweep generator in 16% decrements, covers 63 steps from 0.6 eV to 28.25 keV. For IMS, the default will be 63 steps from 1 to 50 keV in 16% decrements, while IBS will use a variety of mode-dependent energy tables. In solar wind search mode, IBS will sweep from 150 eV to 10 keV in 255, 1.67% steps. When the instrument identifies the proton peak, IBS will shift to a solar wind tracking mode. In this mode, IBS sweeps 127, 1.67% steps every second over an energy range that extends from one half to three times the energy of the proton peak. This range is adjusted every 256 s, on the basis of the previous 256 s of data. If the proton peak shifts outside the observed range, or if a change in spacecraft attitude obscures the solar wind, IBS will return to solar wind search mode. In magnetospheric scan mode, IBS will use two interleaved, 255-step sweeps, from 10 eV to 50 keV in 3.37% steps. The interleaved sweeps can be combined on the ground to give 1.67% energy resolution at a lower-time resolution. Custom, 255 step sweep tables will be used during close satellite encounters.

The range of actuator motion will be a compromise between time resolution and angular coverage. Sweeping through 180° (close to the maximum range) requires approximately 200 s, while sweeping through a 24° range takes only 48 s. The actuator may also be held at a constant position, producing a two-dimensional cut of velocity space at the 2- or 4-s energy sweep period of the sensors. This is the planned mode of operation during icy satellite encounters, which are very rapid (e.g., during an Enceladus encounter, the spacecraft crosses the satellite's geometric wake in under 50 s.)

Another important operational consideration is selecting the seven ion species reported by SAM. The SAM extracts spectra of up to 32 atomic species, of which up to seven are reported and returned in the CAPS data. Each ion group table contains 16 possible, 7-species combinations. Selection of ion species will be based on analysis of, and experience with, the IMS data, particularly the abundance of species indicated by B-cycle TOF data. The initial selections early in the mission will be based on theoretical models and earlier Voyager measurements. In addition, multiple group tables can be stored in the spacecraft SSR and loaded into SAM. This would allow group tables customized to different parts of Saturn's magnetosphere to be used without the need for uplinking new data tables.

The mix of data products placed in the telemetry stream by CAPS is determined by telemetry rate and is discussed in detail in the next section. Solid-state recorder

memory on the spacecraft will be allocated on a day-by-day basis based on the detailed Cassini science plan. Depending on the CAPS allocation and particular measurement objectives during the day, one or more data rates and their duration are chosen to produce the required volume.

In addition to the normal science mode, CAPS has an engineering mode in which multiplier gains are checked, pulser stimulation signals are used to test and calibrate detector signal chains, and detector background is measured for an extended period. Before reaching Saturn the engineering mode will be operated as frequently as cruise data volume and pointing restrictions allow. After reaching Saturn this mode will be part of a periodic instrument calibration occurring approximately once every 50 days.

### 8.3. DATA PRODUCTS

At the maximum CAPS telemetry rate of 16 kbits/s all data products coming out of the science and calibration modes can be accommodated without the need for compression. The exception is the compressed extraction of ions by the SAM algorithm, and a semi-logarithmic collapse of all data words. The collapse replaces 16-bit data words stored in the DPU with 8-bit data words to be returned to Earth. For small data numbers, the 8-bit values are equal to the 16-bit values, but for higher values the scale is logarithmic. A similar 32- to 16-bit compression is used for TOF data. As a result of this compression, the uncertainty in the higher data numbers is roughly  $\pm 0.015N$  rather than the statistical  $\pm N^{1/2}$ . No attempt was made to carry out more exotic on-board compression routines such as moment calculations or image-like compressions, with the exception of a run-length compression of the sparse, IBS data.

The contents of the CAPS data products at 16 kbits/s are distributed among the three sensors, the ACT and housekeeping channels as shown in Table XV. Data products are organized along A-cycle (32.0 s) boundaries. Acquisition and formation of B-cycle data products is more complex than the A-cycle process: The CPU2 extracts TOF data in the form of 512 channels each of ST and LEF data. In the default mode, adjacent energy steps are sampled to produce  $2RES \times 32E \times 512TOF = 32,768$  words. In the standard CAPS telemetry mode of 16 kbits/s, each word of B-cycle data is summed over 8 A-cycles, whereas for some lower rate modes it is summed over 16 A-cycles (i.e., the B-cycle is 8 A-cycles long for the 16 kbits/s mode and 16 A-cycles long for these other modes).

Most CAPS data products are generated at lower data rates by collapsing (summing) the 16 kbps data over adjacent energy, elevation and/or azimuth bins. In addition, snapshots (uncollapsed subsets of the 16 kbps data) may be included. The subset of data included in the snapshot can be determined on the spacecraft, so that the snapshot contains the peak of the velocity distribution. Leaving out certain products entirely produces the smallest possible datasets. The modes used by the CAPS

TABLE XV  
Telemetry products in 16 kbits/s mode.

Product	Data channels						Total* bytes
	EQ	EL	AZ	MQ	LOG	TOF	
ELS	63	8	16	–	–	–	8068
IBS	255	3	16	–	–	–	12244
IMS ION	63	8	8	7	–	–	28288
IMS TDC LOG	63	–	8	–	4	–	2020
IMS TDC SNG	63	8	8	–	–	–	4036
IMS TOF LEF	32	–	–	–	–	512	16388
IMS TOF ST	32	–	–	–	–	512	16388
ACT	–	–	–	–	–	–	68
HOUSEKEEP	–	–	–	–	–	–	170

\*Totals for each product include 4 bytes of fiducial information.

Acronyms: EQ: energy/charge, MQ: mass/charge, EL: elevation, LOG: logical, AZ: Azimuth, TOF: time-of-flight.

instrument were revised prior to the Cassini Jupiter encounter to include 0.25, 0.5, and 1 kbps rates, in addition to the original 2 and 16 kbps modes. These modes were further revised before reaching Saturn, to add 4 and 8 kbps modes and incorporate experience from analysis of the Jupiter data. Other data products that can be included as options (at the expense of sensor data) are memory readout of control tables for SAM and ESA stepping. Sequential event data that are used to verify IMS operations can also be included.

#### 8.4. GROUND OPERATIONS

In an attempt to reduce overall mission costs, the Cassini project has embraced the concept of distributed ground operations. For so-called principal investigator (PI) instruments this means that responsibility for instrument commanding and health and safety lies with the instrument teams and, in particular, with the PI institution. As a practical matter, the PI institution becomes an extension of the Cassini project ground system.

Ground system operations can be divided into two categories: Generating commands for uplink to the spacecraft and handling and processing data produced by the spacecraft during downlink.

Ground operations begin with a sequence-by-sequence list of measurement objectives developed by drawing on the Cassini science operations plan (SOP) and elaborations of the CAPS science objectives. The SOP describes spacecraft orbit, attitude, and allocation of resources such as power, pointing constraints, and

telemetry. This plan was developed prior to reaching Saturn, and consists of conflict-free, flyable sequences. Later, if no significant changes are required, sequences will be taken from the SOP, updated, re-checked and sent to the spacecraft. For CAPS, the most important part of updating these sequences will be the revision or insertion of instrument-internal modes. This is the stage where experience from previous observations can be used to improve our choices of actuation angles, ion selection index, etc. In practice, significant changes to the SOP are likely. Unexpected events, such as satellite ephemeris changes or downlinks that cannot be scheduled at exactly the planned time, will force some changes and modification of the sequences. Changes in response to new discoveries will be highly desirable. The substantial effort required to develop the SOP prior to reaching Saturn is intended to allow for these changes. With flyable sequences in hand, the instrument teams can focus their efforts on science and on implementing desired changes.

Downlink processing begins when science and housekeeping data from CAPS, together with auxiliary data (spacecraft ephemeris, attitude, etc.), are extracted from the Cassini project data-base through the CAPS science operations and planning computer (SOPC) located at SwRI. Level 0 housekeeping data are immediately examined for any out-of-limit values that might affect CAPS health and safety. In the event that limits are exceeded, a contingency plan provides options for recovery from the fault. Non-emergency conditions that may require adjustments to system operating parameters will be incorporated in the normal command uplink cycle. Real-time operations can also be accommodated through the project's sequence virtual team (SVT) process. If necessary, emergency operations can be invoked in which commands will be sent to CAPS in real time. This same routine also checks the predicted against the actual instrument state vector to verify proper operation. Level 0 science data are also checked for trends that might indicate unanticipated changes in sensor operation such as shifts in detector gain or the appearance of unexpected sources of detector background.

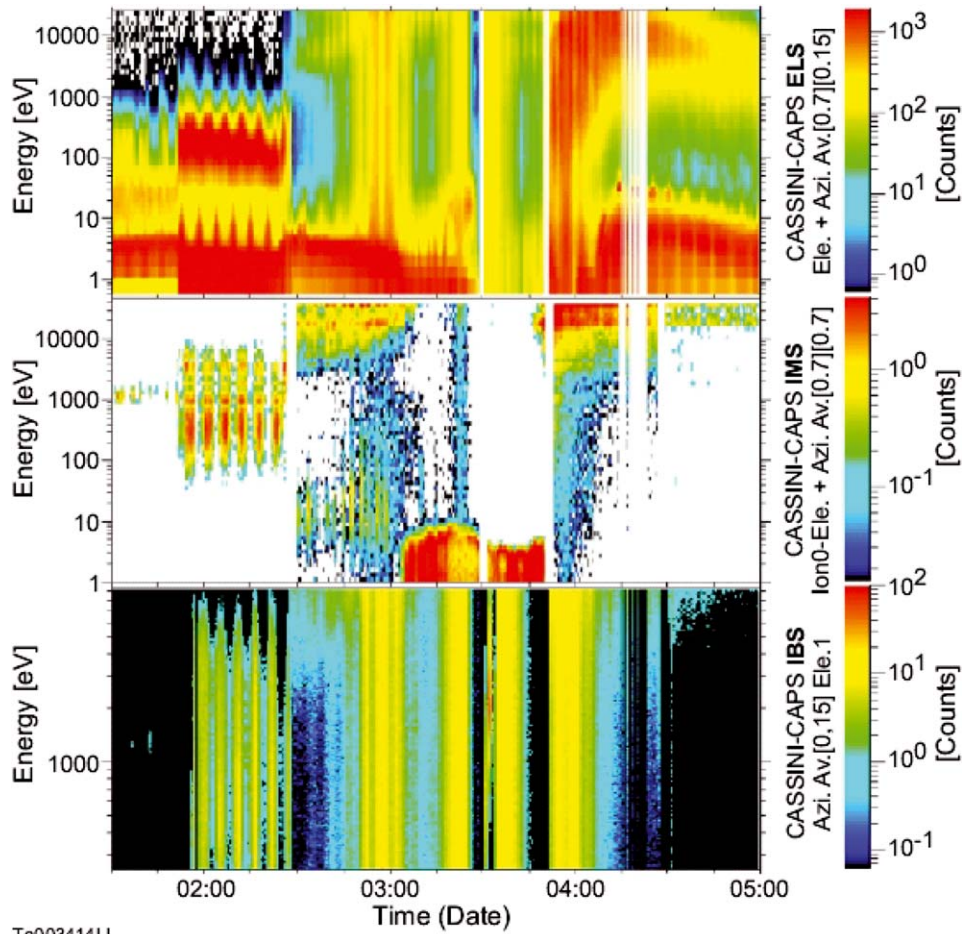
In tandem with the ongoing limit checking process, level 0 data are decompressed, checked for quality, and formatted to create the CAPS level 1 products. Auxiliary data are collected into a parallel stream with the same file structure so that the two are compatible. Level 1a data are extracted and then converted to physical units, such as flux and velocity space density, which then constitute level 1b products. Finally, the derived level 2 data products, such as density, flow velocity and temperature are calculated. These data, together with the software tools needed to generate data displays, are then made available to the CAPS and Cassini teams. The interface with the data analysis system will be Web-based to maximize accessibility and opportunities for scientific study of the data. This interface allows wide access to a set of production survey tools, including various types of spectrograms and line plots, as well as orbit analysis tools. Survey plots (spectrograms and line plots) will be routinely produced as image files and stored on-line for rapid sequential and random access to facilitate browsing, surveys and comparisons with other Cassini observations.

## 9. Initial Operations and Performance

### 9.1. CAPS INITIAL RESULTS DURING EARTH FLYBY

On August 18, 1999 the Cassini spacecraft flew past the Earth on its way to Saturn. While the purpose of the encounter with Earth was to gain velocity, it also opened the possibility for operation of the CAPS as calibration and test exercises. As Rymer *et al.* (2001) have described, the encounter pointing geometry had the spacecraft -Z-axis pointed toward the sun. In this orientation the center of the three sensors' elevation FOVs pointed orthogonal to the direction of motion. The fans (Figures 3 and 6) viewed forward (sunwards) as well as in the spacecraft direction of motion (i.e., the spacecraft ram direction). The latter proved favorable for viewing low-energy plasmas in the Earth's magnetosphere (a situation similar to what occurred during orbit insertion at Saturn). Although it is anticipated that the solar wind will be less intense at Saturn ( $n_{SW} \sim R^{-2}$  where  $R$  is distance from the sun), other features inside the bow shock and magnetopause should be of broadly similar intensity. Thus Earth encounter presented a unique opportunity to test CAPS performance in a not too dissimilar environment from that of Saturn.

In Figure 45 we present energy-time spectrograms from all three CAPS sensors. The ordinate is particle energy, the abscissa is in units of hours UT, and color corresponds to detector counting rates. The upper panel corresponds to ELS data, the middle to IMS, and the lower to IBS. Cassini sliced through the near-equatorial magnetosphere near the sub-solar point. The encounter itself was unique in that the spacecraft speed of 16.1 km/s was about three times that of comparable orbiting spacecraft. With reference to Figure 45, at 0000 UT ELS and IMS measurements indicate that the spacecraft is clearly in the solar wind. At 0151 UT ELS shows most clearly and with the best time resolution that Cassini crosses the Earth's bowshock and passes into the magnetosheath (note the rapid increase in electron flux and the vertical barred pattern due to the motion of the CAPS actuator, indicating strong plasma flow in the magnetosheath). At 0225 UT Cassini crossed the magnetopause into the Earth's magnetosphere proper (sharp drops in electron and ion fluxes). Vertical yellow bars at  $\sim 0250$  to  $0300$  are caused by penetrating particles from the Earth's radiation belts that enter the ELS and IBS detectors. IMS data require coincidences between the two detectors, which greatly reduced its background rates. From 0306 to 0351 the spacecraft was in the plasmasphere. What the figure shows is relatively cold ( $\sim$ few eV) plasma rammed into the ELS and IMS sensors when the spacecraft was inside the plasmasphere (red area below 10 eV from 0306 to 0351 UT) on the inbound and outbound trajectories. Because the IBS is set at a higher energy range, corresponding to solar wind proton energies  $> 200$  eV, it does not observe the plasmasphere. It is worth noting that the plasmasphere is similar in terms of density and temperature to the outer portion of Titan's ionosphere. Finally, the horizontal red bands in the IMS plot between approximately 0230 to 0310 UT and between 0345 to 0440 UT represent the Earth's ring current.



Ta003414LL

Figure 45. Composite energy-time spectrograms of ELS (upper panel), IMS (middle), and IBS (lower) taken during the Cassini Earth encounter. The color scale at the right is proportional to detector counting rates.

## 9.2. ELS INITIAL RESULTS

Abel *et al.* (2001) and Rymer *et al.* (2001) give an overview and detailed discussion of ELS measurements at Earth. Figure 46 is an energy–time spectrogram of ELS data in the same format as Figure 45 except that the eight separate panels correspond to eight anodes and therefore to eight elevation directions (see Figure 10a, b). These data illustrate the high quality of ELS performance in all regions traversed by Cassini. More detailed analysis of bi-directional lobe electrons, including the first observation of a returning electron population in the magnetosheath, is described in Abel *et al.* (2001). Careful examination of Figure 46 shows many of the distributions

to be anisotropic (e.g., in the magnetosheath between  $\sim 0200$  and  $0240$  UT, or the plasmasphere near  $0315$  UT).

Initial analysis of measurements taken at Jupiter indicates high-quality data associated with the jovian bow shock, magnetosheath and magnetopause. In addition, ELS has monitored the effects of impulsive solar activity in the distant solar wind beyond 5 AU (from September 2000 onwards).

Data in Figure 46 also show that at low energies ( $E < 30$  eV) ELS measurements are strongly affected by asymmetries in the spacecraft photoelectron sheath and, at Earth at least, by Cassini's high velocity ( $16.1$  km/s) relative to the plasma (Rymer

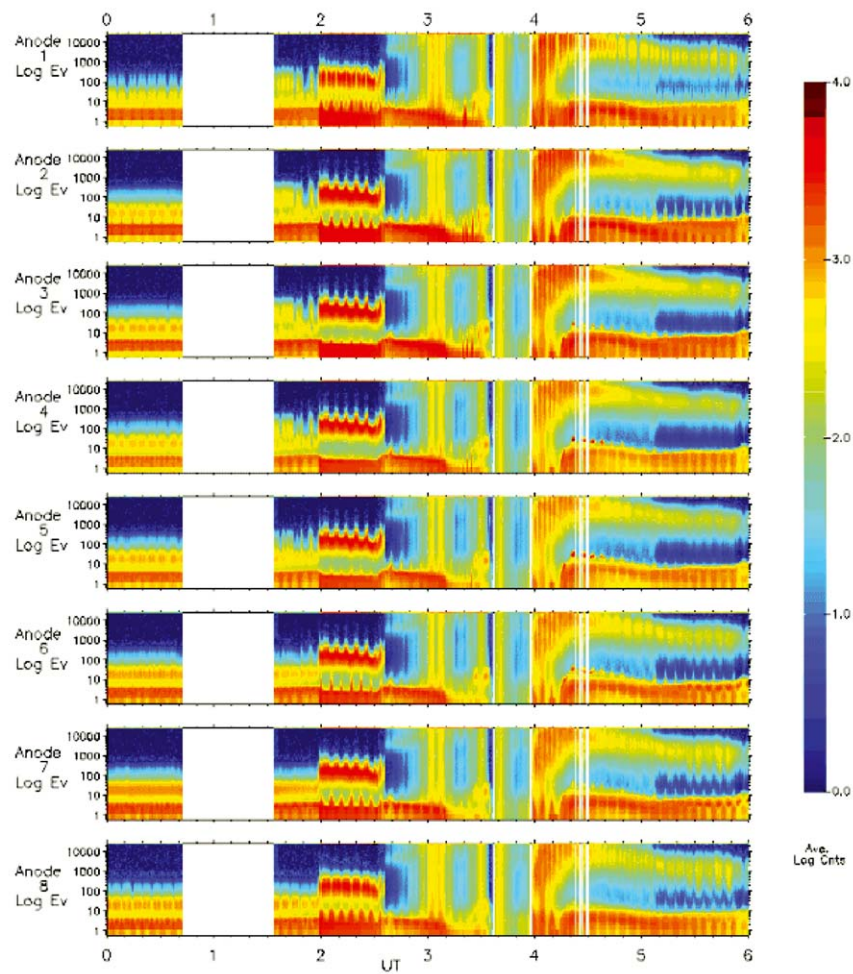


*Figure 46.* ELS energy-time spectrograms taken on August 18, 1999 during Cassini's flyby of the Earth. The eight separate plots represent the eight ELS elevation anodes, with anode eight looking closest to the direction of the spacecraft  $-Z$ -axis (i.e., toward the spacecraft antenna).

*et al.* (2001). At Titan although the spacecraft velocity is lower ( $\sim 6$  km/s) so are ambient electron thermal velocities. Thus we may expect an anisotropic sheath. Although photoelectron emission from the spacecraft is diminished by  $R^{-2}$  relative to that at Earth it is also expected to add to asymmetries. In other words, it is difficult to predict what the response of ELS will be during Titan encounters, although the one data point from Earth is a start for predicting that behavior.

### 9.3. IBS INITIAL RESULTS

Because of its design, IBS data from the Earth encounter are less useful than those of the other two sensors. This can be understood with reference to the IBS section of this paper, but basically it is caused by the orientation of its FOV perpendicular to the ram flux coupled with the lack of resolution in the ram direction. On the other hand, during the Cassini encounter with Jupiter, when the sensors could be pointed toward the solar direction, its performance could be demonstrated.

Figure 47 is an example of one of  $\sim 40$  bow shock crossings observed during encounters in late 2000/early 2001 (Szego *et al.*, 2003a, b) by IBS and the other CAPS sensors. In Figure 47 the jovian bow shock was crossed between 0430  $\sim$  0500 UT when Cassini was  $576R_J$  ( $\sim 4.1 \times 10^7$  km) from Jupiter. Protons in the solar wind upstream of the shock can be distinguished as a red band before 0430 UT. Above it is a thinner yellow band representing  $\text{He}^{++}$ . The shock crossing can be identified by the increase in ion temperature downstream. Comparison with magnetic field data indicates a parallel shock typical of turbulent shocks seen in the jovian magnetosheath. At various times after the shock the solar wind plasma temperature drops such that IBS is again able to resolve the  $\text{He}^{2+}$  peak. Data presented in Szego *et al.* (2003) dealing with the jovian bow shock and magnetosheath show convincingly that IBS is operating as anticipated.

### 9.4. IMS INITIAL RESULTS

Figure 48 shows IMS data in energy versus TOF spectrogram format integrated over the month of March 2002 when Cassini was roughly 8 AU from the sun. The data represent the first observations of interstellar pickup ions made beyond 5 AU. Pickup ions originate from neutral gas in the interstellar medium (Gloeckler and Geiss, 1998). The pickup process occurs when gas is ionized by solar photons and accelerated by the solar wind electromagnetic field to energies as high as  $2Mv^2\sin^2\alpha$  where  $v$  is the solar wind bulk velocity and  $\alpha$  is the ion pitch angle. Interstellar ions have higher energies than solar wind ions as well as pitch angle distributions with particles arriving at angles other than the solar wind direction. Thus they effectively avoid the high-gain antenna of the spacecraft that prevents IMS from directly viewing the solar wind. In summary we would expect

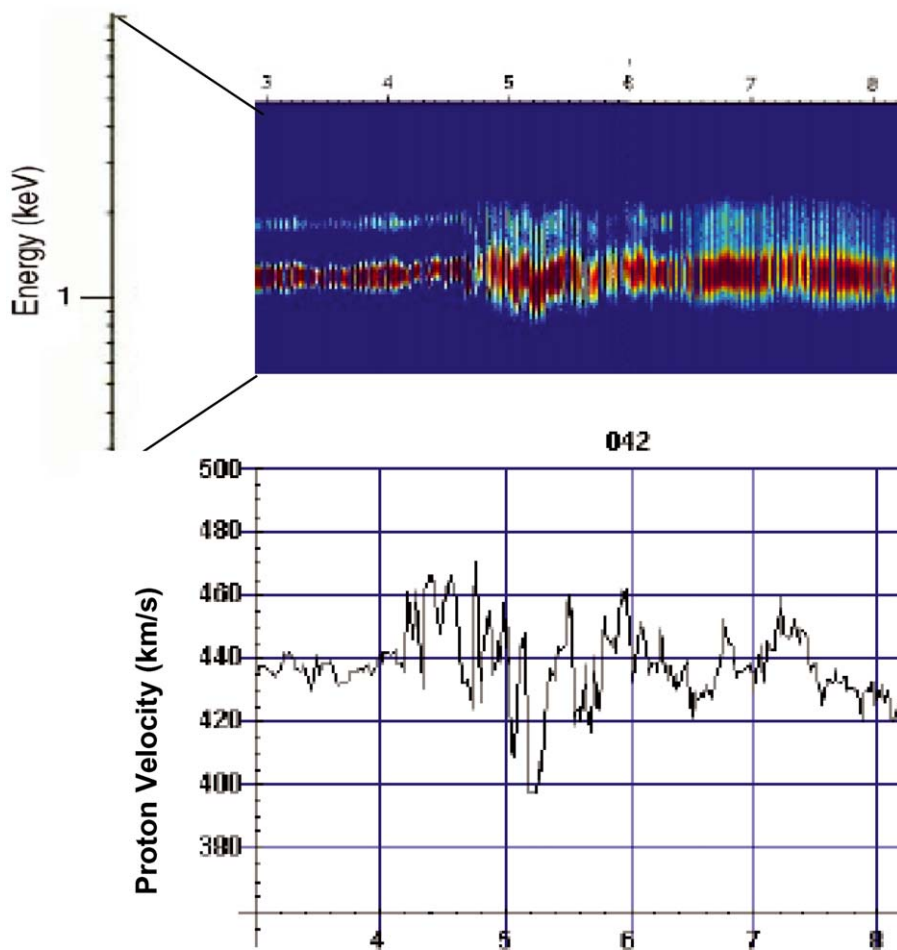
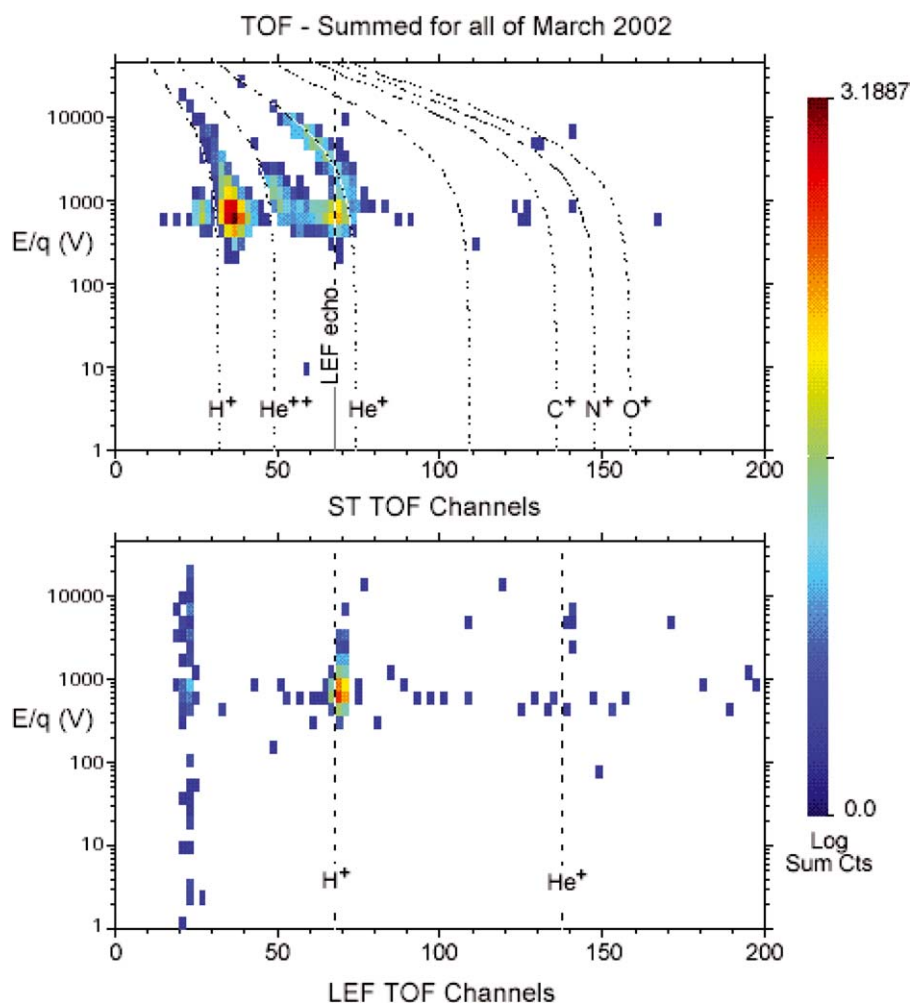


Figure 47. Upper panel shows energy–time spectrogram for the IBS taken between 0300 to 0900 UT on February 11, 2001. The energy scale covers 0.25 to 10.0 keV. The lower panel is a plot of solar wind proton velocity in km/s same period (from Szego *et al.*, 2003a).

to see ions arriving from directions unblocked by the HGA up to a cutoff energy of  $2Mv^2\sin^2\alpha$ . Complicating the picture is the fact that during March 2002 the spacecraft turned in such a way that there is some direct solar wind data mixed with data in Figure 48.

In the ST energy spectrum in Figure 48  $H^+$  ranges up to 20 keV while the bulk of the distribution is at  $\sim 1$  keV corresponding to  $\sim 440$  km/s, roughly the average solar wind velocity. The highest  $H^+$  energy (20 keV) suggests a maximum solar wind velocity during this period of 980 km/s, which is a high but still reasonable value. The second most intense peak in the ST spectrum, labeled LEF echo originates not



*Figure 48.* Color-coded logarithm of the sums of counts in the CAPS IMS ST (upper panel) and LEF (lower panel) detectors, respectively. The dashed lines are derived from a simple theoretical model of the instrument. Data are summed over all of March 2002. The summed counts are displayed as a function of energy-per-charge (vertical axes) and time-of-flight channel on the horizontal axis (1 channel = 3.125 ns).

from the nearby  $\text{He}^+$  counts, but rather from an “echo” peak caused by  $\text{H}^+$  ions (see discussion in Section 6.7 and Figure 38b).

The other two ions visible easily in the ST spectrum, in addition to  $\text{H}^+$ , originate from  $\text{He}^{++}$  and  $\text{He}^+$  listed in order of TOF (see Equations 4–6). In order to understand the ST spectra it is necessary to consider charge exchange fractions leaving the foil (see Figure 21) as well as the center of mass velocity of particles leaving the foil. Thus, on passing through a foil, the two He charge states show up

primarily as  $\text{He}^0$ . The LEF spectrum shows the  $\text{H}^+$  peak, but, as a consequence of the low rates of  $\text{He} \rightarrow \text{He}^+$  and  $\text{He} \rightarrow \text{He}^{++}$ , there are very few counts. We do expect, however, that by summing over longer periods of time and removing unwanted “background” that occurs when Cassini puts the IMS FOV in the solar wind direction, we will be able to distinguish and observe interstellar pickup ions.

Using data from the IMS McComas *et al.* (2004) have reported the first observations of interstellar pickup ions made beyond the orbit of Jupiter. The spatial distribution of the ion fluxes is consistent with gravitational focusing by the Sun. During the period reported, Cassini was located between 6.4 and 8.2 AU from the Sun in the downstream direction relative to incoming interstellar gas moving past the Sun. The IMS data also establish the existence of a hydrogen shadow in this same region where hydrogen is depleted relative to interstellar flow. A combination of radiation pressure on the hydrogen atoms together with trajectories passing close to the Sun that lead to photoionization and loss in the solar wind leads to the shadowing effect. We anticipate further observations of interstellar pickup ions as the spacecraft approaches Saturn and throughout the orbital mission when a large amount of time is spent in the solar wind (Table XIV).

## 10. Conclusions

After nearly 7 years in flight, Cassini went into orbit around Saturn on July 1, 2004. During the cruise to Saturn the CAPS instrument was operated successfully for periods of varying length during cruise and the Earth and Jupiter encounters. The long cruise period has given our team the time necessary to fully check out and test CAPS in the plasma environments of the solar wind and two magnetospheres. This gives us confidence that the instrument will perform successfully during the saturnian tour. In addition, the cruise period was used to develop a sophisticated ground system that enables and greatly assists the complex task of science planning for CAPS activities throughout the mission. The downlink portion of the ground system is equipped to reduce data rapidly once it is received on the ground and make it available as quickly as possible to the scientific community.

## Acknowledgments

Initial development of the CAPS instrument began in 1989. During the intervening years design, fabrication, testing and calibration, as well as post-launch science planning and operations has been a collaborative effort involving the following institutions: Southwest Research Institute (overall responsibility for the investigation, system design, low voltage supplies, spacecraft and sensor interface boards, IBS and IMS high-voltage supplies, flight and ground system software, system calibration, flight operations, science planning lead), the Los Alamos National Laboratory (IMS sensor concept, design, integration, and calibration; IMS detectors, front

end electronics, and time-to-digital converter; IBS concept, detectors, integration, and calibration, flight data processing), the Centre d'étude des Environnements Terrestre et Planétaires (IMS sensor mechanical design and fabrication, SAGEM motor for the actuator), the Goddard Space Flight Center (IMS high-voltage supplies, spectrum analyzer module hardware and software, and CPU2 software), the Jet Propulsion Laboratory (IMS calibration), the University College London (ELS concept, design, sensor fabrication, integration, and calibration, flight data processing), the University of Oulu (IBS optical design and analysis), the University of Virginia (IMS-related carbon foil characterization), the VTT Automation (IBS sensor mechanical design and fabrication, actuator subsystem design, fabrication, and test), the KFKI Research Institute for Particle and Nuclear Physics (electrical ground support equipment (EGSE) and EGSE software) the Norwegian Defense Research Establishment (ELS sensor management unit), and the Rutherford Appleton Laboratory (ELS high-voltage power supplies, electrical system, and detectors).

Many people at these and other institutions have given their best ideas and efforts to support CAPS development and we wish to thank them individually here:

At SwRI we particularly wish to thank M. Ahr, J. Alexander, S. Archey, N. Brinkmeyer, D. Burket, B. Gahagan, D. Guerrero, B. Gupta, D. LeBlanc, J. Ling, M. McGinnis, B. McLaren, G. Palacios, A. Ramirez, L. Roberson, S. Rogillio, M. Sattler, N. Sawka, T. Sawka, D. Strain, R. Thorpe, V. Torres, C. Urdiales, J. H. Waite, Jr. and R. Welch.

At LANL we particularly wish to thank D. Archuleta, J. Baldonado, S. Bame, P. Barker, R. Bramlett, D. Burr, P. Campbell, M. Dugan, R. Edwards, J. Elliot, D. Everett, K. Fuller, H. Funsten, I. Gonzales, V. Herrera, D. Laurence, I. Medina, E. Michel, K. Olivas, N. Olivas, P. Pazuchanics, D. Potter, R. Pressini, A. Roybal, P. Salazar, M. Shappirio, G. Smith, S. Storms, D. Suszcynsky, A. Ulibarri, M. Vigil, R. Vigil and V. Vigil.

At GSFC we particularly wish to thank C. Clatterbuck, D. Glenn, F. Hunsaker, W. Mish, K. Ogilvie, R. Vondrak, A. Williams, and K. Young.

At CETP we particularly wish to acknowledge the work of F. Leblanc, F. LeGoff, A. Ruatti and the ETEZ Company.

The ELS team leader, A. J. Coates, acknowledges the support of the Royal Society. We would like also to acknowledge the support of the rest of the ELS team including G. Abel, C. Alsop, T. Barsby, S. Burge, J. Coker, N. Flowers, L. Free, L. Gilbert, J. Godfrey, B. Hancock, J. Holmes, C. Jackman, A. Johnstone, D. Kelsh, P. Kendon, T. Murrell, J. Raymont, D. Reading, A. Rymer, J. Rose, P. Sheather, F. Thurlow, and L. Worth. Morgan-Matroc Limited, Rugby, U.K. supplied ELS anodes. ELS MCPs were supplied by Philips Components Ltd., France.

The IBS Collaborators would like to thank P. Kyrenius, T. Korpela, S. Kuitunen and J. Vidquist of VTT Automation.

The CAPS-EGSE was developed at KFKI-RMKI and we particularly wish to acknowledge the contributions of L. Foldy and I. Gladkih.

Work at the University of Virginia supported in part by NASA's Planetary Geology and Geophysics program.

The CAPS actuator (ACT) was developed and manufactured by the VTT under contract to SwRI. We particularly wish to thank members of the laboratory and workshops of VTT Automation: T. Antila, H. Berg, the personnel of the Fine-Mechanical Prototype Shop, and especially K. Siitari of Rejlers Inc. The ACT stepper motor was manufactured by SAGEM of France and provided by CETP. Starsys Research Inc., of Boulder, CO manufactured the wax thermal actuators and the IMS cover mechanism.

We wish to acknowledge the primary support for CAPS development and operations in the U.S. provided by NASA/Cal Tech/JPL through JPL contracts 958964, 959401, 959930, and 1243218 to the SwRI, and by JPL contract 1210586 to the University of Michigan. Initial R & D funding was made available by the Advisory Committee for Research at SwRI, and by the Department of Energy at Los Alamos National Laboratory. Work at CETP was supported by CNES grants 92/204 and 95/04; in Hungary by OMF-07851 and a Hungarian Space Office grant MUI/TP/47; in Finland early development work on the ACT was supported by internal VTT funding, with further support provided by the Academy of Finland and the Ministry of Trade and Industry of Finland; in the U.K. by the Particle Physics and Astronomy Research Council; and in Norway by the Norwegian Defense Research Establishment and the Research Council of Norway.

### Appendix: List of Acronyms

---

ACT	Actuator
ADC	Analog-to-Digital Converter
ALF	Assisted Load Format
amu/e	Atomic Mass Unit/Charge
AU	Astronomical Unit
AZ	Azimuth
BIU	Bus Interface Unit
CAPS	Cassini Plasma Spectrometer
CDS	Command and Data System
CEM	Channel Electron Multiplier
CH	TOF channel number (1 CH = 3.125 ns)
CPU	Central Processing Unit
DPU	Data Processing Unit
DAC	Digital-to-Analog Converter
E	Energy, energy step

*(Continued on next page)*

EL	Elevation
ELS	Electron Spectrometer
EPS	Energetic Particle Spectrometer (Voyager)
E/Q	Energy/Charge
ESA	Electrostatic Analyzer
FEE	Front End Electronics
FIFO	First-In-First-Out buffer
FOV	Field-of-View
FPP	Fields and Particles Pallet
FWHM	Full Width at Half Maximum
Gbits	Gigabits ( $10^9$ bits)
HEEA	High-Energy Electron Analyzer (Cluster)
HVU	High-Voltage Unit
IBS	Ion Beam Spectrometer
ID	Identification bit
IEB	Instrument Expanded Block
IMS	Ion Mass Spectrometer
INMS	Ion Neutral Mass Spectrometer
kV	Kilo <u>V</u> olt
keV	Kilo <u>e</u> lectron <u>V</u> olt
LEF	Linear Electric Field
LEMMS	Low Energy Magnetosphere Measurement System
LUT	Look-Up Table
MCP	Microchannel Plate
MIMI	Magnetospheric Imaging Investigation
MLI	Multi-layer Insulation
M/Q	Mass/charge
ms	Milliseconds
MSSL	Mullard Space Science Laboratory
ORS	Optical and remote sensing instruments
PEACE	Cluster Plasma Electron and Current Experiment
PI	Principal investigator
PLS	Plasma Science (Voyager)
PROM	Programmable Read-Only Memory
RAM	Random Access Memory
RES	Resolution (# of TOF channels: 512, 1024, 1536, 2048)
RTI	Real Time Interrupt
SAM	Spectrum Analyzer Module
SMU	Signal Management Unit
SOI	Saturn Orbit Insertion
SOP	Science Operations Plan

*(Continued on next page)*

SOPC	Science Operations and Planning Computer
SSR	Solid State Recorder
ST	Straight-Through (time-of-flight)
SwRI	Southwest Research Institute
SVT	Sequence Virtual Team
TDC	Time-to-Digital Converter
TOF	Time-of-Flight
1-D	1-Dimensional
2-D	2-Dimensional
3-D	3-Dimensional

---

### References

- Abel, G. A., Coates, A. J., Rymer, A. M., Linder, D. R., Thomsen, M. F., Young D. T., and Dougherty, M. K.: 2001, *J. Geophys. Res.* **106**, 30199.
- Alsop C., Free, L., and Scott, S.: 1998, in R. F. Pfaff, J. E. Borovsky, and D. T. Young (eds.), *Measurement Techniques in Space Plasmas: Particles*, AGU Geophysics Monograph Series, Vol. 102, pp. 269–274.
- Alton, G. D.: 1993 *Nucl. Instrum. Methods Phys. Res.* **B73**, 221–288.
- Bame, S. J., Asbridge, J. R., Felthausen, H. E., *et al.*: 1978, *IEEE Trans. Geosci. Electron.* **GE-16**, 216.
- Behannon, K. W., Lepping, R. P., and Ness, N. F.: 1983, *J. Geophys. Res.* **88**, 8791.
- Bird, M. K., Dutta-Roy, R., Asmar, S., Rebold, T. A.: 1997, *Icarus* **130**, 426.
- Blanc, M., *et al.*: 2004, *Space Sci. Rev.*, **114**, 1–112.
- Brecht, H. S., Luhmann, J. G., and Larson, D. J.: 2000, *J. Geophys. Res.* **105**, 13119.
- Bridge, H. S., *et al.*, *Space Sci. Rev.* **21**, 259.
- Bridge, H. S., Belcher, J. W., Lazarus, A. J., Olbert, S., Sullivan, J. D. Bagenal, F., Gazis, P. R., Hartle, R. E., Ogilvie, K. W., Scudder, J. D., Sittler Jr., E. C., Eviatar, A., Siscoe, G. L., Goertz, C. K., and Vasyliunas, V. M.: 1981, *Science*, **212**, 217.
- Broadfoot, A. L., Sandel, B. R., Shemansky, B. E., *et al.*: 1981, *Science* **212**, 206.
- Burns, J. A., and Matthews, M. S.: 1986, *Satellites*, U. Arizona Press, Tucson.
- Carlson C. W., Curtis, D. W., Paschmann, G., and Michael, W.: 1983, *Adv. Space Res.* **2**, 67.
- Coates A. J., Alsop C., Coker A. J., Linder, D. R., Johnstone, A. D., Woodliffe, R. D., Grande, M., Preece, A., Burge, S., Hall, D. S., Narheim, B., Svenes, K., Young, D. T., Sharber, J. R., and Scherrer, J. R.: 1992, *J. British Interplanetary Soc.* **45**, 387.
- Connerney, J. E. P., and Waite, J. H.: 1984, *Nature* **312**, 136.
- Connerney, J. E. P., Acuna, M. H., and Ness, N. F.: 1983, *J. Geophys. Res.* **88**, 8779–8789.
- Crary F. J., and Bagenal F.: 2000, *J. Geophys. Res.* **105**, 25379.
- Cravens, T. E.; Lindgren, C. J., Ledvina, S. A.: 1998, *Planet. Space Sci.* **46**, 1193.
- Davis, L., Jr., and Smith, E. J.: 1990, *J. Geophys. Res.* **95**, 15257–15261.
- Delitsky, M. L., and A. L. Lane: 1997, *J. Geophys. Res.* **102**, 16385–16390.
- Desch, M. D., and Rucker, J. H.: 1983, *J. Geophys. Res.* **88**, 8999.
- Esposito, L. W. *et al.*: 2003, *Space Sci. Rev.* this volume.
- Eviatar, A., and Richardson, J. D.: 1986, *J. Geophys. Res.* **91**, 3299.
- Eviatar, A., Siscoe, G. L., Scudder, J. D., Sittler Jr., E. C., and Sullivan, J. D.: 1982, *J. Geophys. Res.* **87**, 8091.
- Funsten, H. O.: 1995, *Phys. Rev. B* **52**, R8703.

- Funsten, H. O., Barraclough, B. L., and McComas, D. J.: 1993b, *Nucl. Inst. Meth.* **B80/81**, 49–52.
- Funsten, H. O., Barraclough, B. L., and McComas, D. J.: 1994, *Nucl. Inst. Meth. Phys. Res. B* **20**, 24–28.
- Funsten, H. O., McComas, D. J., and Barraclough, B. L.: 1993a, *Optical Eng.* **32**, 3090–3095.
- Funsten, H. O., Ritzau, S. M., and Harper, R. W.: 2001, *Phys. Rev. B* **63**, 155416.
- Gloeckler, G., Balsiger, H., Bürgi, A., Bochsler, P., *et al.*: 1995, *Space Sci. Rev.* **71**, 79.
- Gloeckler, G., Cain, J., Ipavich, F. M., Tums, E. O., *et al.*: 1998, *Space Sci. Rev.* **86**, 437–539.
- Gloeckler, G., and J. Geiss: 1998, *Space Sci. Rev.* **86**, 127–159.
- Gloeckler, G., and Hsieh, K. C.: 1976, *Nucl. Inst. Meth.* **165**, 537.
- Goertz, C. K.: 1983, *Geophys. Res. Lett.* **10**, 455.
- Gorney, D. J., *et al.*: 1981, *J. Geophys. Res.* **86**, 83.
- Gosling, J. T., Asbridge, J. R., Bame, S. J., and Feldman, W. C.: 1978, *Rev. Sci. Instrum.* **49**, 1260.
- Gurnett, D., *et al.*: 2003, *Space Sci. Rev.* **114**, 395–463.
- Haff, P. K., Eviatar, A., and Siscoe, G. L.: 1983, *Icarus* **56**, 426.
- Hamilton, D. C., Gloeckler, G., Ipavich, F. M., *et al.*: 1990, *Rev. Sci. Instrum.* **61**, 3104.
- Hansen K. C.: 2001, *Ph.D. Dissertation*, Department of Atmospheric, Oceanic and Space Sciences, University of Michigan.
- Hartle, R. E., Sittler, Jr., E. C., Ogilvie, K. W., Scudder, J. D., Lazarus, A. J., and Atreya, S. K.: 1982, *J. Geophys. Res.* **87**, 1383.
- Hill, T. W.: 1979, *J. Geophys. Res.* **84**, 6554.
- Hill, T. W., Dessler, A. J., and Maher, L. J.: 1981, *J. Geophys. Res.* **86**, 9020.
- Hones, E. W., Jr.: 1979, S.-I. Akasofu (ed.), *Dynamics of the Magnetosphere*, D. Reidel, p. 545.
- Hood, L. L.: 1985, *J. Geophys. Res.* **90**, 6295.
- Horanyi, M., Burns, J. A., and Hamilton, D. P.: 1992, *Icarus* **97**, 248.
- Hovestadt, D., *et al.*: 1995, *Solar Phys.* **162**, 441.
- Huang, T. S., and Siscoe, G.: 1987, *Icarus* **70**, 366.
- Ip, W.-H.: 1984, *J. Geophys. Res.* **89**, 8843.
- Ip, W.-H.: 1990, *Astrophys. J.* **362**, 354.
- Ip, W.-H.: 1992, *Proceedings of the Symposium on Titan*, **ESA SP-338**, 243.
- Ip, W.-H.: 1995, *Icarus* **115**, 295.
- Johnson, R. E.: 1990, *Energetic Charged-Particle Interactions with Atmospheres and Surfaces*, Springer-Verlag, NY.
- Johnson, R. E.: 1994, *Space Sci. Rev.* **69**, 215–233.
- Johnson, R. E.: 1998, *Sputtering of Ices in the Solar System II*, Kluwer, Amsterdam, 1998.
- Johnson, R. E., and Jesser, W. A.: 1996, *Astrophys. J.* **480**, L79–L82.
- Johnson, R. E., Pospieszalska, M. K., Sittler Jr., E. C., Cheng, A. F., Lanzerotti, L. J., and Sieveka, E. M.: 1989, *Icarus* **77**, 311.
- Johnson, R. E., and Quickenden, T. I.: 1997, *J. Geophys. Res.* **102**, 10985–10996.
- Johnson, R. E., and Sittler Jr., E. C.: 1990, *Geophys. Res. Lett.* **17**, 1629.
- Johnstone, A. D., Alsop, C., Burge, S., Carter, P. J., Coates, A. J., Coker, A. J., Fazakerley, A. N., Grande, M., Gowen, R. A., Gurgiolo, C., Hancock, B. K., Narheim, B., Preece, A., Sheather, P. H., Winningham, J. D., and Woodliffe, R. D.: 1997, *Space Sci. Rev.* **79**, 351.
- Johnstone, A. D., Coates, A. J., Wilken, B., *et al.*: 1987, *J. Phys. E: Sci. Instrum.* 795–805.
- Jurac, S., Johnson, R. E., Richardson, J. D.: 2001, *Icarus* **149**, 384.
- Jurac, S., McGrath, M. A., Johnson, R. E., Richardson, J. D., Vasyliunas, V. M., and Eviatar, A.: 2002, *Geophys. Res. Letts.* **29**, 2172.
- Kaiser, M. L., Desch, M. D., and Connereny, J. E. P.: 1984b, *J. Geophys. Res.* **89**, 2371.
- Kaiser, M. L., Desch, D., Kurth, W. S., Lecacheux, A., Genova, F., Pederson, B. M., and Evans, D. R.: 1984a, *Saturn*, University of Arizona Press, p. 378.
- Keller, C. N., and Cravens, T. E.: 1994, *J. Geophys. Res.* **99**, 6527.

- Keller, C. N., Cravens, T. E., and Gans, L.: 1994, *J. Geophys. Res.* **99**, 6511.
- Klimas, A. J.: 1985, in B. T. Tsurutani, and E. Stone (eds.), *Collisionless Shocks in the Heliosphere: Reviews of Current Research*, AGU Geophysics Monograph Series, Vol. 35, p. 237.
- Knight, S.: 1973, *Plan. Space Sci.* **21**, 741.
- Kopp, A., and Ip, W.-H.: 2001, *J. Geophys. Res.* **106**, 8323.
- Krimigis, S. M., et al.: 2004, *Space Sci. Rev.* **21**, 329.
- Ledvina, S., and Cravens, T. E.: 1998, *Planet. Space Sci.* **46**, 1175.
- Ledvina, S., et al.: 2000, *Adv. Space Res.* **26**, 1691.
- Linder, D. R., Coates, A. J., Woodliffe, R. D., Alsop, C., Johnstone, A. D., Grande, M., Preece, A., Narheim, B., Svenes, K., and Young, D. T.: 1998, in F. Pfaff, J. E. Borovsky, and D. T. Young (eds.), *Measurement Techniques in Space Plasmas: Particles*, AGU Geophysics Monograph Series, Vol. 102, pp. 257–262.
- Lindgren, C. J., Cravens, T. E., and Ledvina, S. A.: 1997, *J. Geophys. Res.* **102**, 17395–17406.
- Luhmann, J. G., Russell, C. T., Schwingenschuh, K., and Yeroshenko, Y. E.: 1991, *J. Geophys. Res.* **96**, 11199.
- Luhmann, J. G.: 1996, *J. Geophys. Res.* **101**, 29,387.
- Luna, H., Michael, M., Shah, M. B., Johnson, R. E., Latimer, C. J., and McConkey, J. W.: 2003, *J. Geophys. Res.* **108**, 10.1029/2002JE001950.
- Maurice, S., and Engle, I. M.: 1995, *J. Geophys. Res.* **100**, 17143.
- Maurice, S., Engle, I. M., Blanc, M., and Skubis, M.: 1996a, *J. Geophys. Res.* **101**, 27053.
- Maurice, S., Sittler, E. C., Cooper, J. F., Mauk, B. H., Blanc, M., and Selesnick, R. S.: 1996b, *J. Geophys. Res.*, **101**, 15211–15232.
- McComas, David J., and Jane E. Nordholt: 1990, *Rev. Sci. Inst.* **61**, 3095–3097.
- McComas, D. J., Nordholt, J. E., Samuel, J., Bruce, B., Barraclough, L., and Gosling, J. T.: 1990, *Proc. Natl. Acad. Sci., U S A*, **87**, 5925–5929.
- McComas, D. J., Nordholt, J. E., Young, D. T., and Berthelier, J. J.: 1998, in R. F. Pfaff, J. E. Borovsky, and D. T. Young (eds.), *Measurement Techniques in Space Plasmas: Particles*, AGU Geophysics Monograph Series, Vol. 102, pp. 187–193.
- McComas, D. J., Schwardron, N. A., Crary, F. J., Elliott, H. A., Young, D. T., Gosling, J. T., Thomsen, M. F., Sittler, E., Berthelier, J. J., Szego, K., and Coates, A. J.: 2004, *J. Geophys. Res. (Space Phys.)*, **109**, A02104.
- Mizera, P. F., et al.: 1981, *J. Geophys. Res.* **86**, 2329.
- Mizera, P. F., Fennel, J. F., Croley, D. R., et al.: 1981, *J. Geophys. Res.* **86**, 2329.
- Morfill, G., Havnes, O., and Goertz, C. K.: 1993, *J. Geophys. Res.* **98**, 11285.
- Nagy, A. F., and Cravens, T. E.: 1998, A Review, *Planet Space Sci.* **46**, 1149.
- Nagy, A. F., Liu, Y., Hansen, K. C., Kabin, K., et al.: 2001, *J. Geophys. Res.* **106**, 6151.
- Ness, N. F., Acuna, M. H., and Behannon, K. W.: 1982a, *J. Geophys. Res.* **87**, 1369.
- Ness, N. F., Acuña, M. H., Behannon, K. W., and Neubauer, G. M.: 1982b, *J. Geophys. Res.*, **87**, 1369.
- Noll, K. S., Roush, T. L., Cruikshank, D. P., Johnson, R. E., and Pendleton, Y. L.: 1997, *Nature* **388**, 45–47.
- Nordholt, J. E., Berthelier, J.-J., Burr, D. M., Funsten, H. O., Goldstein, R., Illiano, J. M., McCabe, K. P., McComas, D. J., Potter, D. M., and Young, D. T.: 1998, in R. Pfaff, J. Borovsky, and D. Young (eds.), *Measurement Techniques in Space Plasmas: Particles*, AGU Geophysics Monograph Series Vol. 102, pp. 209–214.
- Pontius, D. H., and Hill, T. W.: 1982, *Geophys. Res. Lett.* **12**, 1321.
- Reiff, P. H., H. L. Colin, J. D. Craven, et al.: 1988, *J. Geophys. Res.* **93**, 7441.
- Richardson, J. D.: 1986, *J. Geophys. Res.* **91**, 1381.
- Richardson, J. D.: 1992, *J. Geophys. Res.* **97**, 13705.
- Richardson, J. D.: 1995, *Geophys. Res. Lett.* **22**, 1177.

- Richardson, J. D.: 1998, *Rev. Geophys.* **36**, 501.
- Richardson, J. D., and Eviatar, A.: 1987, *Geophys. Res. Lett.* **14**, 999.
- Richardson, J. D., Eviatar, A., McGrath M. A., and Vasyliunas, V. M.: 1998, *J. Geophys. Res.*, **103**, 20245.
- Richardson, J. D., Eviatar, A., and Siscoe, G. L.: 1986, *J. Geophys. Res.* **91**, 8749.
- Richardson, J. D., and Sittler, E. C.: 1990, *J. Geophys. Res.*, **95**, 12019.
- Ritzau, S. M., and Baragiola, R. A.: 1998, *Phys. Rev. B* **58**, 2529.
- Rymer, A. M., Coates, A. J., Abel, G. A., Linder, D. R., Svenes, K., Narheim, B., Thomsen, M., and Young, D. T.: 2001, *J. Geophys. Res.* **16**, 30177.
- Shemansky, D. E., and Hall, D. T.: 1992, *J. Geophys. Res.* **97**, 4143.
- Shemansky, D. E., Matheson, P., Hall, D. T., Hu, H.-Y., and Tripp, T. M.: 1993, *Nature* **363**, 329.
- Shemansky, D. E., Smith, G. R., and Hall, D. T.: 1985, *EOS Trans. AGU* **66**, 1108.
- Shi, M., Baragiola, R. A., Grosjean, D. E., Johnson, R. E., Jurac, S., and Schou, J.: 1995a, *J. Geophys. Res.* **100**, 26387.
- Shi, M., Grosjean, D. E., Schou J., and Baragiola, R. A.: 1995b, *Nucl. Instrum. Methods* **B96**, 524.
- Scarf, F. L., Frank, L. A., Gurnett, D. A., Lanzerotti, L. J., Lazarus, A., and Sittler Jr., E. C.: 1984, in T. Gehrels, and M. S. Matthews (eds.), *Saturn*, University of Arizona Press, Arizona, pp. 318–353.
- Shematovich, V. I., Johnson, R. E., Micheal, M., and Luhmann, J. G.: 2003, *J. Geophys. Res.*, **108**(E8), 5087.
- Sittler, E. C., Jr.: 1993, *Rev. Sci. Instrum.* **64**, 2771, 1993.
- Sittler, E. C., Jr., and Hartle, R. E.: 1996, *J. Geophys. Res.* **101**, 10863.
- Sittler, E. C., Jr., Scudder, J. D., and Bridge, H. S.: 1981, *Nature* **292**, 711.
- Slavin, J. A., Smith, E. J., Gazis, P. R., and Mihalov, J. D.: 1983, *Geophys. Res. Lett.* **10**, 9.
- Stevenson, D. J.: 1982, *Nature* **298**, 142–144
- Szego, K., Young, D. T., Barraclough, B., Berthelier, J.-J., Coates, A. J., *et al.*: 2003, *J. Geophys. Res.* **108**, 11–1.
- Thomsen, M. F.: 1985, in B. T., Tsurutani and E. Stone (eds.), *Collisionless Shocks in the Heliosphere: Reviews of Current Research*, AGU Geophysics Monograph Series, Vol. 35, 253.
- Vasyliunas, V. M.: 1983, in A. J. Dessler (ed.), *Physics of the Jovian Magnetosphere*, Cambridge University Press, Cambridge, Chap. 11.
- Vilppola, J. H., Keisala, J. T., Tanskanen P. J., and Huomo, H.: 1993, *Rev. Sci. Instrum.* **64**, 2190.
- Vilppola, J. H., Tanskanen, P. J., Barraclough, B. L., and McComas, D. J.: 2001, *Rev. Sci. Instrum.* **72**, 3662.
- Vilppola, J. H., Tanskanen, P. J., Huomo, H., and Barraclough, B. L.: 1996, *Rev. Sci. Instrum.* **67**, 1494.
- Waite, J. H., *et al.*: 2004, *Space Sci. Rev.*, **114**, 113–231.
- Warwick, J. W., Pearce, J. B., Evan, D. R., *et al.*: 1981, *Science* **212**, 239.
- Wollnik, H.: 1971, *Nucl. Instrum. Method* **95**, 453.
- Woodliffe R. D.: 1991, Design of Space-Borne Plasma Analysers by Computer Simulation, *Ph.D. Thesis*, University of London.
- Woodliffe R. D., and A. D. Johnstone: 1998, in R. Pfaff, J. Borovsky, D. Young (eds.), *Measurement Techniques in Space Plasmas: Particles*, AGU Monograph Series **102**, 263–268.
- Young, D. T., Bame, S. J., Thomsen, M. F., Martin, R. M., Burch, J. L., Marshall, J. A., and Reinhard, B.: 1988, *Rev. Sci. Instrum.* **59**, 743.
- Young, D. T., Barraclough, B. L., Berthelier, J. J., Blanc, M., Burch, J. L., Coates, A. J., Goldstein, R., Grande, M., Hill, T. W., Illiano, J. M., Johnson, M. A., Johnson, R. E., Baragiola, R. A., Kelha, V., Linder, D., McComas, D. J., Narheim, B. T., Nordholt, J. E., Preece, A.,

- Sittler, E. C., Svenes, K. R., Szalai, S., Szegö, K., and Tanskanen, P.: 1998, in R. F. Pfaff, J. E. Borovsky, and D. T. Young (eds.), *Measurement Techniques in Space Plasmas: Particles*, AGU Geophysics Monograph Series **102**, 237–242.
- Young, D. T., Barraclough, B. L., McComas, D. J., Thomsen, M. F., McAbe, K., and Vigil, R.: 1991, *J. Spacecraft Rockets* **29**, 596–598.